UNIVERSITY
OF TRENTO - Italy
DEPARTMENT OF INDUSTRIAL ENGINEERING

XXX cycle

Doctoral School in Materials, Mechatronics and Systems Engineering

Theoretical analysis and experimental investigation of contact fatigue and surface damage in prealloyed and diffusion bonded sintered steels

Samuel Tesfaye Mekonone

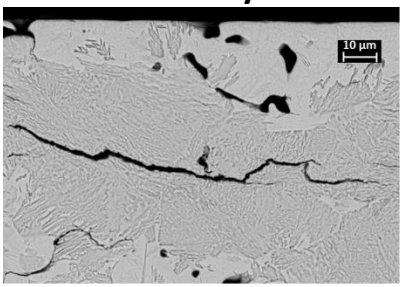

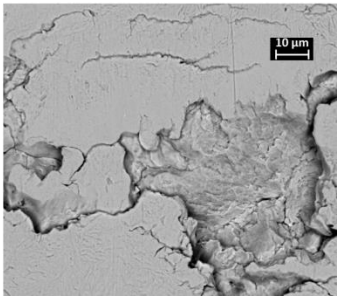

June 2018

THEORETICAL ANALYSIS AND EXPERIMENTAL INVESTIGATION OF CONTACT FATIGUE AND SURFACE DAMAGE IN PREALLOYED AND DIFFUSION BONDED SINTERED STEELS

Samuel Tesfaye Mekonone

E-mail: samitop10@gmail.com

Approved by:

Prof. Molinari Alberto, Advisor
Department of Industrial Engineering
University of Trento*, Italy.*

Prof. Ilaria Cristofolini, Advisor
Department of Industrial Engineering
University of Trento*, Italy.*

External reviewer:

Prof. Herbert Danninger
Institute of Chemical Technology and Analytics
Vienna University of Technology*, Austria.*

Prof. Christoph Broeckmann,
Department of Material Science and Engineering
University of RWTH*, Germany.*

Commission:

Prof. Vigilio Fontanari
Department of Industrial Engineering
University of Trento*, Italy.*

Prof. Lorella Ceschini
Department of Materials Engineering
University of Bologna*, Italy.*

Prof. Franco Bonollo
Department of Management and Engineering
University of Padova*, Italy.*

University of Trento,
Department of Industrial Engineering
June 2018

University of Trento – Department of Industrial Engineering

Doctoral Thesis

Samuel Tesfaye Mekonone – 2018
Published in Trento (Italy) – by University of Trento

ISBN: - - - - - - - - -

In loving memory of my grandmother,
Emahoy Yengussa Molla

Abstract

The contact fatigue and surface damage of prealloyed (Fe-0.85Mo, Fe-1.5Mo) and diffusion bonded (Ni-free, low-Ni, high-Ni) powder metallurgy (PM) steels were investigated. Materials subjected to contact stress fail due to the nucleation of subsurface cracks (contact fatigue cracks), nucleation of brittle surface cracks, and surface plastic deformation. The occurrence of these contact damage mechanisms was predicted using theoretical models, which were developed by assuming that crack nucleation is preceded either by local plastic deformation (contact fatigue and surface plastic deformation) or local brittleness (brittle surface cracks) of the metallic matrix. With reference to the mean yield strength of the matrix (mean approach) or the yield strength of soft constituents (local approach), the models predict the theoretical resistance of materials to the formation of damage mechanisms. The models were then verified using experimental evidence from lubricated rolling-sliding contact tests.

In addition, the effect of compact density and microstructures of materials on the resistance to contact damage mechanisms was investigated. Density and microstructure were modified by varying green density, alloying elements, sintering temperature and time, and applying strengthening treatments: carburizing and shot peening on prealloyed (homogenous microstructure) and carburizing, sinterhardening and through hardening on diffusion bonded (heterogeneous microstructure) steels.

The theoretical resistance to subsurface and surface crack nucleation in prealloyed materials was predicted using the mean approach since the microstructure is homogeneous. But the local approach is applied for diffusion bonded materials (Ni-free and low-Ni); exceptionally, the mean approach was applied for some homogeneous microstructure of Ni-free material sintered at a prolonged time. However, the models have a limitation in predicting the contact damage mechanisms in a high-Ni material. This issue may require further investigation to modify the model.

Shot peening provides higher resistance to the nucleation of surface cracks. High compact density, high sintering temperature and time, and sinterhardening improve the resistance to contact damage mechanisms for Ni-free and low-Ni materials.

Table of Contents

Chapter I

1. Introduction

Powder metallurgy (PM) is a net shape and cost-effective technology that is used to produce mechanical components characterized by excellent dimensional and geometrical precision with good mechanical properties. This technology is highly competitive compared with other conventional processing methods such as casting, machining or forging.

In conventional processes, first, the metallic powder is compacted in a die to form a so-called green compact, then consolidated through heat treatment (that results in intermetallic bonding) called sintering. Gears, bearings and cams are among the most common PM components that are produced through the compaction and sintering processes.

However, residual porosity is an inherent characteristic of these components. Since porosity is a void in the microstructure, it determines the stress field significantly, intensifying stress locally and reducing the load bearing section. Porosity reduces mechanical properties of PM components, and provides lower resistance in comparison to those of cast and wrought steel, in particular, ductility, toughness and fatigue resistance.

The methods to improve the mechanical properties of PM materials are increasing green density (compaction), improving pore morphology and sintering shrinkage (sintering), strengthening the microstructure (sinterhardening, thorough hardening and thermochemical treatments), increasing surface density (surface rolling), and introducing residual stresses (shot peening). Increasing green density and strengthening the microstructure are counteracting requirements since the former are attained by using elemental powders, the latter by introducing alloying elements. The use of diffusion bonded powders is the compromise between the two requirements, but it results in heterogeneous microstructures, which are another peculiar

characteristic of press and sintered steels. Microstructural heterogeneity causes a non-homogeneous distribution of strength in the cross-section. Microstructural heterogeneity of diffusion bonded steels may be reduced by increasing sintering temperature and time.

For components that undergo a cyclic contact with a counteracting surface, contact fatigue and related surface damage are the mechanisms by which the surface may be failed. For instance, surface durability is a very demanding requirement for components used in automobile engines, such as gears and cams, where the surface is used to transmit dynamic contact load and rotating motion. Therefore, the effect of porosity and microstructural heterogeneity on these surface and subsurface damage mechanisms is needed to be investigated to propose the best strategies (material, density, and strengthening process) that could enhance the performance.

Several years ago, GKN Sinter Metals SPA (a world-leading PM component producer) and the University of Trento (Department of Industrial Engineering) started cooperation to investigate the effect of porosity and microstructural heterogeneity on the contact fatigue of diffusion bonded materials. The research mainly focused on determining the resistance of contact fatigue. Recently, the collaboration extended to include prealloyed steels (characterized by homogenous microstructure), other diffusion bonded steels and to apply different strengthening treatments.

In this Ph.D. work, the contact fatigue and surface damage behavior of PM steels, with homogenous and heterogonous microstructures, were investigated in terms of resistance to the nucleation of subsurface cracks (contact fatigue), surface cracks (brittle fracture) and surface plastic deformation. These phenomena are the possible damage mechanisms that the material may experience when it is subjected to contact stress.

Theoretical models were first developed to predict the nucleation of subsurface and surface cracks, as well as surface plastic deformation; these models are formulated starting from the theoretical analysis of the local plastic deformation and the brittle fracture caused by pores. The models were applied with both the mean approach

and the local approach, considering the mean mechanical properties of the matrix and the mechanical properties of the weaker constituent, respectively.

The theoretical models were then validated using lubricated rolling sliding tests carried out on different materials. Based on their resistance to different damage mechanisms, the materials investigated were ranked, and the effect of composition, alloying strategy, sintering temperature and time (in diffusion bonded steels), strengthening treatment and shot peening was determined.

The thesis was divided into five chapters. The first chapter is the introduction. Chapter II describes the scientific background, reviewing fundamental contact mechanics theories and concepts about the contact fatigue and surface damage behavior of PM materials, and describing the theoretical models. The investigated materials and experimental methods are described in Chapter III. In Chapter IV, the results are presented, discussed and summarized. Finally, the main highlights of the project and some suggestions for future work are described in the concluding chapter.

Chapter II

2. Scientific Background

2.1. Literature review on contact fatigue and surface damage of PM steels

Nowadays a large spectrum of structural parts is manufactured by Powder Metallurgy (PM) aiming to exploit its potential to produce the complex geometries and net shape components, with an efficient material utilization capabilities [1]. Cams, gears, and bearings are among the most popular machine elements produced using this technology. These parts are often assembled in the systems and automobile engines, which are used to transmit the dynamic contact load and torque. During the service time, the surface undergoes a cyclic contact with counteracting surface and is subject to high cyclic contact stress that leads the surface to eventual failure.

The study of contact damage of PM steel uses a pioneering benchmark work of Tallian [2], who first reported on wrought steels in which damage mechanisms are categorized as surface and subsurface originated cracks. The former are classified as wear damage (dominant in sliding contact) and the latter as contact fatigue (dominant in pure rolling or rolling-sliding contact) [3–8] damage.

Subsurface and surface damage are associated with a higher stress field at the contact zone that results in the formation of microcracks [2,9] and the propagation and branching could generate surface wear particles. According to the nucleation site and the size of the detached wear particles, different nomenclature of contact fatigue and wear damage has been used by many authors. The most common terms are reported in [10];

- Micro and macro pitting: represent all surface originated contact fatigue and wear damage

- Spalling: represents subsurface contact fatigue damage
- Case crashing: represents all large-scale subsurface contact fatigue often found in the case hardened materials.

The contact fatigue is different from the normal fatigue (push-pull, bending and torsion) because the stress is a Hertzian stress state; pressure distribution is mostly concentrated locally at a small contact area, and contact fatigue has no endurance limit [11]. But the nomenclature and the approach used to investigate the contact fatigue damage are similar to those used or the normal fatigue. The methodology, characterization technique, and design approach for contact fatigue of PM materials are highlighted in [12–17].

Contact fatigue of PM steel is a complex phenomenon and still an active research area. That is because of the presence of many influencing parameters such as material and process parameter, contact mechanics, contact friction and surface conditions, subsurface defects microstructure, etc., all these paramteres make the study very complex and multidisciplinary.

Figure 2.1.1 illustrates the diagram showing the parameters that could be considered during the investigation of contact fatigue of PM steels.

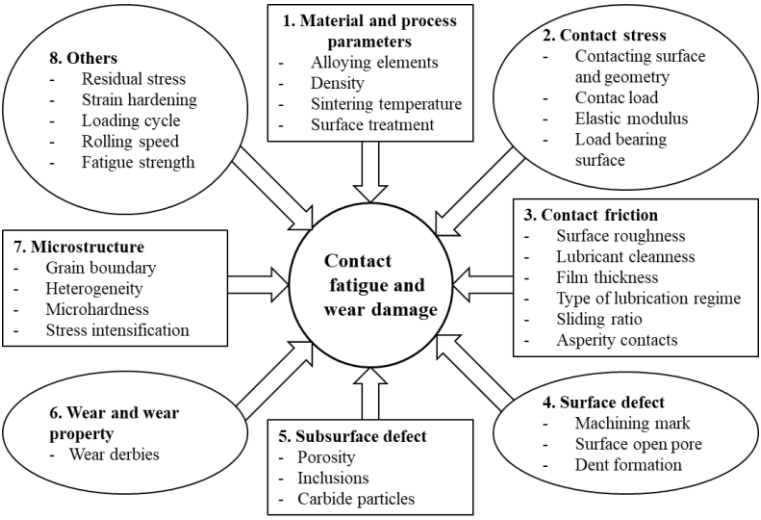

Figure 2.1.1 Parameters that affecting contact fatigue and wear damage

Porosity in the microstructure is the most determining factor and most studied parameter in the history of PM materials. It is the void between interconnected particles that introduces a negative impact on the surface damage resistance of the materials. This effect was highlighted in the work of Haynes [18] and others [16,19,20], which conclude that the fatigue endurance limit and fatigue life is affected negatively by the presence of pores.

Even though the contact fatigue is different from the normal fatigue damage mechanisms, there is no doubt that porosity also plays a determining factor in contact fatigue life. The contact fatigue property of PM materials were reported in several papers [21–24], which demonstrate that the fatigue strength is always lower than that of the pore-free material. The main reasons behind the impact of porosity on PM material are:

1. pores intensify stress locally [25],
2. pores are often crack nucleation sites [26],
3. pore connectivity and network are propagation pathways [27] and

4. the presence of pores reduces the cross-section area that is involved in supporting the load [28] (fraction of the load bearing section).

Locally, stress is intensified and becomes higher at the pore edge, and the first crack nucleates in the microstructure surrounding the pore, then the crack growth follows the weakest direction along the pore connectivity and networks.

Some of the contact fatigue crack formation and life-limiting parameters are discussed briefly in the next paragraphs.

2.2. Materials and process parameters

Fatigue strength and other mechanical properties of sintered structural components are influenced by alloying elements, sintering conditions, density and additional surface treatments[13,29].

2.2.1. Alloying elements and powder mixing

Alloying elements **can** modify the microstructure, the yield and fatigue strength of steel structural components, through their effect on hardenability. The influence on the microstructure relates to the hardenability factor. Figure 2.2.1 represents the amount of alloying element versus the hardenability factor: as provided by Höganäs AB handbook.

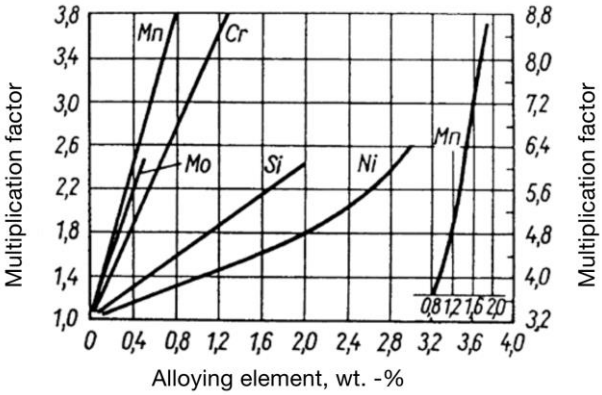

Figure 2.2.1 the effect of alloying element on hardenability factor

Manganese (Mn), molybdenum (Mo) and chromium (Cr) provide a higher hardenability factor, which was also demonstrated in [30]. These elements are the most common alloying elements that are applied in PM steels. In addition to the hardenability factor, some alloying elements promote solution hardenings, such as nickel (Ni) and copper (Cu).

Moreover, the type of powder alloying method can affect the microstructure. Microstructure, microstructural homogeneity, and density depend on the alloying strategy used to preserve compressibility when needed. The two most common powder alloying in the conventional PM processes are prealloyed Fe-Mo base powder and partially prealloyed (admixed Ni and Cu powders with prealloyed Fe-Mo). Prealloyed Fe-Mo powder with the addition of graphite blend provides uniform microstructure and properties with a certain limitation of compressibility. But partially prealloyed powder improves powder compressibility and provides heterogeneous microstructure [31]. Prealloyed admixed with only nickel powder (without copper) avoids the formation of the secondary pore and increases the compact density. That helps to reduce the pore connectivity and the pore network.

Ni stabilizes austenite, and it causes the formation of heterogeneous microstructure; this would affect the contact fatigue behavior. However, with the different amount of

austenite, the influence on the dynamic loading was investigated, and the specimen with higher retained austenite shows higher fatigue life [32]. The increasing of fatigue life may be due to the decomposition and transformation of austenite into martensite above the critical load that improves the resistance to fatigue cracks. But in the general case, the presence of austenite or Ni rich austenite reduces local yield strength.

In the case of contact fatigue crack nucleation, the effect of austenite has not yet been systematically studied. The little interest in this area by most researchers is due to the complexity of the phenomena of contact stress distribution, and the interaction between softer and harder constituent in the heterogeneous microstructure. A few investigations on diffusion bonded steel with 4 % Ni have shown that contact fatigue cracks are nucleated at a low applied load at the pore edges when the pores are surrounded by the softer Ni-rich microstructures [33].

2.2.2. Compaction and sintering parameters

The correlation of the mechanical behavior of PM compacts with density is a common approach. Achieving high density of structural component is the goal that allows low porosity and pore size in the microstructure. Densification may be attained by applying either higher compaction pressure or high sintering temperature [27] techniques. These techniques eliminate certain pore populations and subsequently reduce the fractional porosity. They also reduce local stress field and strain accumulation during mechanical loading of a component. The associated effects reported are that the yield strength and fatigue endurance limit increase with the density [18,20,29,34,35].

Sintering temperature and sintering condition are important parameters affecting pore morphology, density, microstructural homogeneity, and interparticle bonding. The conventional sintering temperatures are between 1120 °C to 1150 °C, applied to most conventional PM materials. Alloying elements characterized by their higher oxygen sensitivity such as chromium and manganese need higher sintering

temperatures up to 1250 °C or above. High sintering temperature improves interparticle bonding through the reduction of oxide layers. The final microstructure is then characterized by well-homogenized and regular pore morphology.

Sinterhardening, in which martensitic transformation occurs just after the completion of isothermal holding time in the furnace, is effective regarding the formation of harder microstructure and is cost-effective. More than 80 % of the martensitic microstructure can form during this process [36]. This microstructure could improve contact fatigue and wear damage resistance. Based on the powder blending, the application of sinterhardening provides a different result on the contact fatigue resistance of the materials.

2.2.3. Surface treatment and surface characteristics

Among the different surface treatments, carburizing and shot peening are relatively economical industrial processes which improve the contact fatigue and surface wear damage. These two techniques modify the microstructure and behavior of the surface layers.

Carburizing is an old and well known industrial process that modifys PM steel surface. The case is enriched with carbon through a thermochemical diffusion from the higher potential of the furnace atmosphere that is maintained in the austenite field to the lower carbon potential of steel. Subsequent quenching forms the tetragonal martensitic microstructure, which is characterized by high microhardness. Therefore, depending on the characteristic case depth ($d_{550\ HV0.1}$), obtained through optimal use of carbon potential, carburizing temperature and time, the resistance to contact fatigue and wear damage can be greatly improved.

However, the presence of pores in the hardened matrix and its effect on the damage and damage mechanism are not investigated in detail. In particular, the hardened surface layers are prone to the formation of a brittle cracks, because the pore become equivalent to a crack of a critical length[26].

Shot peening is a process in which the stream of spherical shots impinging the surface at high velocity and controlled conditions allows to achieve localized cold working on the surface layers of mechanical parts [37–39]. The process introduces surface plastic deformation and results in accumulation of compressive residual stresses, strain hardening, and phase transformation. Depending on the compressive residual stress profile and the peak stress, fatigue life of shot peened parts improves due to the positive effect on extending crack nucleation period and crack growth arresting [40].

Depends on the shot target microhardness and the amount of target retained austenite, plastic deformation response is observed in the surface region [39,41,42]. In the case of harder shot and softer target, maximum compressive stress is accumulated at the surface and reaches 60% of yield strength[41]. In this combination, shot peening can improve surface resistance to contact fatigue and wear damage with the proper use of the shot target property.

An additional effect of shot peening in porous materials is the densification of the surface layers due to plastic deformation [38,43]. Investigation of shot peening on sinterhardened parts show that surface pores are collapsed and closed using ceramic shot and improved the contact fatigue resistance by 30% [44].

However, no literatures are available for the effect of shot peening on the contact fatigue performance of case carburized parts, that is limited only to wrought steel[40,45]. In this particular cases, densifying the surface is expected to have a significant effect on the brittle crack resistance. What is more, shot peening introduces surface roughness and elongated residual pore near the densified surface. The positive effect of the technology on the contact damage is still under investigation.

2.3. Contact mechanics

Table 2.3.1 reports the list of parameters and their units utilized in the following

Table 2.3.1. List of symbols and definitions

Notation	Definition	Notation	Definition
E	elastic modulus (N/mm^2)	P_{max}	maximum Hertzian pressure (N/mm^2)
ν	Poisson's ratio	P_o	mean Hertzian pressure (N/mm^2)
b	half contact width (mm)	P	contact pressure (N/mm^2)
L	contact length (mm)	$\sigma_x, \sigma_y, \sigma_z$	principal stresses (N/mm^2)
R	contact radius (mm)	τ_{xz}, τ_{yz}	principal shear stresses (N/mm^2)
F	applied force (N)	$\sigma_{eq.}$	equivalent stress (N/mm^2)
E_c	effective contact modulus (N/mm^2)	τ_{max}	maximum shear stresses (N/mm^2)
R_c	effective contact radius (mm)	μ	coefficient of friction
		$\sigma_{x,t}$	Surface tangential stress

Figure 2.2.1 represents the configuration of elastic contact between two cylindrical surfaces and the pressure distribution within the contact width.

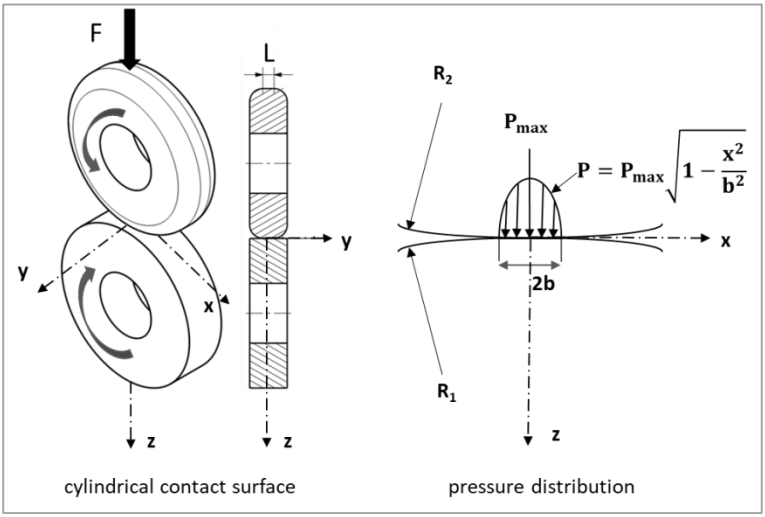

Figure 2.3.1 Contact between cylindrical surfaces and parabolic pressure distribution **[46,47]**

Through the action of a force, F, cylindrical surfaces with the radius R_1 and R_2, brought into physical contact and initially forms a line contact. The parabolic pressure distribution is build-up at the contact zone over the contact length, and the pressure is the maximum at the center of the contact width [48]. This configuration of contact represents the real machine element contacts, such as cam and gear teeth interaction with the counterface. Often the contact area is small, and higher contact stress is applied to the contact zone, that results in elastic or elastic-plastic deformation in the surface layers.

According to the Hertzian contact theory (that assumes the contact is elastic, smooth and non-conformal contact surfaces), two-dimensional compressive stress distribution on the x-z plane is determined using the formulas from eq.(1) to eq. (5) [49].

$$\sigma_x = \frac{P_{max}}{b}\left\{m\left(1+\frac{z^2+n^2}{m^2+n^2}\right)-2z\right\} \quad (1)$$

$$\sigma_z = \frac{P_{max}}{b} m \left(1 - \frac{z^2+n^2}{m^2+n^2}\right) \quad (2)$$

$$\sigma_y = \nu(\sigma_x + \sigma_z) \quad (3)$$

$$\tau_{max} = \begin{cases} \tau_{xz} = \frac{\sigma_z - \sigma_x}{2}, & \frac{z}{b} < 0.463 \\ \tau_{yz} = \frac{\sigma_z - \sigma_y}{2}, & \frac{z}{b} > 0.463 \end{cases} \quad (4)$$

$$\sigma_{eq.} = \frac{1}{2}\left[(\sigma_z - \sigma_x)^2 + (\sigma_y - \sigma_x)^2 + (\sigma_z - \sigma_y)^2\right]^{0.5} \quad (5)$$

Where, m and n are variables described in terms of space x, z coordinates and determined using eq. (6) and eq. (7), respectively.

$$m^2 = \frac{1}{2}\left[\{(b^2 - x^2 + z^2)^2 + 4x^2z^2\}^{\frac{1}{2}} + (b^2 - x^2 + z^2) \right] \quad (6)$$

$$n^2 = \frac{1}{2}\left[\{(b^2 - x^2 + z^2)^2 + 4x^2z^2\}^{\frac{1}{2}} - (b^2 - x^2 + z^2) \right] \quad (7)$$

The sign of m and n are associated with the sign of z and x axis, respectively.

The maximum or mean Hertzian pressure applied on the cylindrical contact surface is determined using the relation given by eq. (8) and eq. (9).

$$P_O = 0.78 P_{max} \quad (8)$$

$$P_{max} = \frac{2F}{\pi b L} \quad (9)$$

Half contact width b relates to the effective elastic modulus, the effective radius of curvature, and the applied load and is determined using eq. (10)[48].

$$b = \sqrt{\frac{4R_c F}{\pi L E_c}} \quad (10)$$

Effective modulus and effective radius of curvature are evaluated using eq. (11) and eq. (12)

$$\frac{1}{E_c} = \frac{1-\nu_1^2}{E_1} + \frac{1-\nu_2^2}{E_2} \tag{11}$$

$$\frac{1}{R_c} = \frac{1}{R_1} + \frac{1}{R_2} \tag{12}$$

Figure 2.3.2 represents normalized Hertzian contact stress contours on x-z plane and profile along the z-axis. Variable contact width and stress field are normalized by half contact width and maximum Hertzian pressure, respectively.

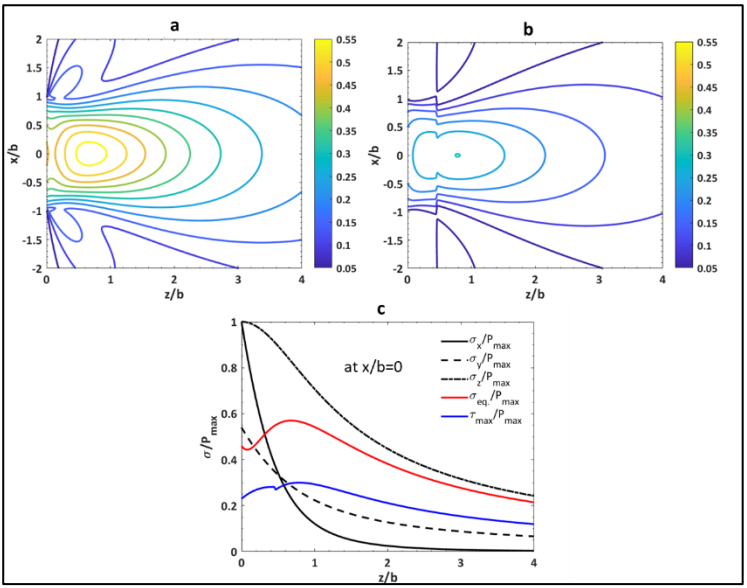

Figure 2.3.2 Normalized contour of equivalent stress (a) and maximum shear stress (b); and profiles of all contact stresses (c) [25]

The principal stresses distribution are always compressive, and the three different stresses along the orthogonal axes introduce a triaxial state of stress [50,51]. This triaxiality introduces elastic or plastic zone evolution of the contact region. Hertzian

principal stress and subsurface plastic zone evolution during the contact fatigue are investigated in [52,53] that shows large scale damage related to subsurface maximum Hertzian stress.

Maximum stress found in the subsurface layer between 100 µm - 400 µm depth [47]. The Hertzian depth varies in this range, depending on the intensity of the pressure distribution. The influence of applied force on half contact width, mean pressure, and Hertzian equivalent stress of two different contacting materials (distinguished using subscript 1 and 2) is shown in Figure 2.3.3.

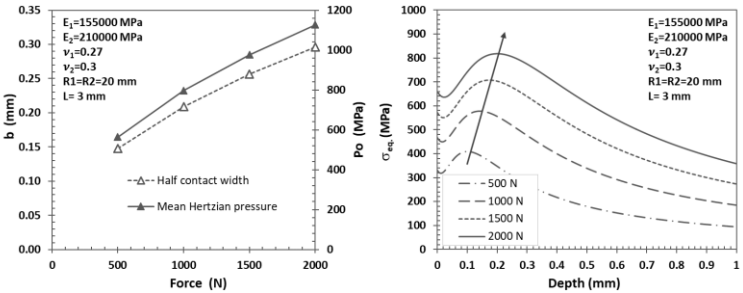

Figure 2.3.3 Influence of applied force on half contact width, mean pressure, and maximum Hertzian equivalent stress

Half contact width, mean pressure and maximum equivalent stress at the Hertzian depth increase with the applied force.

However in real contact surface, the topographic characteristics and material property are not uniform, and the pressure distribution and Hertzian depth change within the contact zone. Contact stress distribution at irregular, discrete and asperity contacts reviewed in [54–56]. All discrete asperity contact reduces the contact area and the region around the asperity subjected to elastic or plastic deformation. On the other hand, this type of contact results in a high frictional force at the surface.

2.4. Contact friction and surface tensile stress

The surface stress is determined by the presence of surface irregularity, surface area, and asperity contacts. When the surface is irregular due to the presence of groove, valley or open porosity, the number of asperity contact increases. The contact always associated with the generation of surface tangential stress due to friction, which is very high near to the asperity contacts [57]. The surface tangential stress profile on the x-y contact plane is determined using eq. (13)[49]

$$\sigma_{x,t} = -2\mu P_{max} \begin{cases} \left[\frac{x}{b} + \sqrt{1 - \frac{x^2}{b^2}}\right] & x \le -b \\ \frac{x}{b} & -b < x < b \\ \left[\frac{x}{b} - \sqrt{\frac{x^2}{b^2} - 1}\right] & x \ge b \end{cases} \quad (13)$$

Figure 2.4.1 represents the normalized axis-symmetric tangential stress profile along the normalized x-axis with a variable coefficient of friction. The surface tangential stress reaches the peak when x=b, and increases sharply with the coefficient of friction.

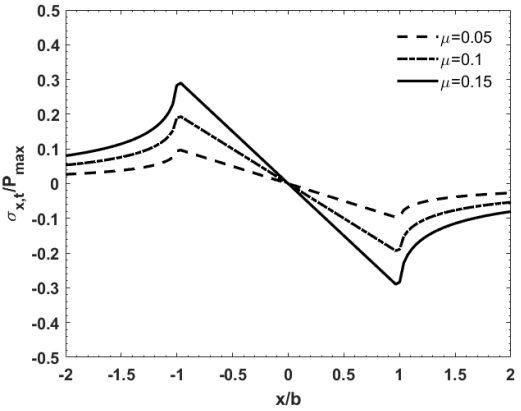

Figure 2.4.1 Normalized surface tangential stress profile at a variable friction coefficient

The peak tangential stress at the surface affects the resistance to contact fatigue and wear damage. Materials with a surface defect or surface pore that attribute stress intensification: leads early damage even at lower stress.

On the other hand, surface stress induces material to flow towards the surrounding pores results in surface densification that introduces both positive and negative impacts on the surface damage resistance [15]. The positive effect is the matrix can be strain hardened, load bearing surface can increase, and the unclosed pore act as a suitable medium to trap derbies. These effects improve the resistance to dynamic loading of the surface layer. On the contrary, densification can develop unstable hydraulic pressure that alters damage mechanisms and could reduce the resistance to surface damage. Moreover, when the lubricant is forced into an isolated surface pore or crack front, strong hydrostatic pressure could build up during the contact. Therefore, the mechanical action of hydrostatic pressure can strongly influence the resistance to the surface crack formation. In particular, the shear mode of surface damage can divert to the opening mode of damage by additional lubricant pressure [58].

2.5. Surface damage and damage mechanism

Referring to the position where the cracks are nucleated and to the characteristics of the final surface damage, cracks are classified into two types [2,59,60]:

a) Subsurface initiated cracks (contact fatigue cracks) and
b) Surface initiated cracks

Figure 2.5.1 shows an example of subsurface and surface initiated cracks observed during rolling-sliding contact fatigue test of porous material.

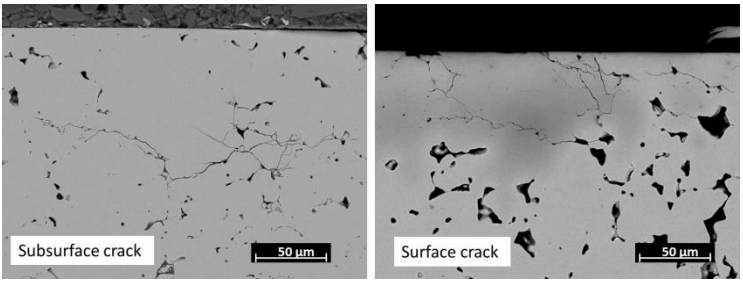

Figure 2.5.1 Types of surface damage and damage mechanisms

In both cases, cracks are nucleated at the pore edge and followed by crack propagation and branching along the pore networks. The former grows towards the surface, and the latter grows towards the depth. The dominant mode of failure depends on the surface condition, lubrication, and material properties. For instance, grinding and high quality of surface finish, with precise dimensional and geometrical characteristics of the component, and under a good lubrication condition, cracks are nucleated usually in the subsurface layers. But in the case of rough surface and poor lubrication condition, cracks are nuclueated usually at the surface[50].

In particular, the sequence of events in subsurface originated damage are crack nucleation in the subsurface followed by propagation and crack branching towards the surface [61,62], then finally leads to particle detachment either by spalling or case crashing. This damage is often characterized by a large scale contact fatigue damage [26,61]. The characteristic depth or Hertzian depth at which cracks are nucleated is affected by parameters like surface roughness and hardening depth [50]. Crack formation relates to the maximum shear or equivalent stress at the characteristics depth. In addition to the material properties, microstructural defects such as inclusion, pore and oxide particle are often responsible for this type of damage[6,63–65].

In the case of surface originated damage, the sequence of events are surface crack nucleation followed by shallow shear mode crack growth towards the bulk and crack deflection to the surface [61,62]. Surface damage is a detachment of particles (micro and macro pitting) characterized by a shallow depth up to 10 µm [62]. Surface

friction, surface shear stress, asperity contacts, and lubricant pressure are responsible for the formation of surface cracks and the subsequent surface damage.

In addition to the surface tribological condition and porosity, surface microstructure determines the response of the surface. The response may be either elastic, plastic deformation or brittle fracture [39]. In the case of a softer/weaker matrix, the material response is either elastic or plastic deformation. The plastic deformation zone is where cracks are nucleated, and the severity of the deformation determines their growth. However, in the case of a hard matrix, the formation of a brittle crack may occur. In particular, the presence of surface pore in the low toughness matrix (martensitic microstructure) increases the chance to the brittle crack formation. The surface pore acts as a defect, and the size of the pore in the matrix determines the surface originated brittle damage.

Regardless of the type of crack formation, contact fatigue and wear damage mechanisms of PM materials follows the following steps [66,67]:

- Stress field localization at the edge of the open and closed pore.
- Dislocation pile up and strain accumulation at the sharpest edges of the pores and along the grain boundary during every cycle contacts.
- Local stress field promotes local plastic deformation that may result in densification and crack nucleation.
- Any lubricant entrapment to the face of the cracks promote crack tip opening.
- The growth of cracks in the pore connectivity network or towards the low strength of matrix.
- Formation of crack branching due to the interchangeability of a different mode of contact fatigue failure.
- Formation of debris either in the form of pitting or spalling.
- Final surface damage.

2.6. Theoretical prediction of subsurface crack nucleation

Layers of materials underneath the contact surface are subjected to no proportional triaxial stress distributions, which allows the contact zone always subjected to alternative stress during every contact cycles. Unlike normal push-pull fatigue loading, the maximum stress plane or points change during the cyclic contacts. This phenomena results in higher complexity of predicting the contact fatigue cracks and the wear damage. However, several theoretical models are available to predict contact fatigue cracks. The existing models are [68]:

a. Equivalent stress approaches,
b. Maximum shear stress approaches,
c. Critical plane models, and
d. Empirical model.

Shear stress approach is more conservative and can reasonably apply for any materials but with no indication of crack propagation direction. The same is true for equivalent stress that cannot indicate crack growth direction, too.

In the case of porous materials, the equivalent stress and maximum shear stress intensified locally, and the fraction of the load bearing surface is always smaller than 1 (because material ratio is below 100%) [25,61], such that the maximum stress (σ) requires the correction parameters. The modified local stress may be determined using eq. (14) and eq. (15), corresponding to the equivalent and shear stress failure criteria [69,70,66]

$$\sigma = \frac{\sigma_{eq}\,\beta_k}{\Phi} + \sigma_{Res.} \tag{14}$$

$$\sigma = \frac{2\tau_{max}\,\beta_k}{\Phi} + \sigma_{Res.} \tag{15}$$

Where β_k is notch sensitivity of the matrix and given by eq. (16)[71].

$$\beta_k = (K_t - 1)\eta + 1, \quad (16)$$

where, K_t, is pore shape coefficient, that varies from 1 for the pore-free materials to 3 for porous materials, simply by considering the circular pore. η is the coefficient of matrix sensitivity that depends on the microstructural constituents: 0.3, 0.5 and 0.7 correspond to ferrite, pearlite, and martensite, respectively [71]. Φ is the fraction of load bearing sections, which depends on the amount of porosity and pore shape, and is given by eq. (17)[28].

$$\Phi = (1 - (5.58 - 5.57 f_{circle})\varepsilon)^2 \quad (17)$$

where f_{circle} is pore shape factor and ε is fractional porosity.

$\sigma_{Res.}$ is a compressive residual stress induced during either surface treatment, such as shot peening.

Because of the local maximum stresses, subsurface crack nucleation preceded by local plastic deformation. The model derived according to the comparison between local stresses and the material yield strength. The relation is explained using eq. (18),

$$\sigma > \sigma_y \quad (18)$$

The yield strength of heat treated matrix (σ_y) may be determined from the microhardness using eq. (19) [72]

$$\sigma_y = \frac{HV_{0.1}}{4.2} \quad (19)$$

2.7. Theoretical prediction of surface crack nucleation

Depending on the affecting parameters, such as roughness, lubrication regimes, contact friction, surface hardness, and microstructural inhomogeneity, two types of

surface cracks are most common during rolling-sliding contact fatigue. Those are surface cracks due to surface plastic deformation and brittle cracks due to brittleness.

2.7.1. Surface crack nucleation by plastic deformation

Three different stresses may accumulate at the surface,

1. Tangential stress due to the friction of irregular surface or asperity contacts,
2. The mechanical action of the lubricant pressure, and
3. Surface Hertzian stress during the cyclic contact.

All these stresses may promote surface plastic deformation. Depending on the coefficient of friction, typically when $\mu \geq 0.3$ [46,47] the position of Hertzian depth moves to the surface, and the maximum Hertzian stress provides the biggest portion of the three stresses. In the case of hydrodynamic or mixed mode lubrication, Hertzian stress at the surface is still considerable for the analysis of surface plastic deformation. The assumption considered for the analysis of surface plastic deformation were;

- Surface plastic deformation expected due to surface stresses.
- The lubricant pressure could alter surface fracture mode; the influence is ignored for PM material because lubricant possibly escapes through the pore connectivity.
- In the case of heterogeneous microstructure, no combined response (elastic, plastic and brittle fracture) adapted at the same time.
- Cracks may grow along the grain boundary and through the pore networks.

By incorporating stresses and the assumptions, surface plastic deformation is predicted using the Ashby model proposed in [73,74]. The criterion is comparing the

yield strength of the matrix with surface contact stress. The formula (for PM materials) is corrected using the factors that is correlated with microstructural sensitivity and load bearing surface. Therefore, anticipated local plastic deformation of the surface may predict using eq. (20).

$$\sigma_y = P_0 \frac{\beta_k}{Mr_2} \sqrt{1 + 9\mu^2} + \sigma_{Res.} \quad (20)$$

where, P_0 is mean pressure, the constant β_k and Mr_2 are correction factors corresponding to the notch effect of the surface matrix and to the load bearing surface, μ is coefficient of friction and $\sigma_{Res.}$ is compressive residual stress.

Load bearing surface (Mr_2) is defined as the actual area of material in contact and supporting the unit load. In the case of a rough and porous surface, the material that supports contact load is not continuous because of the presence of surface valley and surface peak. Therefore, the material ratio supporting the unit load is always below 100%. Load bearing surface can be determined from the material ration curve (Abbott-Firestone curve) provided using surface profilometer measurement. For example, Figure 2.7.1 shows surface profile over a certain length and the material ratio curve obtained at the typical porous surface layer.

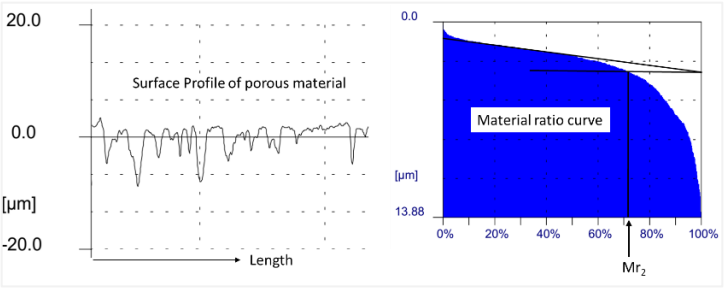

Figure 2.7.1 Surface profile and material ration curve of PM material

The valley in the surface profile represents surface pores that is not expected to support the load. The material ration curve represent the distribution of peaks, and

the load bearing surface can be determined from the curve by drawing a secant line that connecting the inflicting points of the curve, and the point of intersection with the horizontal line represents the load bearing surface.

However, the use of load bearing surface in eq. (20) depends on the type of contact conditions. For example, in lubricated contact condition lubricant may fill the valleys, and this could change the load bearing capacity of the surface. In the case of hydrodynamic lubrication contact regime, the lubricant film may support the contact load, in this condition, Mr_2 is taken as 100%.

2.7.2. Surface crack nucleation due to brittleness

Tensile stress applied on the low toughness matrix could result in the formation of brittle surface cracks. In particular, case hardened PM surface characterized by higher hardness and lower toughness, in which the presence of open pore raises tensile stress, and it also considered as cracks [26,75]. Therefore, relatively small tensile stress may be sufficient to propagate brittle cracks of the surface layer. The nucleation at the pore edges surrounded by the hard phases may be predicted using eq. (21)

$$\sigma_t > \sigma_f \tag{21}$$

where, σ_t, is the maximum tensile stress at the surface and σ_f is stress at fracture.

σ_t is given by eq. (22) [61]

$$\sigma_t = \frac{\beta_k}{Mr_2}\,\sigma_{x,t} \tag{22}$$

where, β_k is the notch effect of the surface matrix, Mr_2 is load bearing surface and $\sigma_{x,t}$ is the tangential stress at the surface.

The fracture stress σ_f is determined using eq. (23) [26]

$$\sigma_f = \frac{K_{IC}}{\psi(\pi a)^{\frac{1}{2}}} \quad (23)$$

where ψ is a geometrical factor ($1000^{0.5}$), K_{IC} is the fracture toughness of the matrix and a is the pore size. K_{IC} is related to a yield strength of the matrix and determined using eq.(24) [69]

$$K_{IC} = \frac{60000}{\sigma_y + 300} \quad (24)$$

Combining equations (21), (22), (23) and (24), a relation between the critical pore sizes that causes brittle cracking and the maximum Hertzian pressure is obtained using eq. (25)

$$a = k\left(\frac{0.78}{P_0}\right)^2 \quad (25)$$

where K is material and geometry parameter (MPa^2 m), defined by eq. (26)

$$k = 0.3183\left(\frac{K_{IC}}{2\mu}\right)^2\left(\frac{M_{r2}}{\beta_k * \psi}\right)^2 \quad (26)$$

Chapter III

3. Material and Experimental Methods

3.1. Materials

Table 3.1.1 reports the investigated materials: codes, nominal chemical compositions, and type of treatments applied to study lubricated rolling-sliding and wear damage of PM materials.

Table 3.1.1 Code, nominal composition, and applied treatments of the investigated materials

Material composition	Code	Applied treatments	Powder grade
Fe-0.85Mo-0.35C	A85Mo	- Carburized - Shot Peened	Prealloyed
Fe-1.5Mo-0.3C	AMo1		
Fe-1.5Mo-2Cu-0.65C	DDH2	- As sintered - Sinterhardened	Ni-free diffusion bonded
Fe-1Ni-1Cr-0.8Mo-0.6Si-0.1Mn-0.75C	AS4300C75	- Sinterhardened	Low-Ni diffusion bonded
Fe-0.4Ni-1.4Cr-0.8Mo-0.2Mn-0.75C	EcosintC75	- Sinterhardened	
Fe-4Ni- 0.5Mo-1.5Cu-0.3C	DAE1	- Carburized	High-Ni diffusion bonded
Fe-4Ni-0.5Mo-1.5Cu-0.5C	DAE2	- Quenched	

The powders were cold pressed in double uniaxial action compaction to obtain rings. The green parts then sintered in a belt furnace with different belt speeds and sintering temperatures. The applied belt speed is either 10 cm/min or 20 cm/min depending on density; the faster speed applied to the lower density parts.

All materials were pressed and sintered in an industrial facility by GKN Sinter Metals, Brunico, Italy.

Density (theoretical and nominal), porosity (nominal) and sintering temperature reported in Table 3.1.2.

Table 3.1.2 Density, porosity and sintering temperatures ($T_{sint.}$) of the investigated materials

Code	ρ, g/cm^3		ε, %	$T_{sint.}$, °C
	Theoretical	Nominal	Nominal	
A85Mo	7.81	7.4	5.49	1150
AMo1	7.83	7.4	5.49	
DDH2	7.79	7.0	10.18	1120
	7.79	7.3	6.33	
AS4300C75	7.64	7.3	4.46	1150
			4.46	1250
EcosintC75	7.74	7.2	6.97	1150
			6.97	1250
DAE2	7.83	7.0	10.62	1150
	7.83	7.3	6.79	
DAE1	7.86	7.0	10.98	
	7.86	7.3	7.16	

PM rings have the final dimension of 16 mm inner diameter, 40 mm outer diameter and 10 mm height. The sintered parts were submitted to additional treatments such as either through hardening or gas carburized and then stress relieved, as reported in Table 3.1.1.

The treatments were also carried out in the GKN Sinter Metals factory under the conditions of the industrial production.

The carburized prealloyed steels were ceramic shot peened in an industrial facility of 2Effe Engineering SRL, Soiano al lago (BS), Italy.

3.2. Experimental methods

Density measurements were performed by the water displacement method with weighing balance accuracy of 0.001 mg.

Before surface and subsurface microstructure characterization, all specimens contaminated by oil or lubricant were cleaned properly using ligroin for seven hours in ultrasound. Then, they were cleaned using ethanol for five minutes minimum.

Abbott Firestone curve and roughness of the die surface were analyzed using the surface profilometer. The load bearing surface (Mr_2) was determined. The surface microhardness was measured using microhardness tester of 0.1 Kg. Its value is the mean of three indentations carried out at different positions.

The maximum Feret pore diameter (D_{max}) on the die surface and the porosity were measured using the image analysis of three backscatter SEM images.

Metallographic specimens of longitudinal cross sections of the typical contact zone were prepared. The specimens were mounted in the resin, gently grounded using 220-1200 grid silica carbide polishing paper. Pores were opened using 3 μm and 1 μm slurry polishing. The optical microscope was used to collect images from unetched microstructure for pore parameter analysis. Three images were collected for each material within a surface layer 400 μm deep. The selection of this depth size relates to the position of Hertzian equivalent stress, that often maximum up to this depth. The subsurface pore parameters such as porosity (ε), pore area, perimeter (P), equivalent pore diameter ($D_{eq.}$) and maximum pore diameter (D_{max}) were characterized by using Image analysis on unetched microstructure. The following procedures were followed to measure pore parameters along the cross-sections.

- First, pore parameters were measured on the three adjacent micrographs from the surface up to 100 μm depth.
- Then, the same pore parameters were collected from 100 μm to 200 μm, 200 μm to 300 μm and from 300 μm to 400 μm.
- Additional pore parameter, f_{circle}, was determined for each pore size using eq. (27)

$$f_{circle} = \frac{4\pi A}{P^2} \quad (27)$$

- Mean value of the f_{circle} using the whole pore population and the bigger pore size of 100%, 10% and 5% corresponding to the whole pore population was calculated.

The etched microstructures were prepared and the reagent applied to reveal the microstructure was 5% of Nital. Microhardness (HV0.1) was measured on these microstructures. The two following approaches were applied during the indentation:

a. Three indentations carried out randomly, with the gap between at least three times of diagonal indent lengths, up to the total 1 mm thick.
b. The measurement was carried out locally, that is simply by searching each microstructural constituents in particular for the heterogeneous diffusion bonded materials.

The surface residual stress and retained austenite profiles of carburized and shot peened specimens were measured by X-ray diffraction by 2Effe Engineering. The measurement conditions listed in Table 3.2.1.

Table 3.2.1 X-ray diffraction measurement conditions of residual stress and retained austenite of carburized and shot peened prealloyed steels

Incident Radiation	Cr Kα	Elementary Cell	Cubic
Filter	Vanadium	Miller's Index (hkl)	211
Diffractometer configuration	ω	Multi-regression	Yes
Detector type	30°	Background subtraction	Polynomial
Detector's angle range	Strip	2θ position	Free
Acquisition time	30 s	2θ angle	156.33°
Oscillation range	+/-40°	Young modulus	208000 MPa
Number of Ψ angles used	7	Poisson coefficient	0.28
Selection of Ψ	Automatic	Power supply	33 kV
Measurements method	Static	Current the tube's	85 μA
Materials	Steel	Collimator's diameter	1 mm

The measurement was takes placed within the interval of 50 μm up to 250 μm depth from the surface. Shot peening and the analysis of residual stresses and retained austenite were carried out.

Several lubricated rolling-sliding tests were carried out on disk to disk configuration using an Amsler tribometer. Figure 3.2.1 shows the Amsler apparatus with the contacting rings.

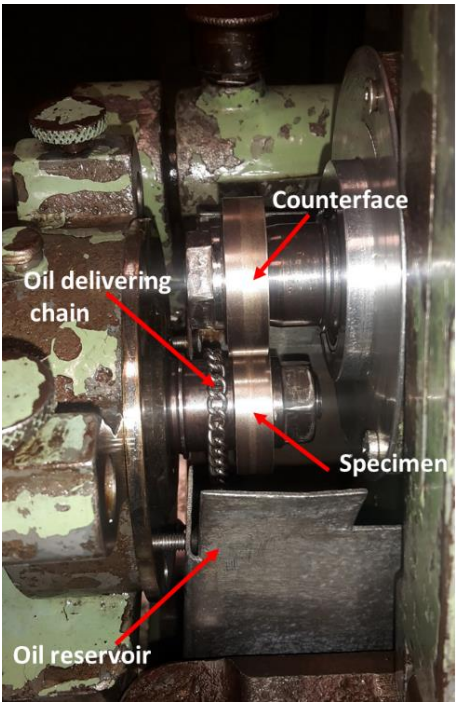

Figure 3.2.1 Amsler Tribometer and contacting rings

The lubricant used was Castrol edge 5W-30. It was stored in the reservoir oil tank and continuously delivered to the contact surface by the oil delivering chain. Contact fatigue tests were performed at different mean Hertzian pressures with respect to the reference pressure (the theoretical resistance to the contact fatigue crack nucleation) that was determined by the theoretical analysis. The specimen and the counterface disks rotate with an angular velocity of 400 rpm and 360 rpm, respectively. This velocity difference results in a 10% sliding. This type of contact condition resulting in the highest possibility of surface pitting of the contacting surfaces [52]. The tests run up to one million cycles. The coefficient of friction was recorded during the whole test.

After contact fatigue tests, the microstructure of the worn discs was investigated. Using SEM and optical microscope, the presence of cracks in the surface and

subsurface region was investigated. Figure 3.2.2 shows a schematic representation of contact configuration and techniques of sectioning for metallographic preparation.

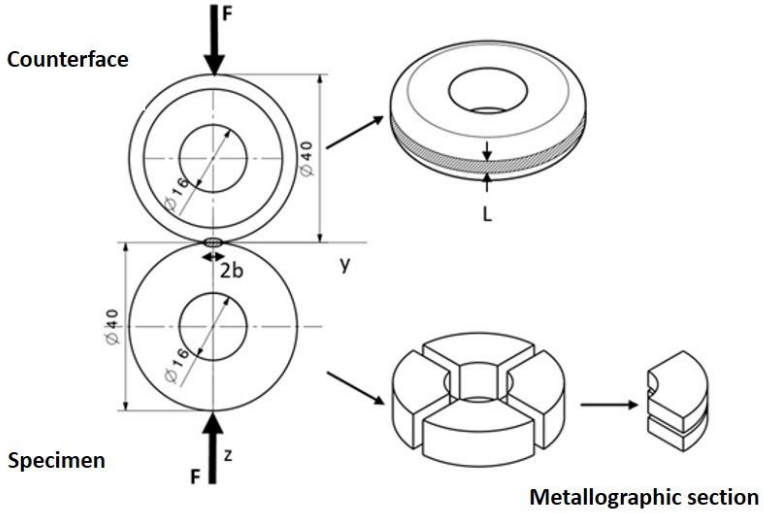

Figure 3.2.2 Contacting surfaces configuration and the procedure that shows sample sectioning

Counterface disk is a heat treated 52100 bearing steel. The important properties are reported using Table 3.2.2.

Table 3.2.2 Properties of counterface disc (bearing steel)

Material	Nominal composition	E (GPa)	ρ, g/cm^3	HRc	ν
Bearing steel	Fe-1.5%Cr-1%C	210	7.81	60-65	0.3

The dimension and geometric characteristics of counterface disk are the same as a sintered specimen. Since the maximum available force of the Amsler apparatus is about 2000 N force, the counterface disk surface was chamfered to reduce contact length (L) to increase the mean pressures applied to the specimens.

The relationship between applied load and contact length were analyzed by considering the specimen elastic modulus (155 GPa), specimen Poisson's ratio (0.27), and the variable contact length of counterface disk (L). Figure 3.2.3 represents the mean Hertzian pressure versus the force at a variable contact length.

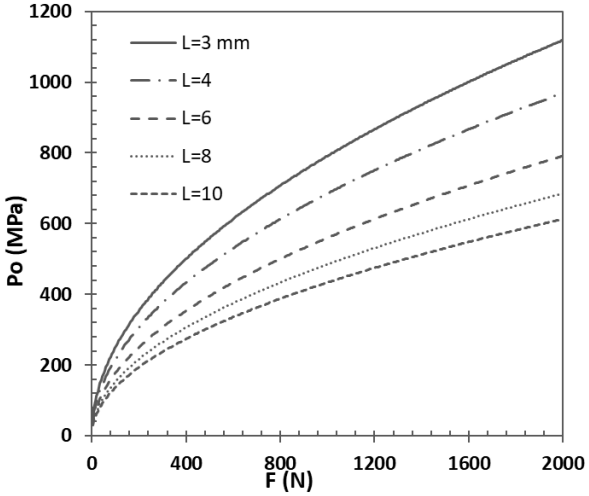

Figure 3.2.3 Mean pressure at different contact lengths

As the contact length decrease from 10 mm to 3 mm (the minimum length), the corresponding mean pressure increases. With the maximum available load 2000 N and the contact length 3 mm the mean Hertzian pressure could rich about 1150 MPa.

Since elastic modulus of the porous material varies with porosity, its effect on the mean pressure was evaluated. Figure 3.2.4 represents the mean pressure as a function of elastic modulus (specimen) determined at different applied loads with 3 mm contact length.

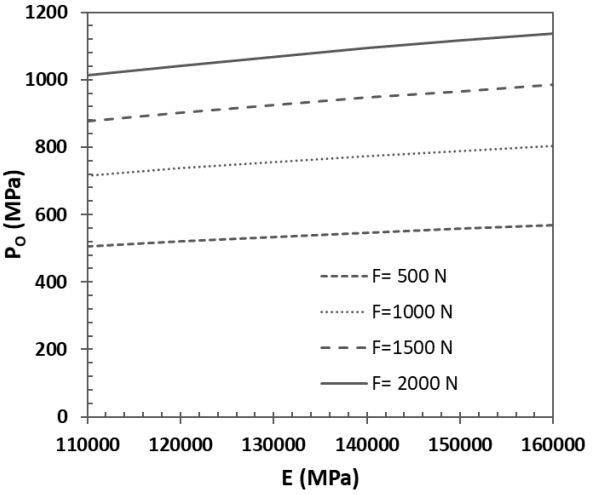

Figure 3.2.4 The effect of elastic modulus of the spacemen on the mean pressure at different applied loads

At the given force and contact length, the mean pressure shows only slightly increases with elastic modulus.

Chapter IV

4. Results and Discussion

4.1. Prealloyed steels: effect of Mo content of carburized steels and shot peening

Shear and equivalent stress failure criteria are used to predict the formation of subsurface cracks during rolling-sliding contact [66,76]. In theory shear stress approach is more conservative and equivalent stress approach (maximum distortion strain energy criterion) is more accurate to predict crack nucleation; however, due to the peculiarity of PM materials, both approaches were verified.

Moreover, the effect of molybdenum content on lubricated rolling-sliding contact fatigue and surface damage resistance was studied. The addition of Mo influences the mechanical property without influencing the powder compressibility and dimensional precision of the parts. In particular, the higher hardenability factor of this element contributes a positive change of matrix properties. Tailoring Mo addition is very common in the industry to minimize the costs of Mo that rises continuously in the market. Here two different additions: 0.85%Mo (A85Mo) and 1.5%Mo (AMo1), were considered and the influence on the formation of subsurface cracks was studied using the two failure criteria approaches. The two steel were carburized and shot peened.

However, the combination of high hardness, which attained through carburizing, and the presence of residual pores (usually irregular in shape) may promote the formation of brittle surface cracking. The effect was studied in [75,77] and shows that the pore in a porous material acts as pre-existing cracks when the matrix microhardness exceeds a threshold. The formation of the brittle cracks depends on the pore size and the tensile stress. Therefore, in addition to the main damage mechanisms of subsurface crack nucleation, brittle surface crack nucleation due to surface tensile stresses was also studied.

In this part, - lubricated rolling-sliding damage of a gas carburized prealloyed Fe-0.85%Mo- 0.25%C and Fe-1.5%Mo-0.2%C sintered steel was investigated. The occurrence of both subsurface and surface damage were analyzed theoretically, and rolling-sliding contact fatigue tests were carried out to confirm the theoretical predictions.

4.1.1. Rolling-sliding contact fatigue and wear damage of carburized materials

Surface characteristics, such as hardness (HV10), microhardness (HV0.1), load bearing surface (Mr2), mean roughness (R_a) and core roughness depth (R_k) of the two carburized materials were measured and reported in Table 4.1.1.

Table 4.1.1 Surface characteristics of carburized rings measured at the contact surface

Material	HV10	HV0.1	Mr_2 (%)	R_a (µm)	R_k (µm)
A85Mo	649	848	82.8	-	1.2
AMo1	673	845	81.5	-	1.0

Figure 4.1.1 shows unetched microstructure of the carburized prealloyed steels.

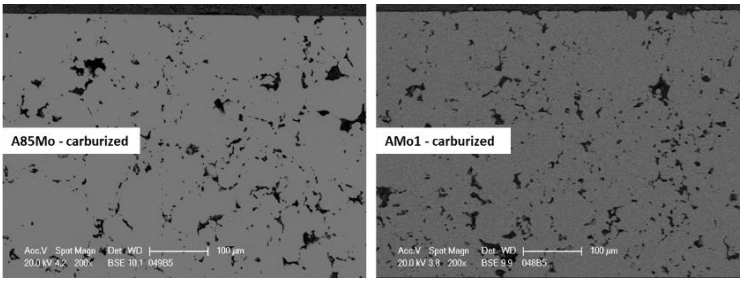

Figure 4.1.1 Unetched microstructure of carburized materials prepared using backscatter electron scanning image

This image was used to measure pore parameter by image analysis. Figure 4.1.2 shows the profiles of fractional porosity (ε), pore shape factor (f_{circle}), elastic modulus (E) and the fraction of load bearing sections (Φ).

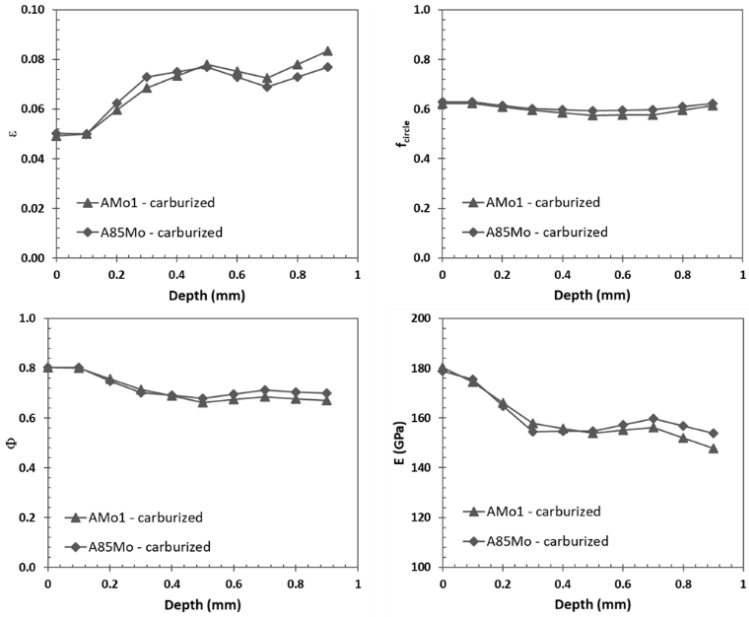

Figure 4.1.2 Profiles of pore parameters and material property: ε, f_{circle}, Φ, and E

Porosity is lower at the surface and increases to the bulk. The porosity of the two materials is almost the same. The pore shape factor corresponding to the whole pore population shows very little variation along the depth and is still the same for the two materials. The fraction of load bearing sections was determined from the mean value of the pore shape factor and the porosity distribution. The mean value of the fraction of load bearing sections is 0.78 for A85Mo and 0.77 for AMo1. Elastic modulus was determined from the fraction of load bearing section and the elastic modulus of pore free material using eq. (28) [70].

$$E = E_o \, \Phi^{0.5} \qquad 28$$

where, E is the elastic modulus of the porous material, E_o is the elastic modulus of pore free material, which is 210 GPa, and Φ is a fraction of load bearing sections. For the two materials, Φ and E increases towards the surface because of the decreasing of porosity and slight increasing pore shape factor.

Figure 4.1.3 shows etched microstructure of the carburized A85Mo and AMo1 materials observed at SEM in a backscatter mode.

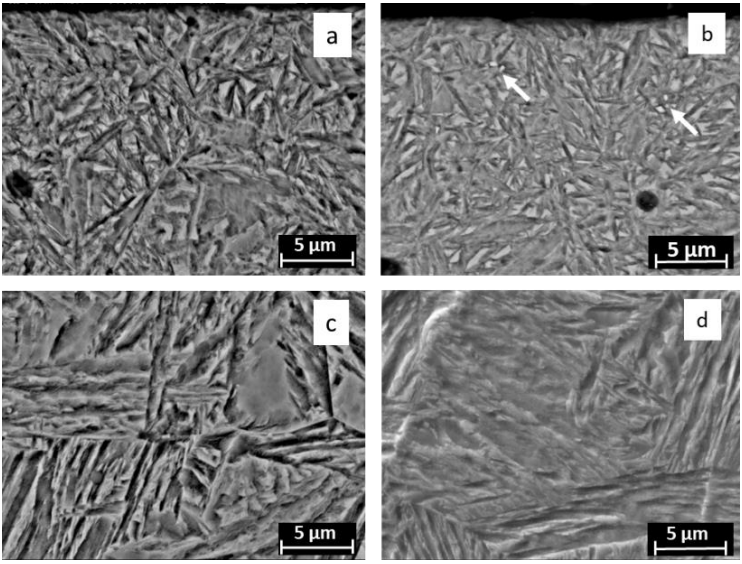

Figure 4.1.3 Microstructure of the carburized A85Mo (a, c) and AMo1 (b, d) steels: surface (a, b) and core (c, d)

The main microstructural constituent of the surfaces are plate martensite and retained austenite between plates, while the bulk microstructure is the mixture of lower bainite and martensite. At the surface of AMo1 carburized steel, a few white micro carbides were observed, as indicated by the white arrow. To observe carbide formation, elements are mapped and shown in Figure 4.1.4. Carbide particles were highlighted using the blue circular dotted lines.

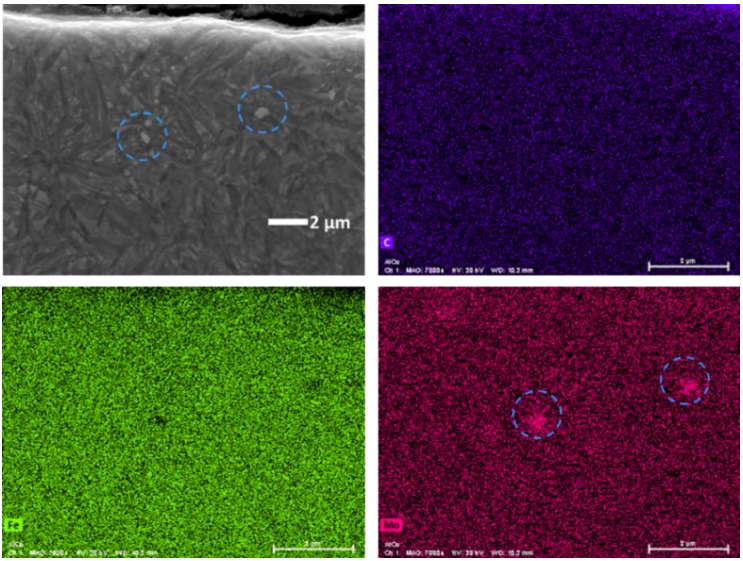

Figure 4.1.4 Element mapping of Fe-1.5%Mo-0.2%C carburized material using EDX analysis

The local concentration of Mo confirms the formation of carbides. These carbide particles are very fine, and the effect on the contact fatigue crack formation is negligible.

The amount of retained austenite and the residual stress induced by carburizing were measured. Figure 4.1.5 shows the profile of retained austenite and the residual stresses of the carburized rings.

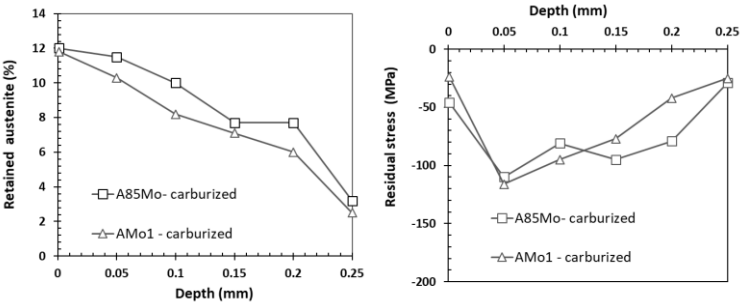

Figure 4.1.5 Retained austenite and residual stress profiles of carburized materials

The amount of retained austenite is 12% at the surface and decreases moving towards the bulk. The compressive residual stress induced by carburizing and heat treatment is maximum at about 0.05-0.1 mm, and it is about -120 MPa. The maximum residual stress depth is small. The influence on the reduction of stress at Hertzian depth will be weak.

Figure 4.1.6 shows the microhardness profiles of carburized rings. Microhardness profiles are typical of a carburized steel, with a case depth of about 800 μm (d_{550HV}) thickness.

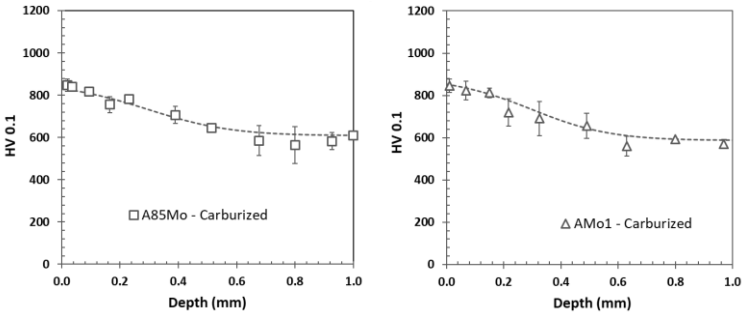

Figure 4.1.6 Microhardness profiles of carburized A85Mo and AMo1 steel

The dotted line represents the theoretical microhardness profile of martensite produced by carburizing. The analysis needs the data of gas carburizing, such as carbon potential (0.8 wt. %.) of the carburizing atmosphere, carburizing time (155 min), carburizing temperature (860 °C), and C concentration in the bulk. Also, the diffusion coefficient of C was determined using the model proposed in [78], and carbon profile along the depth was determined using the equation proposed in [79]. Then carbon profile converts to the microhardness profile by correlating with the data available in the literature [30].

Figure 4.1.7 shows the results of the theoretical analysis of the subsurface cracks in the carburized rings, using the shear stress and the equivalent stress approach. The calculation was made to determine the mean Hertzian pressure P_o at which plastic

deformation is expected to occur. This value is the theoretical resistance of the carburized material to the formation of contact fatigue subsurface cracks.

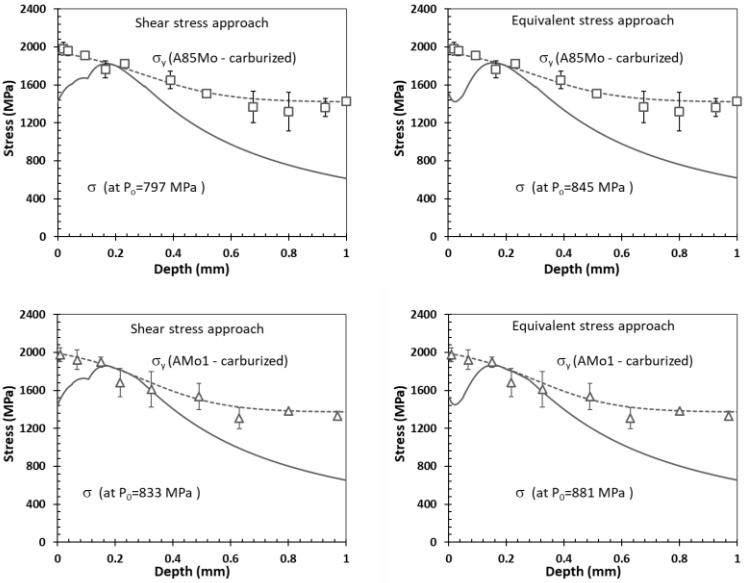

Figure 4.1.7 Comparison between the maximum stress (σ) and the matrix yield strength (σ_y) profiles of carburized steels: shear and equivalent stress approaches

The theoretical resistance of the carburized A85Mo steel is 797 MPa and 845 MPa according to shear stress and equivalent stress failure criteria approach, respectively. The theoretical resistance of carburized AMo1 steel is 833 MPa and 881 MPa according to shear stress and equivalent stress failure criteria approach, respectively. Equivalent stress approach increases the mean pressure by 6% from shear stress approach. The amount of Mo has no significant effects on the theoretical resistance of the material.

Lubricated rolling-sliding tests were then carried out at different mean pressures on the two materials.

According to the reference mean pressures calculated using shear and equivalent stress approach the following three mean pressures were applied on A85Mo carburized steel.

- 750 MPa, lower than the theoretical resistance with both the approaches; no subsurface cracks are expected;
- 830 MPa, intermediate between the theoretical resistances with the two approaches;
- 950 MPa, higher than the theoretical resistance with both the approaches; subsurface cracks are expected.

Test at 830 MPa was aimed at concluding which of the two approaches is more reliable in the prediction of the resistance. Figure 4.1.8 shows the backscatter SEM images of the worn specimens.

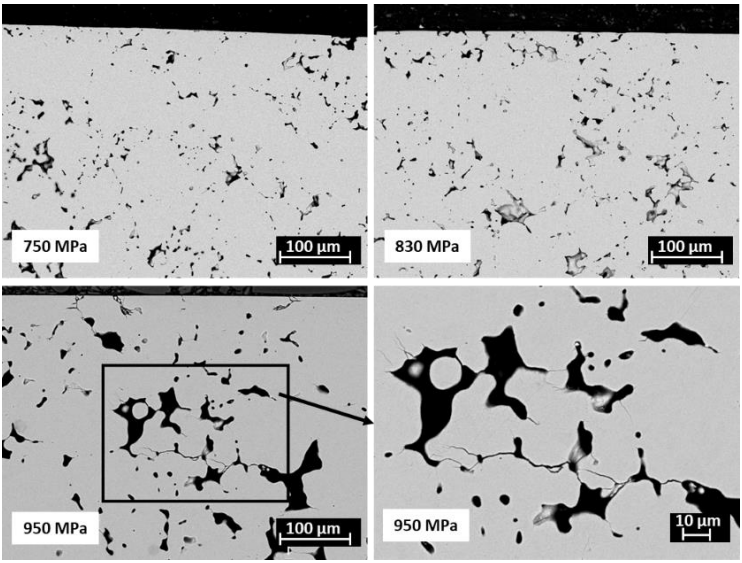

Figure 4.1.8 The microstructure of the carburized worn A85Mo material tested at different mean pressures

Subsurface cracks were observed only on the rings tested at 950 MPa. Therefore, the evidence is in agreement with the theoretical approach based on the equivalent stress failure criteria approach.

In addition to subsurface cracks, surface cracks were observed at 830 MPa and 950 MPa, as shown in figure 4.1.9. The observed cracks at 950 MPa are typical brittle surface cracks.

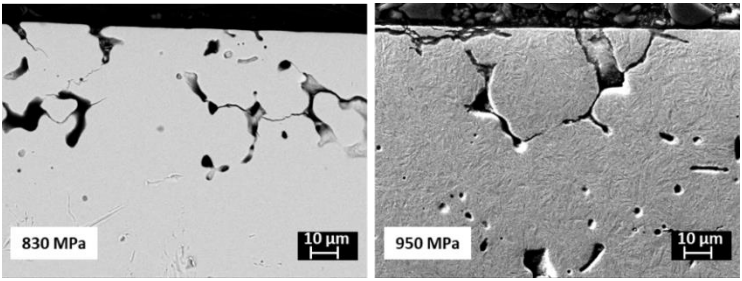

Figure 4.1.9 The microstructure of the carburized worn A85Mo material tested at different mean pressures showing surface cracks

These surface initiated brittle cracks are predicted simply by comparing critical crack length (a), that is calculated using eq. (25), with measured pore sizes (half of maximum Feret diameter) on carburized surfaces. Figure 4.1.10 represents backscattered SEM image of carburized A85Mo surface with the distribution of the surface pore maximum Feret diameters, which was measured by Image analysis.

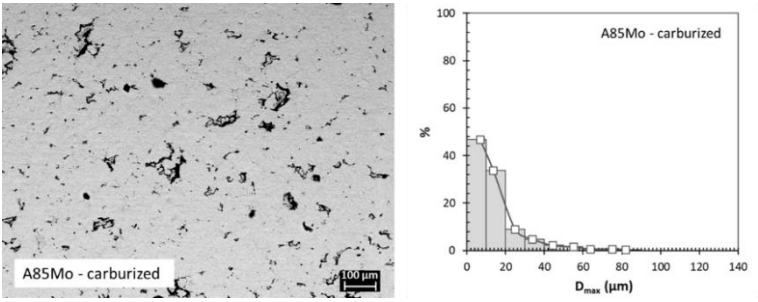

Figure 4.1.10 Top surface view of carburized A85Mo ring and surface pore Feret diameter distribution

Figure 4.1.11 is the graphical representation of the theoretical analysis of the brittle surface crack formation. The critical pore size responsible for surface crack nucleation was calculated and plotted along with the tensile stress. Both critical pore size and tensile stress are a function of the mean pressure. The friction coefficient measured during the tests, and it is 0.014 (representative for all tests). The higher the mean pressure, the higher the tensile stress and the smaller the pore size that is expected to cause the formation of a surface cracks.

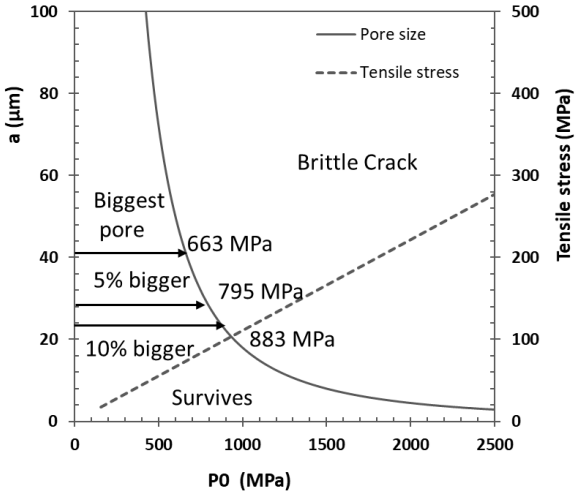

Figure 4.1.11 critical pore size responsible for surface crack nucleation and tensile stress as a function of the mean pressure for the carburized A85Mo steel

The mean pressure at which the brittle surface cracks are expected to nucleate is calculated using the biggest pore size, the pore size of the bigger pores accounting for 5% and 10% of the pore population. Accordingly, 5% of the bigger pore population predicts better than others the behavior of the material.

In the case of carburized AMo1 steel, referring to the mean pressures that are calculated using the shear and equivalent stress approaches, three test mean pressures were applied:

- 800 MPa, lower than the theoretical resistance with both the approaches; no subsurface crack are expected;
- 850 MPa, intermediate between the theoretical resistances with the two approaches;
- 945 MPa, higher than the theoretical resistance with both the approaches; subsurface cracks are expected.

Test at 850 MPa was aimed at concluding which of the two approaches is more reliable in the prediction of the resistance. Figure 4.1.12 shows the microstructure of the worn specimen observed at SEM.

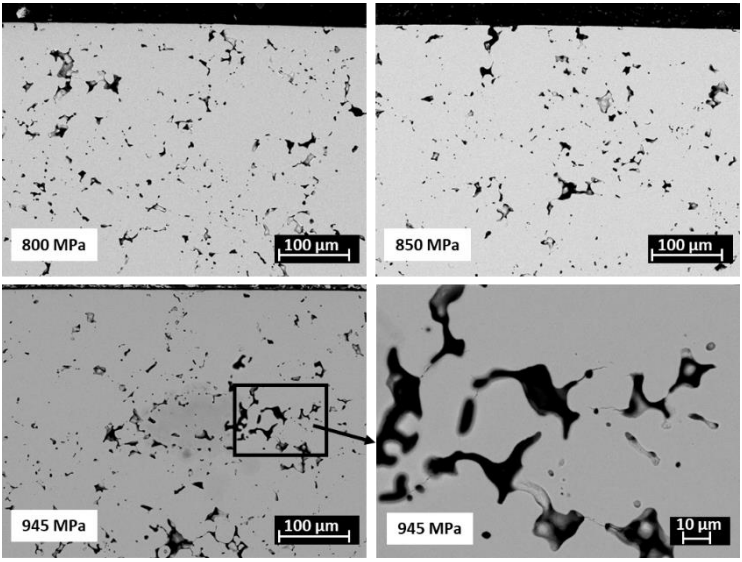

Figure 4.1.12 the microstructure of the carburized worn AMo1 material tested at different mean pressures

Subsurface microcracks were observed only on the ring tested at 945 MPa. Again, this is in agreement with the equivalent stress failure criteria approach.

Some brittle surface cracks were observed on the carburized AMo1 surface due to the residual open porosity and high surface hardness provided during carburizing. An

additional contact fatigue test was carried out at 672 MPa to validate surface initiated cracks. Figure 4.1.13 represents worn microstructure of AMo1 steel tested at all test pressures.

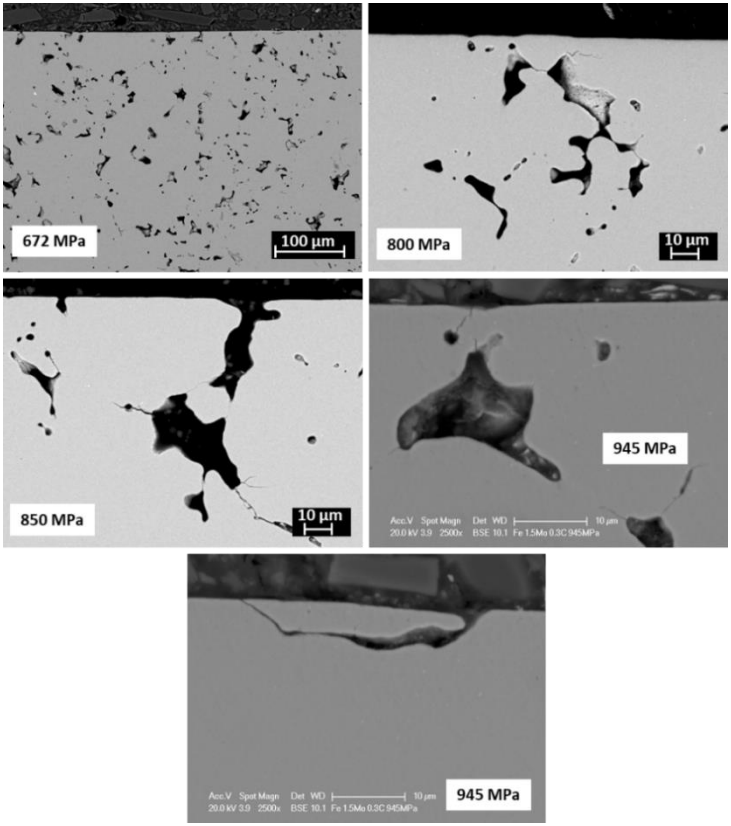

Figure 4.1.13 The microstructure of the carburized worn AMo1 steel tested at different mean pressures

No surface cracks were observed at 672 MPa. But surface cracks were observed at all other test pressures. For instance, short micro cracks were observed at 800 MPa, and the number of crack increases with pressure. At 850 MPa crack grows along the pore connectivity and at 945 MPa micro pitting was observed.

The nucleation of surface cracks are predicted theoretically by comparing half of the maximum Feret diameter with the critical pore size (determined using eq. (25)). Maximum Feret diameter of the open pore was measured using Image analysis on the three SEM images as shown in figure 4.1.14.

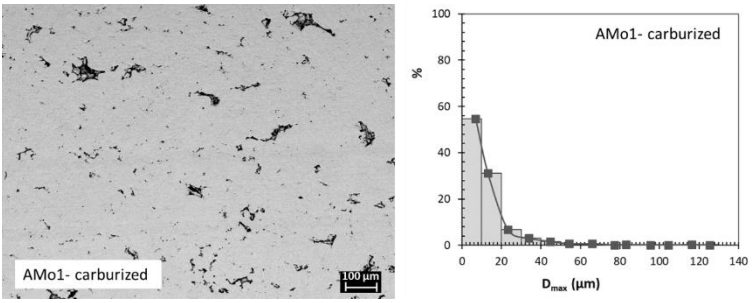

Figure 4.1.14 Surface of the carburized AMo1 steel and Feret diameter distribution

The mean pressure at which the brittle surface cracks are expected to nucleate is determined using figure 4.1.15 from the biggest pore size, the size of the bigger pores accounting for 5% and 10% of the pore population.

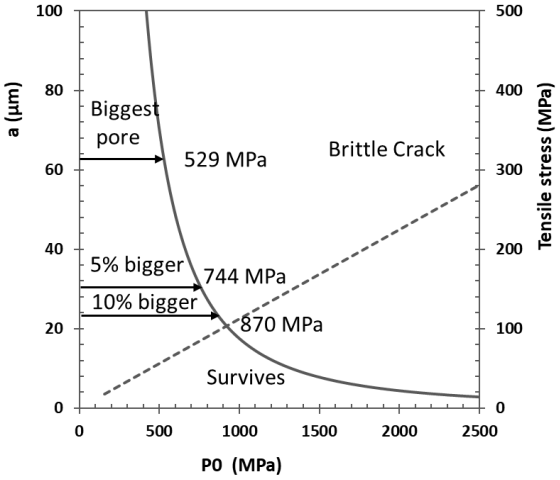

Figure 4.1.15 critical pore size responsible for surface crack nucleation and tensile stress as a function of the mean pressure for the carburized AMo1 steel

The comparison between theoretical and experimental results indicate that the resistance to surface cracking during lubricated rolling-sliding tests properly predicted form the size of the bigger pores accounting for 5% of the pore population.

4.1.2. Effect of shot peening

Table 4.1.2 reports measured surface characteristics, such as hardness (HV10), microhardness (HV0.1), load bearing surface, the surface roughness (R_a) and core roughness depth (R_k) of the two shot peened materials.

Table 4.1.2 Surface characteristics measured at the contact surface of shot peened rings

Material	HV10	HV0.1	Mr2 (%)	R_a (µm)	R_k (µm)
A85Mo	707	928	83.6	0.3	1.4
AMo1	693	967	83.2	0.2	0.6

The effect of shot peening on the contact fatigue and wear damage due to surface densification, accumulation of compressive residual stress, and strain hardening was investigated. Figure 4.1.16 represents unetched microstructure of shot peened steels.

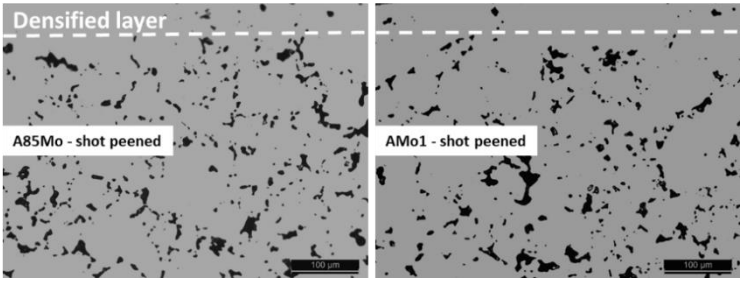

Figure 4.1.16 Unetched microstructure of the shot peened A85Mo, and AMo1 rings prepared using an optical microscope

Shot peening promotes densification about 50 µm to 70 µm thick surface layers. The densification mostly relates to the deformation of the softer austenite between

martensitic plates. Figure 4.1.17 represents the retained austenite and residual stress measured on shot peened specimens.

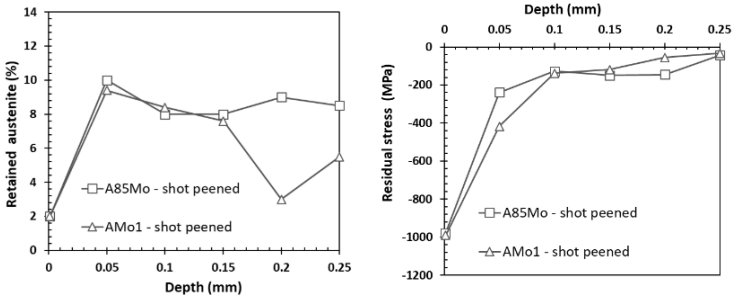

Figure 4.1.17 Retained austenite and residual compressive stress of shot peened spacemen

Due to the stress/strain induced transformation of austenite into the martensite, the amount of retained austenite is lower at the surface. Shot peening also introduces higher compressive stress at the surface and decreases moving to the depth.

Using three different adjacent images as represented in Figure 4.1.16, pore parameter were analyzed using image analysis. Figure 4.1.18 shows the profiles of fractional porosity, pore shape factor, elastic modulus and a fraction of load bearing sections.

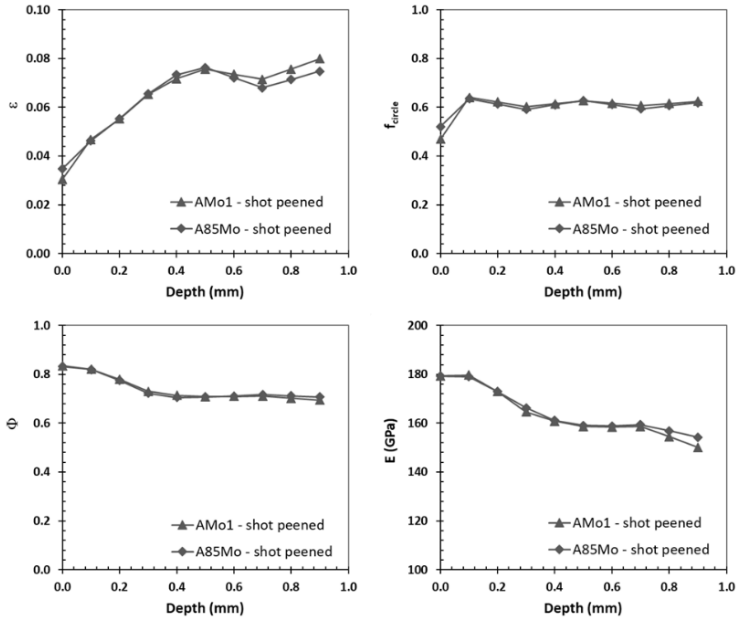

Figure 4.1.18 Profiles of pore parameters and material property: ε, f_{circle}, Φ, and elastic modulus

Shot peening shows a significant effect to reduce the surface porosity. The depth of shot peening penetration is not distinguished, but smaller surface pores of carburized material eliminated effectively. The pore shape factor is also lower at the surface due to the collapsing of pore after shot peening. The fraction of load bearing sections was calculated using the median value of the pore shape factor and porosity profile given by eq. (17). It increases towards the surface because of the lower porosity at the surface. The effect of shot peening on the pore parameters and property of A85Mo and AMo1 are similar.

Figure 4.1.19 represents the microstructure of shot peened materials. The microstructure is martensitic with a few retained austenite observed between martensite plates. Apart from the amount of austenite, the microstructure of shot peened surface is similar to that of the carburized surface (Figure 4.1.3).

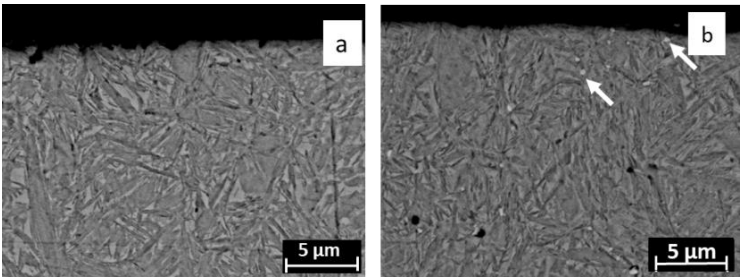

Figure 4.1.19 Microstructure of the shot peened materials: A85Mo (a) and AMo1 (b) steels

The microhardness of shot peened microstructure was measured. Figure 4.1.20 shows microhardness profile of shot peened rings.

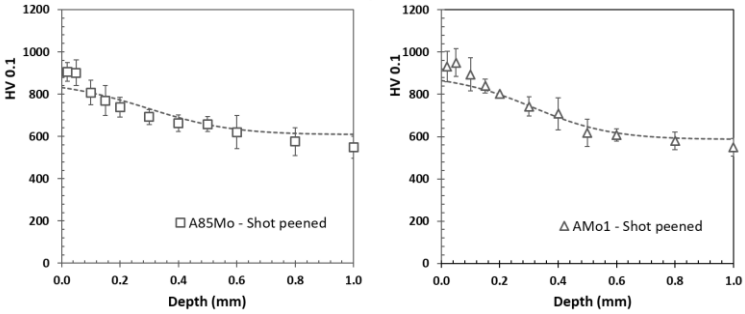

Figure 4.1.20 Microhardness profiles of shot peened A85Mo and AMo1 steels

The dotted line is the theoretical microhardness of carburized martensite. Microhardness is higher only at the very near surface due to strain hardening induced by shot peening, which is above the theoretical microhardness of carburized surface.

Following the same procedure as carburized materials, the theoretical resistance of shot peened surface determined. Figure 4.1.21 shows the results of the theoretical calculation of the resistance to subsurface contact fatigue damage of the shot peened materials.

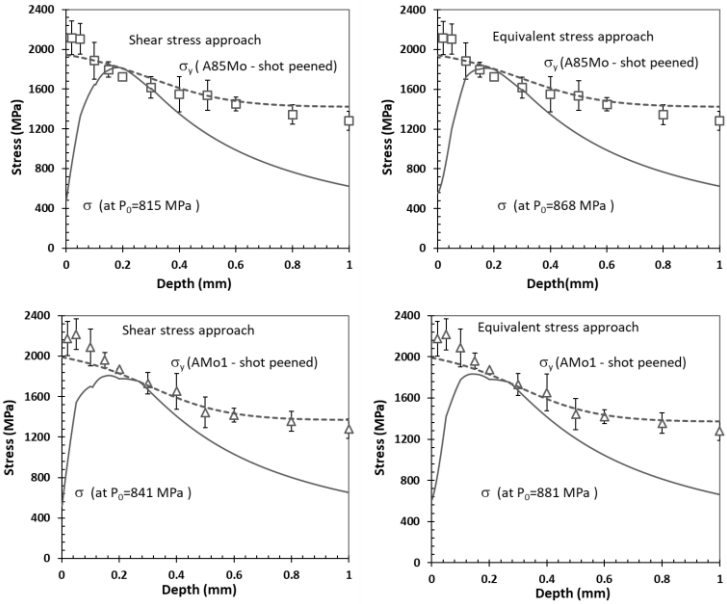

Figure 4.1.21 Comparison between the maximum stress (σ) and yield strength (σ_y) profiles of shot peened matrix

The theoretical resistances of the shot peened A85Mo steels is 815 MPa and 868 MPa according to the shear stress and the equivalent stress failure criteria approaches, respectively. The theoretical resistance of the carburized AMo1 steel is 841 MPa and 881 MPa according to the shear stress and the equivalent stress failure criteria approaches, respectively. Since the compressive residual stress at the Hertzian depth is quite small (Figure 4.1.17), shot peening shows no effect on the resistance to subsurface crack nucleation. The theoretical resistance to contact fatigue cracks of shot peened material is similar to the carburized material.

While the penetration of compressive stress and strain hardening is not deep enough, the effect of compressive stress induced at the surface is very high. That increases the resistance to surface wear damage. Similar to the subsurface crack prediction, the brittle surface crack formation was predicted theoretically using brittle fracture model.

Figure 4.1.22 shows backscattered electron scanning image of the top surface of shot peened rings.

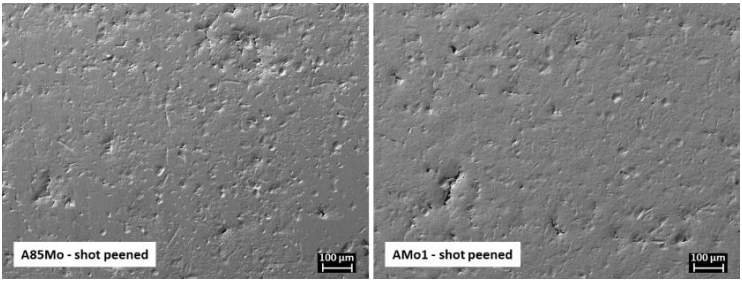

Figure 4.1.22 Top surface view of the shot peened rings

Shot peening generates rough surface topology with few collapsed open pores. Because of the surface densification by shot peening, the size of the pore is much smaller than the carburized rings.

The maximum Feret diameter of pore was measured using image analysis, and the distribution shown in Figure 4.1.23.

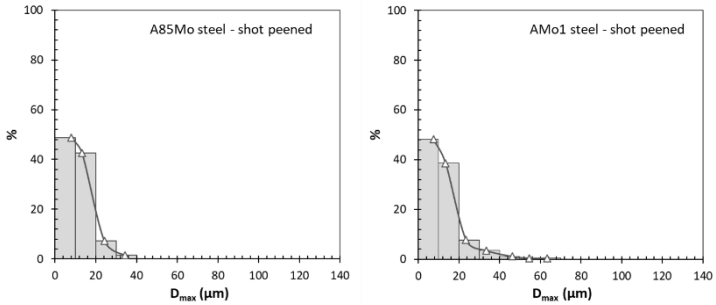

Figure 4.1.23 Distribution of Feret diameter of surface pore measured using image analysis

The half of maximum Feret diameter of the bigger pores accounting for 5% and for 10% of the pore population are determined. It is then compared with the critical crack length or pore size responsible to the formation of brittle cracking. Moreover, the deformation of the surface deteriorates the surface profile, resulting in a higher

friction coefficient (μ=0.04-0.1). But the main effect of shot peening is the decrease of the surface tensile stress, as shown in figure 4.1.24.

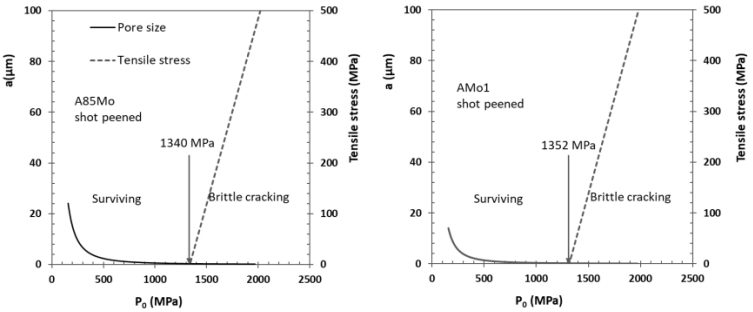

Figure 4.1.24 Critical pore size responsible for surface crack nucleation and tensile stress as a function of the mean pressure for the shot peened materials

Surface compressive residual stresses could cancel the tensile stress, which starts increasing when the mean pressure reaches 1340 MPa and 1352 MPa on A85Mo and AMo1 steels, respectively. Although the pore size on the shot peened surface is higher than the critical one corresponding to 1340 MPa and 1352 MPa (less than 1 μm), tensile stress is zero and not able to form the surface cracks. Therefore no surface cracks are expected below such mean pressure. If mean pressure exceeds these pressures, surface cracks nucleate.

Subsurface and surface crack nucleation on shot peened materials were investigated by carried out lubricated rolling-sliding contact tests at different mean pressures. Figure 4.1.25 shows the microstructure of the shot peened A85Mo steel tested at:

- 830 MPa (higher than the theoretical resistance based on the shear stress approach but lower than the theoretical resistance based on the equivalent stress approach) and,
- 950 MPa (higher than the theoretical resistance based on shear and equivalent stress approach) mean pressures.

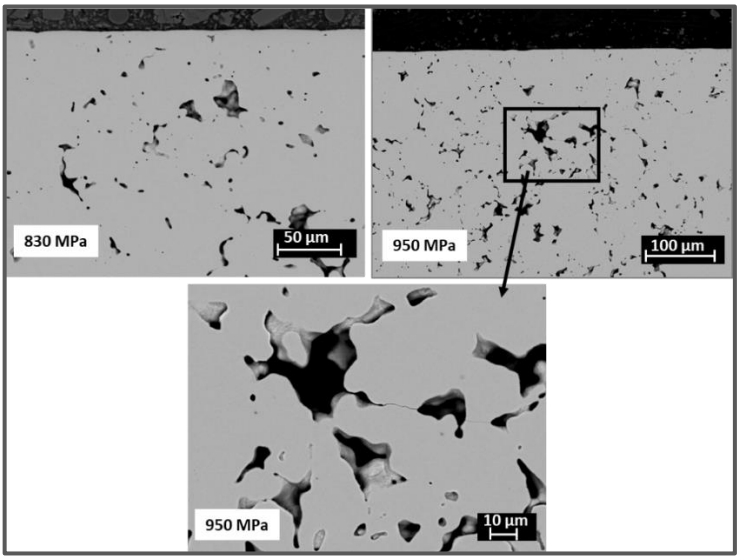

Figure 4.1.25 Microstructure of worn shot peened A85Mo specimens at the corresponding 830 MPa and 950 MPa test pressures

Subsurface cracks were not observed at 830 MPa, while at 950 MPa the subsurface cracks were observed. The shot peened surface does not show surface cracks at the two test pressures. The surface resistance to the formation of cracks may relate to the presence of higher residual stress and strain hardening. The observed result is in agreement with the theoretical calculation, which predicts no surface cracks up to 1340 MPa mean pressure.

Similar to A85Mo, AMo1 shot peened steel tested at different mean pressures. Figure 4.1.26 shows the microstructure of worn shot peened AMo1 steels tested at:

- 850 MPa (higher than the theoretical resistance based on the shear stress approach and lower than the theoretical resistance based on the equivalent stress approach) and,
- 1100 MPa (higher than the theoretical resistance based on shear and equivalent stress approach) mean pressures.

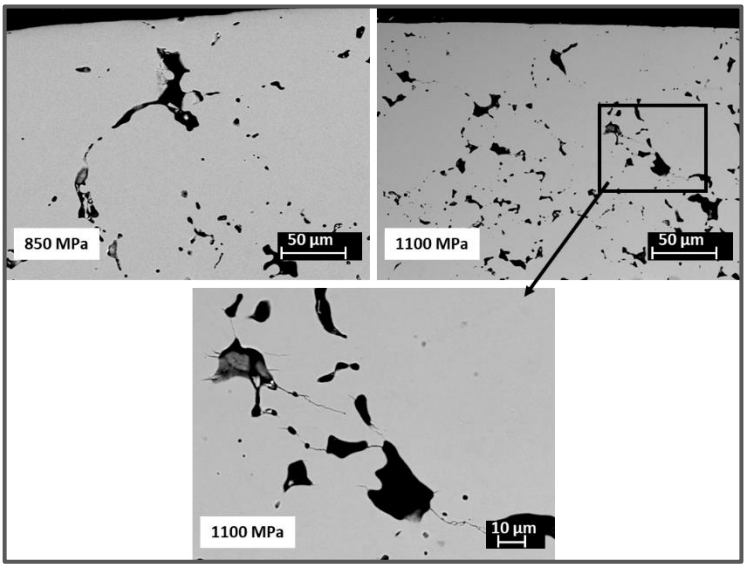

Figure 4.1.26 Microstructure of the shot peened worn AMo1 specimens tested at 850 MPa, and 1100 MPa mean pressures

Subsurface cracks were not observed at 850 MPa. However, at higher pressure 1100 MPa, subsurface cracks were observed. The higher pressure produces a higher number of cracks: most of them were nucleated at the pore edges and grows along the pore connectivity, which are inclined to the contact surface. But no surface cracks were observed at the test pressures. All the experimental evidence is in agreement with the theoretical calculation.

4.2. Ni-free diffusion bonded steel: effect of sinterhardening and density

In this paragraph, the effect of density and sinterhardening on the contact fatigue damage of Cu bonded prealloyed Fe-Mo PM steel was investigated. Porosity, microstructure and microstructural heterogeneity play a significant role in the resistance to contact fatigue crack nucleation. Aiming to improve the contact fatigue and wear damage, densifying and sinterhardening are most common techniques applied to PM structural parts. Densifying reduces pore size and fractional porosity

that reduce local stress field and improves the fraction of load bearing sections. An additional cost effective sinterhardening produces martensitic microstructure, which increases the matrix yield strength and subsequently improves the resistance to plastic deformation.

The contact fatigue of DDH2 sinterhardened material was investigated only considering the subsurface cracks preceded by local plastic deformation [44]. In the present work, the effect of friction and surface shear stress on the occurrence of surface plastic deformation studied.

In this section, rings from Fe-1.5%Mo-2%Cu-0.6%C (DDH2) steel, with target densities of 7.0 g/cm^3 and 7.3 g/cm^3, were prepared. They produced in the sintered and sinterhardened conditions. Subsurface and surface cracks at the pore edge were predicted by comparing yield strength of the matrix constituents with Hertzian equivalent stress and surface stress, as proposed using eq. (14) and eq. (20), respectively. The allowable mean pressure at which the material could resist a contact fatigue crack formation was estimated, then validated experimentally by carried out rolling-sliding contact fatigue tests.

Table 4.2.1 reports density and mechanical properties (measured by tensile tests) of sintered and sinterhardened materials.

Table 4.2.1 Density and mechanical properties of sintered and sinterhardened materials

Material	Treatment	ρ (g/cm^3)	σ_y (MPa)	UTS (MPa)	E (GPa)
Fe-1.5Mo-2Cu-0.6C (DDH2)	sintered	7.0	562	695	120
		7.3	581	781	157
	sinterhardened	7.0	809	941	120
		7.3	979	1071	157

After longitudinal sectioning of the rings, the microstructure was observed at SEM. The unetched microstructure of 7.0 g/cm^3 and 7.3 g/cm^3 sintered and the sinterhardened material are illustrated in Figure 4.2.1.

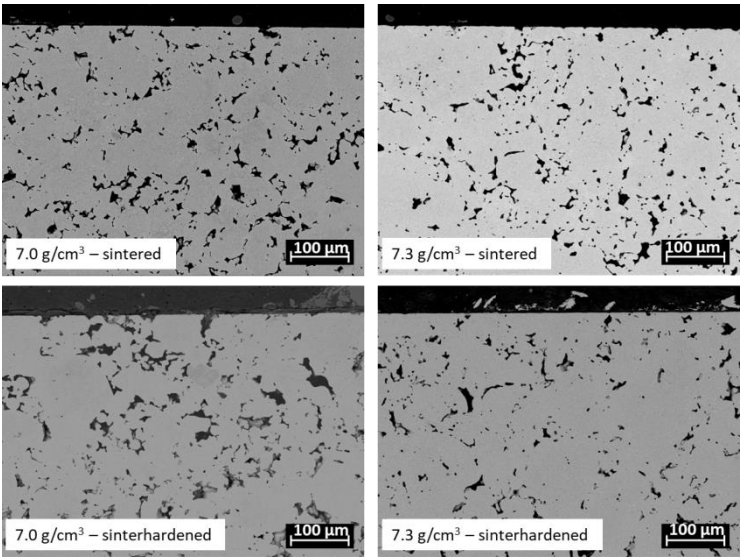

Figure 4.2.1 Unetched backscatter electron scanning microstructure of sintered and sinterhardened materials

Qualitatively, the size of the pore is bigger on the lower density steel, and relatively smaller on the higher density steel. Table 4.2.3 reports the quantitative analysis of porosity (ε), f_{circle} (corresponding to the whole pore population), ρ and Φ.

Table 4.2.2 Density and pore parameters measured from an image analysis

Treatment	ρ (g/cm³)		ε		f_{circle}	Φ
	nominal	measured	nominal	measured		
Sintered	7.0	6.98	0.10	0.11	0.58	0.57
	7.3	7.26	0.06	0.07	0.62	0.73
Sinterhardened	7.0	7.04	0.10	0.10	0.57	0.58
	7.3	7.23	0.06	0.07	0.65	0.74

The measured density is equivalent to the nominal one. The porosity is significantly lower in the higher density specimens. Similarly, higher density material sintered at higher isothermal holding time shows relatively higher pore shape factor than low

density material (sintered at lower isothermal holding time). The fraction of load bearing section is determined using the values of porosity and the pore shape factor using eq. (17).

Figure 4.2.2 shows Sodium metabisulfite and 2% of Nital solution etched optical microstructures of sintered and sinterhardened materials.

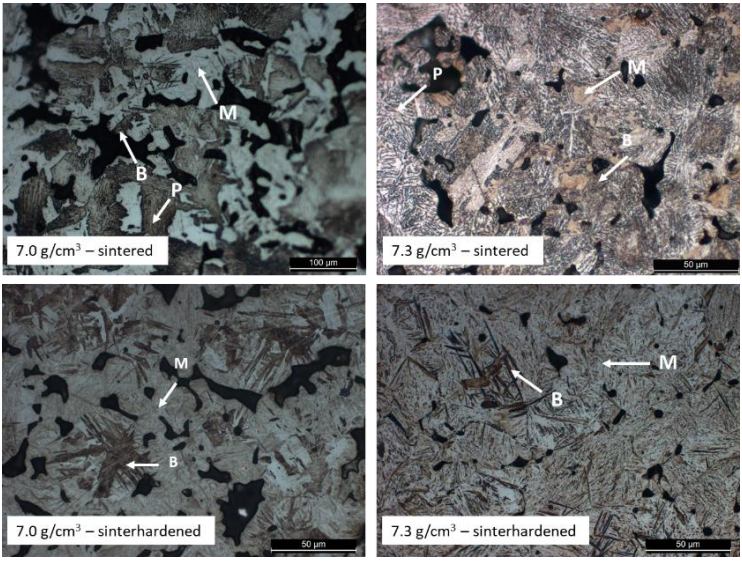

Figure 4.2.2 Etched optical microstructures of sintered and sinterhardened materials

The microstructure of the two sintered materials contains a mixture of pearlite (P), bainite (B) and Cu-rich martensite (M). 7.0 g/cm^3 sintered material comprises a higher heterogeneous mixture, while 7.3 g/cm^3 sintered material comprises the less heterogeneous mixture. This difference is due to the longer sintering time that enhances copper diffusion and homogenization in the ferrous matrix. Since copper affects the transformations of austenite on cooling, its improved homogeneity in austenite results in an improved homogeneity of the transformation products. After sinterhardening, 7.0 g/cm^3 material is again a heterogeneous microstructure and the mixture of lower bainite (B) and martensite (M) constituents. The mixture of bainitic and martensitic microstructural constituents surrounds both the bigger and smaller

pores. In the case of 7.3 g/cm^3 sinterhardening material, the matrix microstructure is a homogeneous mixture of bainite (B) and martensite (M). Therefore, the microstructural homogeneity of the higher density is gained by higher isothermal holding time, while the microstructural heterogeneity of low density material relates to the lower isothermal holding time.

Microhardness of the matrix was measured along the radial direction, from the surface to 1 mm depth with 0.1 mm interval. Figure 4.2.3 illustrates microhardness profiles of the weaker (selective indentation at the pearlite and bainite) constituent and mean (random indentation) of the 7.0 g/cm^3 and 7.3 g/cm^3 sintered and sinterhardened matrix.

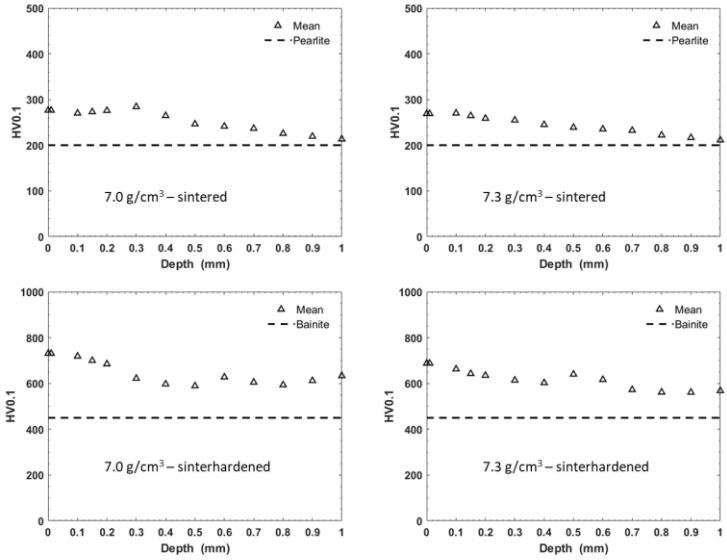

Figure 4.2.3 Microhardness profiles of weaker constituent and mean of sintered and sinterhardened materials

Due to the cooling rate differences between the surface and bulk, mean microhardness of all materials slightly decreases from the surface to the bulk. Their difference are related to the heat dissipation rate, and the surface layers are always expected to cool faster than the bulk. Faster cooling rate enhances the formation of

the martensitic microstructure at the surface. But, since the microstructure of the bulk cooled at a lower cooling rate, weaker constituent such as bainite are expected to form.

4.2.1. Theoretical prediction and experimental validation of subsurface crack nucleation

By comparing the equivalent Hertzian stress with the yield strength (σ_y) of the matrix, the theoretical resistance to contact fatigue crack nucleation was predicted. Figure 4.2.4 represents the theoretical prediction of contact fatigue cracks on sintered and sinterhardened materials of the two densities. Yield strength profiles of the matrix are reported using dotted lines, as calculated from the microhardness of weaker constituent and mean microhardness profiles. The maximum stress profiles are reported using the solid lines.

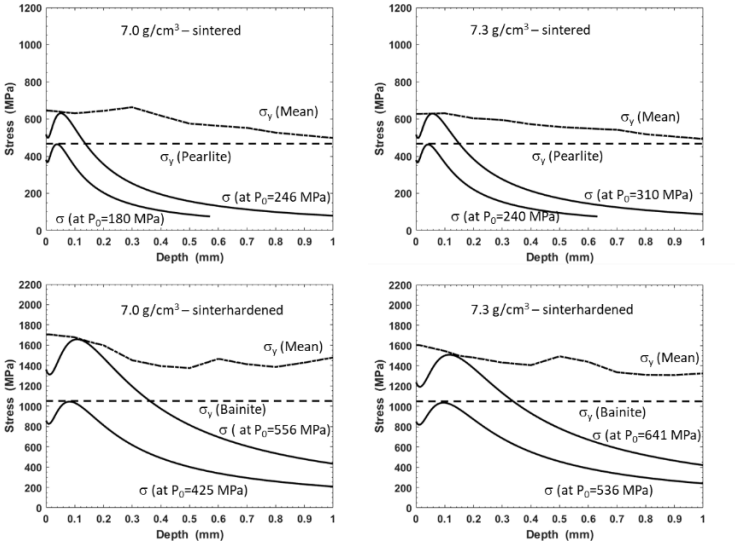

Figure 4.2.4 Theoretical prediction of contact fatigue cracks on 7.0 g/cm^3 and 7.3 g/cm^3 sintered and sinterhardened materials by comparing yield strength (σ_y) and maximum stress (σ)

The maximum stress corresponds to the mean Hertzian pressure values reported that are indicative of the theoretical resistance to the nucleation of the subsurface crack. The theoretical resistance to subsurface crack nucleation of all materials is summarized below:

- 7.0 g/cm^3 sintered material works without subsurface crack nucleation up to 246 MPa mean pressure if the mean yield strength of the matrix is the reference, but it works up to 180 MPa mean pressures if the yield strength of pearlite constituent is the reference.
- 7.3 g/cm^3 sintered material works without subsurface crack nucleation up to 310 MPa mean pressure if the mean yield strength is the reference, but it works up to 240 MPa mean pressure if the yield strength of pearlite constituent is the reference.
- 7.0 g/cm^3 sinterhardened material works without subsurface crack nucleation up to 556 MPa mean pressure if the mean yield strength of the matrix is the reference, but it works up to 425 MPa mean pressure if the yield strength of bainite constituent is the reference.
- 7.3 g/cm^3 sinterhardened material works without subsurface crack nucleation up to 641 MPa mean pressure if the mean yield strength of the matrix is the reference, but it works up to 536 MPa mean pressure if the yield strength of bainite constituent is the reference.

As additional information, the Hertzian depths were calculated at the corresponding mean pressures of Figure 4.2.4. Table 4.2.4 reports the Hertzian depth corresponds to the mean pressures that could support by sintered and sinterhardened materials. The Hertzian depth is used as the reference position to indicate the location of expected cracks.

Table 4.2.3 Hertzian depths at the corresponding mean pressures of Figure 4.2.4.

Material	Hertzian depth (µm)	
	Local approach (yield strength of the weaker constituents)	Mean approach (yield strength of the mean)
7.0 g/cm^3 – sintered	40	70
7.3 g/cm^3 – sintered	87	130
7.0 g/cm^3 – sinterhardened	42	73
7.3 g/cm^3 – sinterhardened	90	141

Contact fatigue test was carried out at different test mean pressures to validate the theoretical resistance. Then the occurrence of cracks were investigated on the microstructure of worn specimens. Figure 4.2.5 represents the microstructure of worn 7.0 g/cm^3 sintered materials, after the test at 189 MPa and 218 MPa mean pressures.

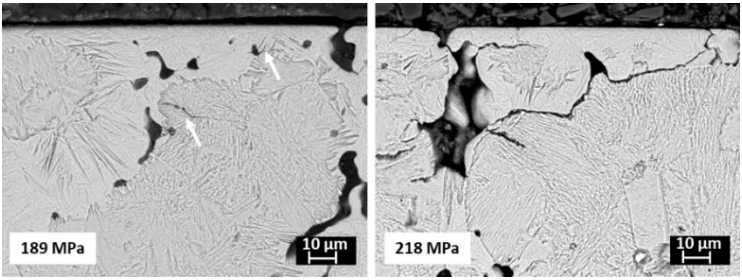

Figure 4.2.5 Microstructure of worn 7.0 g/cm^3 sintered specimen at different mean pressures

Within the Hertzian depth about 40 µm, subsurface cracks were observed at the two mean pressures. The two mean pressures are above the resistance determined with reference to pearlite and below the resistance determined with reference to the mean yield strength of the matrix. The observed results are in agreement with the theoretical prediction based on the local approach (based on the resistance of pearlite constituent that may resist up to 180 MPa pressure). Crack size and crack

number increase with pressure. The observed cracks first grow parallel to the surface then grow towards the surface, through pore connectivity, in the softer pearlite nodules or along the interface of weaker/harder constituent. At lower pressure, no contact fatigue cracks were observed in the microstructure. Therefore, the experimental evidence indicates that the local approach predicts the occurrence of subsurface crack formation very accurately than using the mean approach.

Figure 4.2.6 represents the microstructure of the worn 7.3 g/cm^3 sintered materials, after tests at 249 MPa and 374 MPa mean pressures.

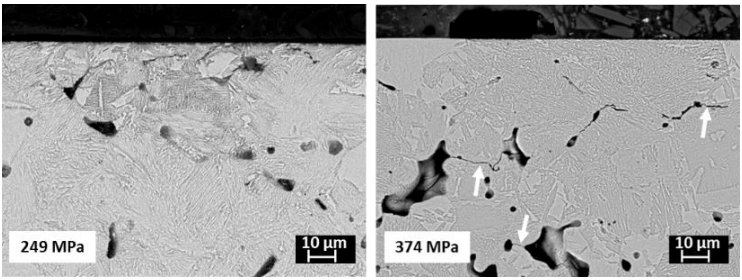

Figure 4.2.6 Microstructure of worn 7.3 g/cm^3 sintered specimen at different mean pressures

Contact fatigue cracks were not observed at 249 MPa. This applied mean pressure is higher than the theoretical resistance to contact fatigue cracks determined with reference to pearlite (local approach). But at a higher mean pressure, 374 MPa, which is higher than the theoretical resistance to contact fatigue cracks determined with reference to the mean yield strength of the matrix (mean approach), a few microcracks (indicated by white arrows in the figure) were observed. The nucleated cracks grow through the pore connectivity. These cracks appear within the Hertzian depth from the surface. The experimental result is in agreement with the theoretical prediction determined based on the mean approach.

The difference between using the local approach and mean approach for the 7.0 g/cm^3 and 7.3 g/cm^3 sintered materials are associated with the isothermal holding time. The former has heterogeneous microstructure (low isothermal holding time),

and cracks may nucleate at a mean pressure higher than the resistance of pearlite constituent. The latter has a more homogeneous microstructure (high isothermal holding time) and crack nucleation is less sensitive to the weak constituent due to its very low amount; it could nucleate only above the resistance of the mean yield strength of the matrix.

With a similar trend, the resistance to contact fatigue crack formation was investigated for sinterhardened steels. Figure 4.2.7 represents backscattered SEM microstructure of worn 7.0 g/cm^3 sinterhardened specimen tested at 404 MPa, and 529 MPa mean pressures.

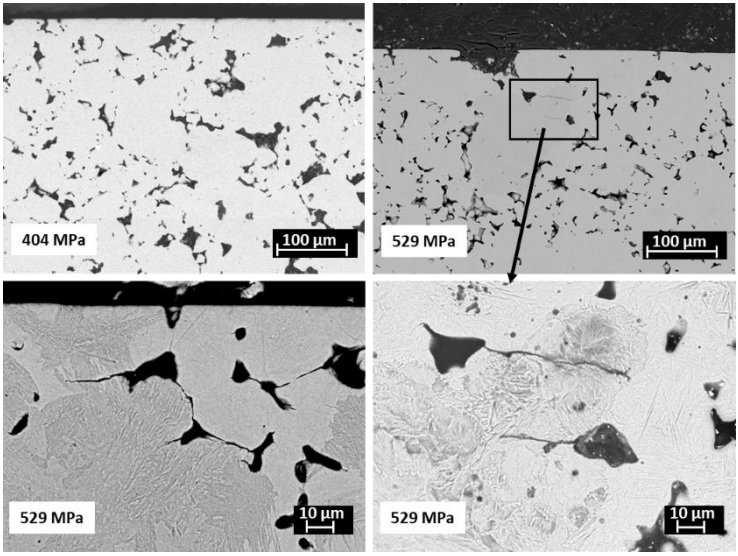

Figure 4.2.7 Unetched and etched microstructure of worn 7.0 g/cm^3 sinterhardened specimens at different mean pressures

Subsurface cracks were not observed at 404 MPa. This pressure is below the theoretical resistance determined with reference to the weaker bainite constituent (local approach). However, at 529 MPa, which is above the theoretical resistance of weaker constituent (local approach) but below the resistance determined with reference to the mean yield strength of the matrix (mean approach), subsurface

cracks were observed. Cracks are nucleated at the pore edge and grows either towards to the weaker/softer constituent (bainite) or along the bainite/martensite interface. The position of all detected cracks are within the Hertzian depth. The experimental results are in agreement with the theoretical resistance determined with reference to the bainite constituent.

Figure 4.2.8 represents unetched and etched microstructure of worn 7.3 g/cm^3 sinterhardened specimens tested at 575 MPa and 678 MPa mean pressures. The former and the latter pressures are above the theoretical resistance determined with reference to the weaker constituent and determined with reference to mean microhardness, respectively.

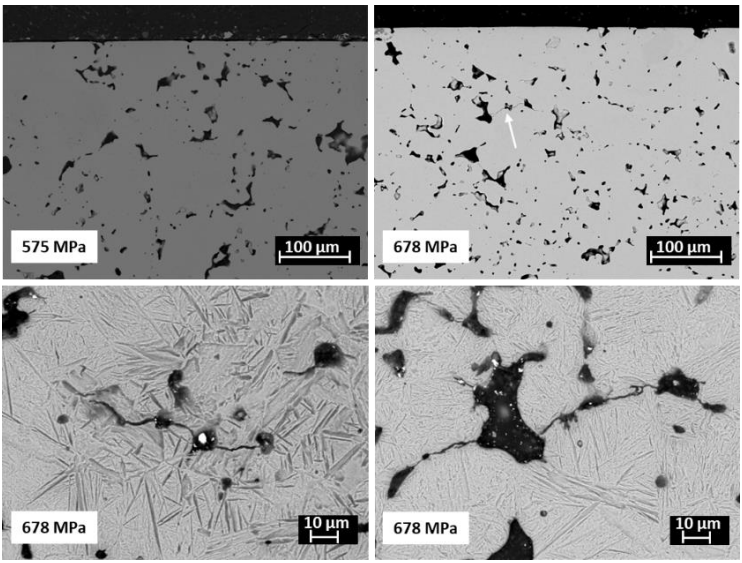

Figure 4.2.8 Microstructure of worn 7.3 g/cm^3 sinterhardened samples tested at different mean pressures

Subsurface cracks were not observed at 575 MPa mean pressures. This applied mean pressure is above the theoretical resistance of the bainite. But subsurface cracks were observed at 678 MPa, which is above the theoretical resistance

determined based on the mean approach. The etched microstructure with higher resolution shows the crack nucleation sites and growth paths. All cracks were nucleated at the pore edge and grew along the pore connectivity.

Even after sinterhardening, the microstructural homogeneity still influences the type of approaches used to determine the theoretical resistance of the material: the local approach for low density material and the mean approach for high density material.

4.2.2. Theoretical prediction and experimental results of surface plastic deformation

Figure 4.2.9 represents the top surface view of sintered materials before the contact fatigue test. This top surface view is also representative of the sinterhardened materials of the equivalent densities. The figure shows open pore population with a size decreasing with density.

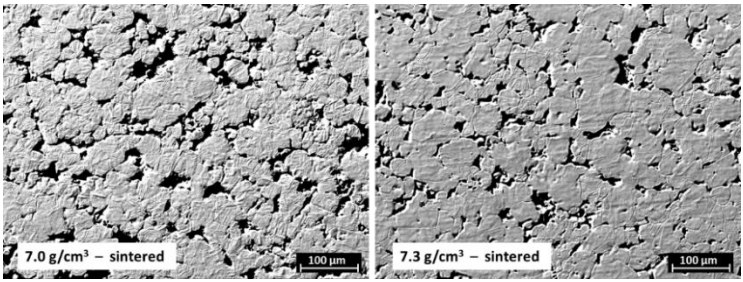

Figure 4.2.9 Top surface view of 7.0 g/cm^3 and 7.3 g/cm^3 sintered materials

Pore size distribution was analyzed using image analysis. Figure 4.2.10 represents the pore size distribution. The bigger pore size decreases as the compact density increases.

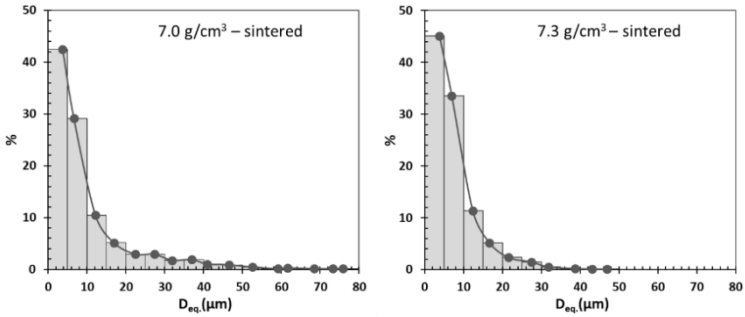

Figure 4.2.10 Equivalent diameter of surface pore distribution measured by image analysis

Before sectioning the ring, load bearing surface Mr2 and the surface microhardness were measured using surface profilometer and microhardness tester, respectively. Table 4.2.4 reports the nominal density, load bearing surface and microhardness of the sintered and sinterhardened material.

Table 4.2.4 Surface hardness and load bearing surface of sintered and sinterhardened materials

Material	Mr_2	HV0.1		
		weaker	mean	harder
7.0 g/cm³ – sintered	79	214	276	-
7.3 g/cm³ – sintered	83	210	269	-
7.0 g/cm³ – sinterhardened	79	450	674	804
7.3 g/cm³ – sinterhardened	83	453	709	804

Microhardness of the weaker and harder constituent measured by selective indentation and surface microhardness is by random indentation. The microstructure of the surface comprises a mixture of weaker and harder constituents. The weaker constituent of the sintered material is pearlite, while the weaker constituent of sinterhardened material is bainite.

Since sintered and sinterhardened material contains the softer constituents such as pearlite and bainite microstructure in the matrix, brittle surface cracks are not expected to nucleate. Instead, the occurrence of surface plastic deformation was investigated with reference to the weaker constituent and the mean microhardness.

Surface plastic deformation was predicted theoretically simply by comparing surface stress with the yield strength of the surface layer. Figure 4.2.11 represents the theoretical prediction of surface plastic deformation at a test pressure of sintered and sinterhardened materials.

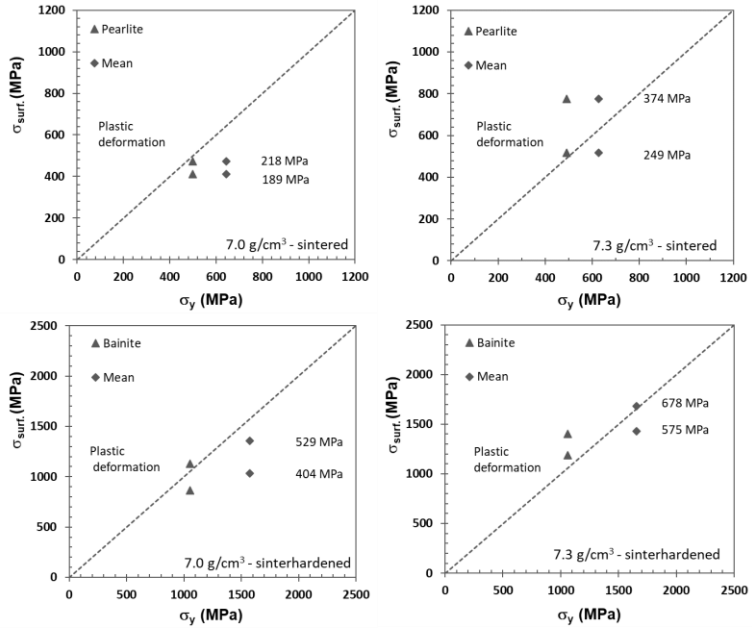

Figure 4.2.11 Theoretical prediction of surface plastic deformation of sintered and sinterhardened materials

The theoretical calculation of surface plastic deformation done at all test pressures (that were used to verify the formation of subsurface cracks). The calculation is carried out based on the local and the mean approaches, and the results are reported in the diagrams. The bisector line separates the material resistance regime

to the surface plastic deformation regime; if the data points lie on the right side of the line, the material is not expected to undergo plastic deformation, while data points on the left side indicate the occurrence of surface plastic deformation. The results of theoretical prediction are summarized as:

- 7.0 g/cm^3 sintered materials: no surface plastic deformation at all test pressures;
- 7.3 g/cm^3 sintered material: surface plastic deformation at all test pressures based on the local approach, no plastic deformation at a lower pressure based on the mean approach;
- 7.0 g/cm^3 sinterhardened material: surface plastic deformation at the higher pressure based on the local approach;
- 7.3 g/cm^3 sinterhardened material: no plastic deformation at a lower test pressure based on the mean approach.

Then, the occurrence of surface plastic deformation investigated experimentally. Figure 4.2.12 illustrates a top surface view of sintered worn samples tested at different mean pressure.

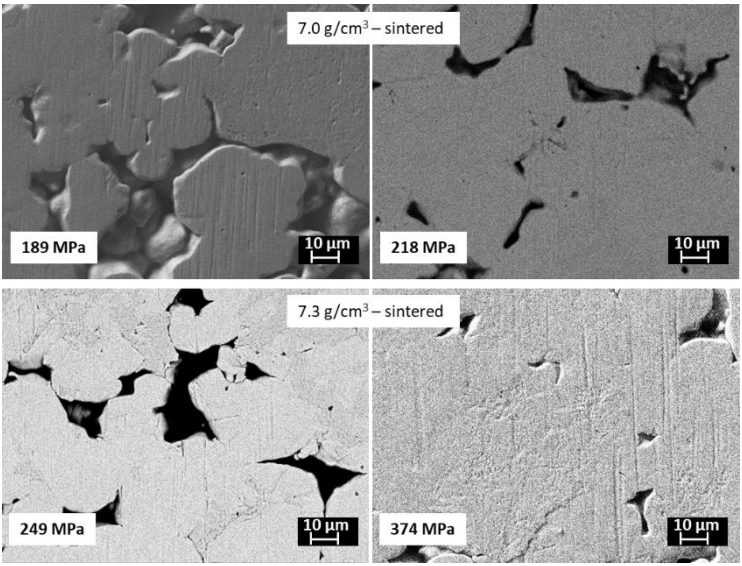

Figure 4.2.12 Top view of worn sintered specimens tested at different mean pressures

Neither surface cracks nor surface densification due to plastic deformation were not observed at 189 MPa and 218 MPa on 7.0 g/cm^3 sintered materials. The experimental evidence is in agreement with the theoretical prediction; with both the local approach and the mean approach that predict no plastic deformation. In the case of 7.3 g/cm^3 sintered material, surface cracks, and densification were not observed at 249 MPa mean pressure; this is in agreement with the theoretical prediction based on the mean approach. However, at 374 MPa mean pressure the surface is densified; this is coherent with the theoretical predictions made with the two approaches.

With similar trend, the surface view of worn sinterhardened material was characterized. Figure 4.2.13 illustrates the top surface view of sinterhardened materials tested at different mean pressures.

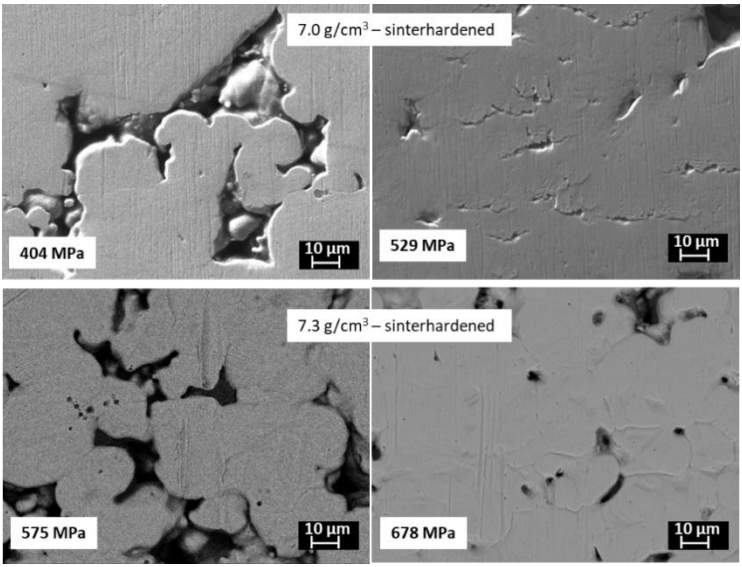

Figure 4.2.13 Top view of worn sinterhardened specimens tested at different mean pressures

7.0 g/cm^3 sinterhardened material does not show surface plastic deformation at 404 MPa. However, at high pressure of 529 MPa, surface densification by plastic deformation was observed. The experimental evidence is in agreement with the theoretical prediction based on the local approach. In the case of 7.3 g/cm^3 sinterhardened material, surface densification was observed at 575 MPa test pressure. Again, this is in agreement with the theoretical prediction based on the mean approach. At 678 MPa surface densification by plastic deformation was observed. The mean approach predicts plastic deformation at this pressure.

To summarize, the occurrence of subsurface cracks and surface plastic deformation were determined for each density of sintered and sinterhardened conditions. Figure 4.2.14 shows the effect of density and sinterhardening on the resistance to contact fatigue crack nucleation of materials.

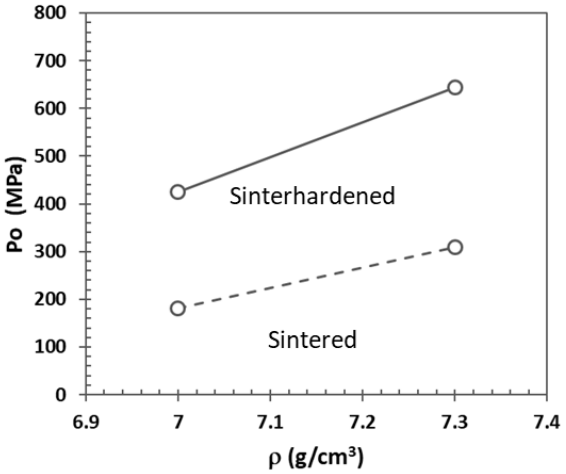

Figure 4.2.14 Effect of density and sinterhardening on the resistance to subsurface crack nucleation

The resistance to subsurface cracks nucleation increases linearly with the density. The increase in density from 7.0 g/cm^3 to 7.3 g/cm^3 improves crack nucleation resistance by 34% to 42%. Also, applying sinterhardning treatment increases the resistance by 52% to 58%.

The theoretical resistance for surface plastic deformation was calculated using the mean coefficient of friction that was measured during the test, which is 0.13 for 7.0 g/cm^3 and 0.09 for 7.3 g/cm^3 materials. Figure 4.2.15 represents the effect of density and sinterhardening on the theoretical resistance of surface plastic deformation of materials.

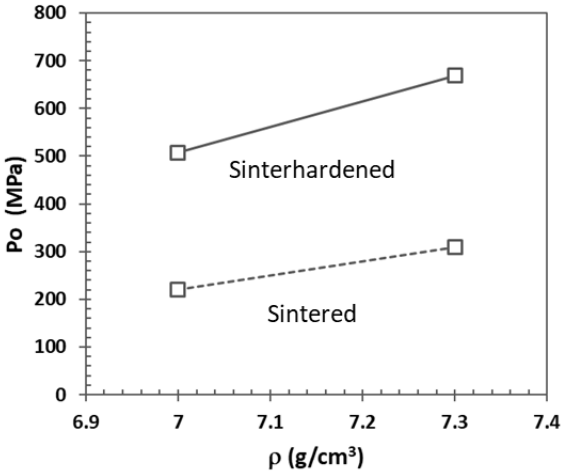

Figure 4.2.15 Effect of density and sinterhardening on the resistance to surface plastic deformation

The theoretical resistance to surface plastic deformation increases linearly with the density. The increase of density from 7.0 g/cm^3 to 7. 3 g/cm^3 improves surface plastic deformation resistance by 24% to 29%. An additional treatment of sinterhardning increase the resistance to contact fatigue, improving by 54 % to 57%.

4.3. Low-Ni diffusion bonded steels: effect of sintering temperature

In this part, the influence of sintering temperature on Ancorsteel and EcosintC75 materials in lubricated rolling-sliding contact was investigated. Ancorsteel and EcosintC75 powders are diffusion bonded and sinter at conventional and high sintering temperatures. Cr and Mn alloying elements were added to the two materials. This addition can improve the performance related to the mechanical properties and reduces the overall production cost [80].

However, these alloying elements are oxygen sensitive and form stable oxides that may affect the quality of the interparticle bonding. Sintering atmosphere and sintering

temperature are set up, aiming to reduce particle surface oxide layers and to provide homogenized microstructures. Therefore, the effect of sintering temperature on the resistance to contact fatigue and surface crack nucleation was studied using the theoretical approach and validated experimentally.

Edogas and H_2/N_2 are the sintering atmospheres used for the two materials sintered at 1150 °C and 1250 °C, respectively.

AS1150 and AS1250 are codes used to represent Ancorsteel material sintered at 1150 °C and 1250 °C, respectively. Ecosint1150 and Ecosint1250 are codes used to represent EcosintC75 material sintered at 1150 °C and 1250 °C, respectively.

Figure 4.3.1 represents unetched scanning electron microstructure of Ancorsteel and EcosintC75 materials.

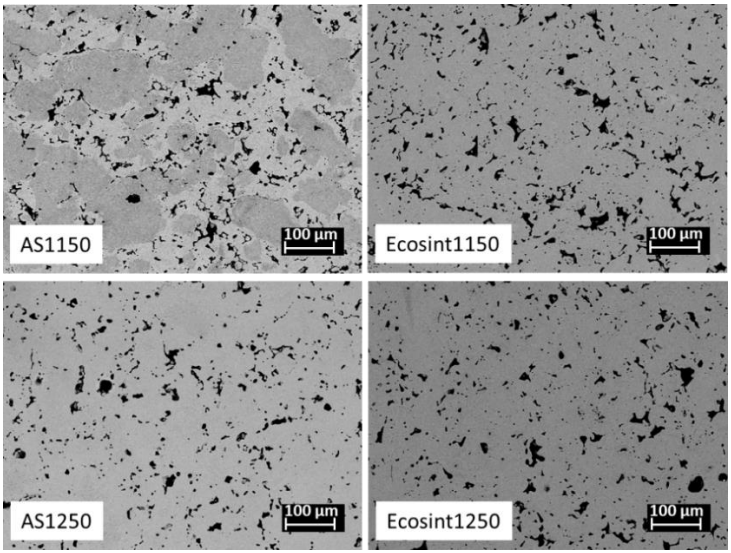

Figure 4.3.1 Scanning electron microstructure of Ancorsteel and EcosintC75 materials

Pore parameters were measured using image analysis. Table 4.3.1 reports the density, subsurface pore parameters and elastic modulus of the two materials sintered at conventional and high sintering temperatures.

Table 4.3.1 Density, pore parameters and elastic modulus

Material	ρ (g/cm3)	ε	f_{circle}	Φ	E, GPa
AS1150	6.83	0.11	0.58	0.56	120
Ecosint1150	7.01	0.09	0.59	0.61	137
AS1250	7.04	0.08	0.66	0.72	155
Ecosint1250	7.15	0.08	0.63	0.71	158

As expected, sintering at 1250 °C provides a higher pore shape factor (f_{circle}), a fraction of load bearing sections and elastic modulus than sintering at 1150 °C. Sintering temperature also influences the number of surface pores. By eliminating the smaller pore with equivalent diameter < 2.35 μm, the total number of pore was counted on the image of each material and sintering conditions. The number of pores counted for AS1150 and AS1250 was 289 and 248, respectively. The number of pores counted for Ecosint1150 and Ecosint1250 was 579 and 551, respectively. In both materials, the number of pore decreases with increasing sintering temperature

The equivalent diameter and maximum Feret diameter of pores were compared to show the effect of the sintering temperature on the two materials. The pore sizes distribution of the two materials is represented using Figure 4.3.2.

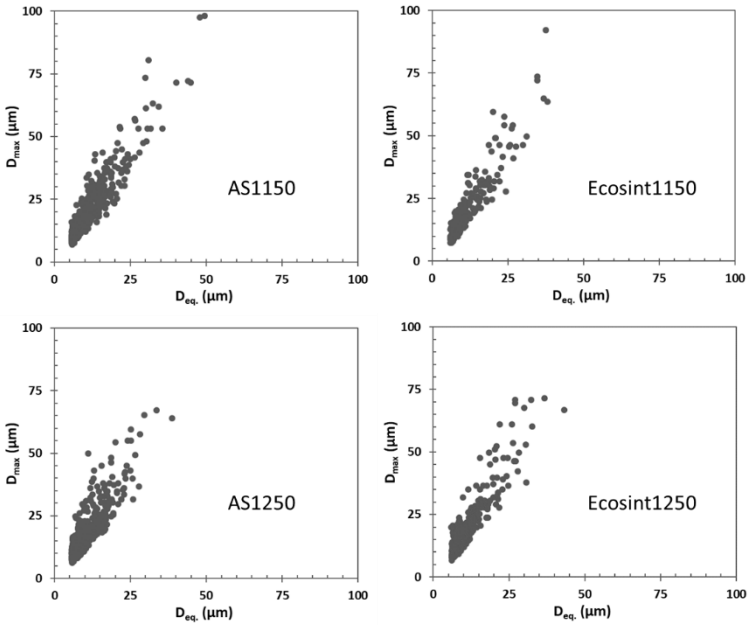

Figure 4.3.2 Pore size distribution of Ancorsteel and EcosintC75 materials sintered at 1150 °C and 1250 °C

As expected, higher sintering temperature does not affect pore size significantly.

Figure 4.3.3 represents etched microstructure of Ancorsteel and EcosintC75 materials analyzed using an optical microscope.

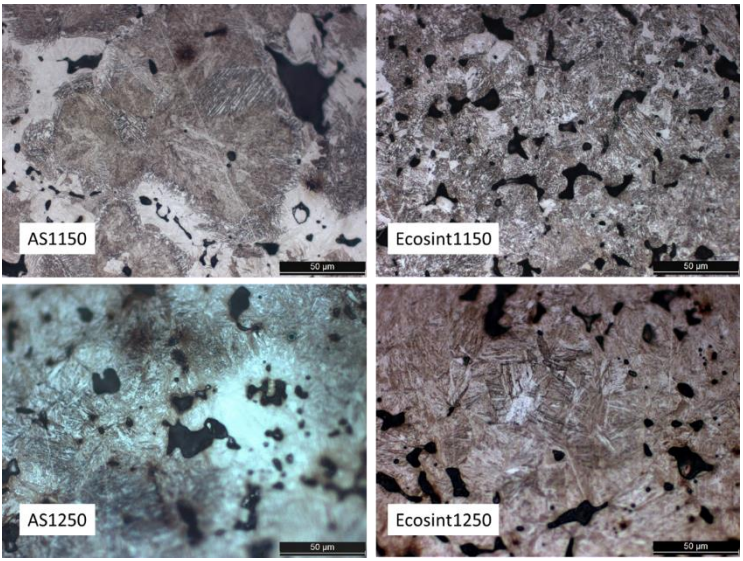

Figure 4.3.3. The etched optical microstructure of the Ancorsteel and EcosintC75 materials sintered at conventional and high sintering temperatures

The microstructure of AS1150 contains whiter region (martensite) and the brown region (bainite), and the microstructure of Ecosint1150 is bainitic, a mix of upper and lower bainite. The microstructure of the two materials sintered at high temperature is still the mixture of the two constituents. AS1250 comprises bainite and martensite, better homogenized than at low temperature. Similarly, the microstructure of Ecosint1250 is an improved mixture of bainite and martensite.

Figure 4.3.4 represents the microhardness profiles of bainite and the mean one of Ancorsteel and EcosintC75 sinterhardened materials.

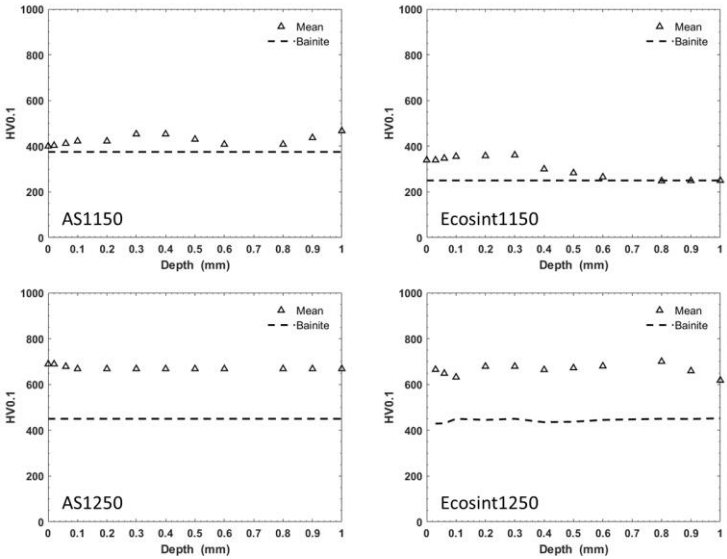

Figure 4.3.4 Microhardness profiles of Ancorsteel and EcosintC75 materials sintered at conventional and high temperatures

The microhardness of the two materials increases with sintering temperature and is constant within the Hertzian depth in all the cases. The increase of microhardness of the two materials sintered at high temperature related to the removal of oxide surface that facilitates better inter diffusion of alloying elements.

4.3.1. Theoretical prediction and experimental validation of subsurface crack nucleation

Figure 4.3.5 represents the theoretical prediction of subsurface cracks for Ancorsteel and EcosintC75 sinterhardened materials. Yield strength profile (represented by the dote lines) of the matrix was calculated from the mean microhardness profiles and that of the weaker constituents. The reported mean Hertzian pressure values are corresponding to the theoretical resistance to the nucleation of the subsurface cracks on the two materials sintered at low and high temptresses.

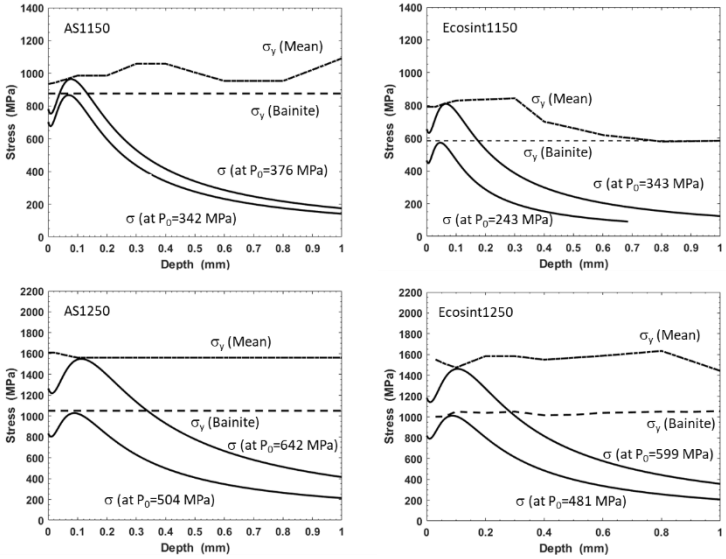

Figure 4.3.5 Theoretical prediction of the materials using the mean and weaker microhardness

The theoretical resistance to the subsurface crack nucleation was predicted based on the local approach (with reference to the theoretical resistance of weaker constituent) and the mean approach (with reference to the mean microhardness), and the results are summarized as follows:

- AS1150 material is expected to survive at 376 MPa, and 342 MPa mean pressures with reference to the mean and local approaches, respectively;
- Ecosint1150 material is expected to survive at 343 MPa (mean approach), and 243 MPa (local approach) mean pressure;
- AS1250 material can resist subsurface crack nucleation at 642 MPa (mean approach) and 504 MPa (local approach) mean pressures;
- Ecosint1250 material can resist subsurface crack nucleation at 599 MPa (mean approach), and 481 MPa (local approach) mean pressures.

The theoretical resistance to the contact fatigue crack nucleation of high temperature sintered materials is higher than that of low temperature sintered material.

Hertzian depths were calculated for the above reported mean pressures. Table 4.3.2 reports the Hertzian depth that were determined with reference to local and mean approaches.

Table 4.3.2 Hertzian depth referring to bainite and mean microhardness

Materials	**Hertzian depth (μm)**	
	Local approach	**Mean approach**
AS1150	70	77
Ecosint1150	46	66
AS1250	91	114
Ecosint1250	84	105

The Hertzian depth is the higher in all the case for materials sintered at high temperature.

Figure 4.3.6 represents the microstructure of worn AS1150 samples tested at different mean pressures.

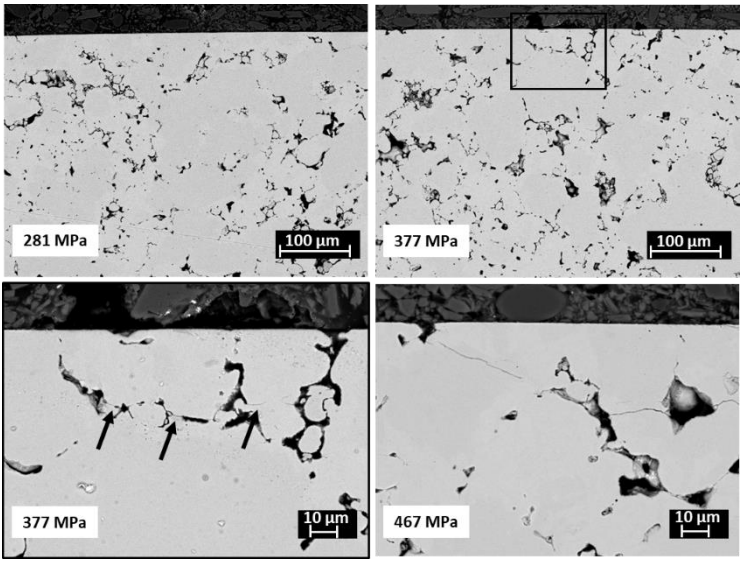

Figure 4.3.6 Microstructure of worn AS1150 spacemen tested at different mean pressures

No subsurface cracks were observed at 281 MPa. The pressure is below the theoretical resistance of weaker (bainite) constituent. At 377 MPa (equivalent with the theoretical resistance of the weaker constituent), very few microcracks were observed within the Hertzian depth. At higher pressure, 467 MPa (above the theoretical resistance determined with the mean microhardness), longer subsurface cracks nucleated within the Hertzian depth and grows towards the surface. Therefore, the experimental evidence indicates that the local approach predicts the nucleation of subsurface cracks.

Figure 4.3.7 represents the microstructure of worn Ecosint1150 samples tested at different mean pressures.

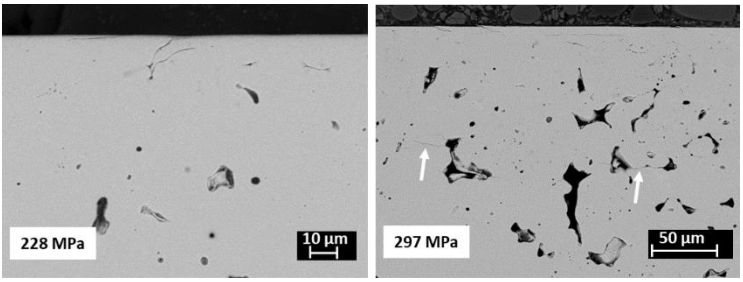

Figure 4.3.7 Etched microstructure of worn Ecosint1150 spacemen tested at different mean pressures

At 228 MPa pressure, which is below the theoretical resistance of the weaker (bainite) constituent, no subsurface cracks were observed. However, at higher pressure 279 MPa, which is above the theoretical resistance of the bainite constituent, contact fatigue cracks were observed at the Hertzian depth. Therefore, the occurrence of subsurface cracks is predicted accurately using the local approach.

With a similar trend, the theoretical resistance to contact fatigue cracks of high temperature sintered materials was validated. Figure 4.3.8 represents the microstructure of worn AS1250 sample tested at 485 MPa, and 556 MPa mean pressures.

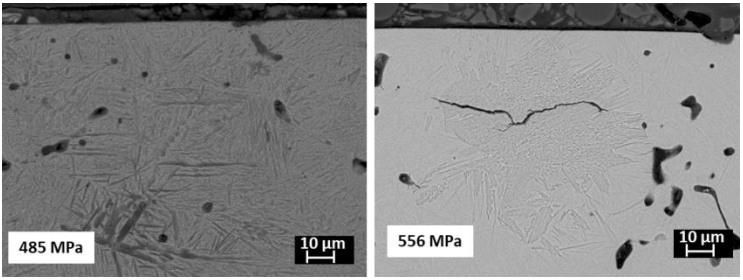

Figure 4.3.8 Microstructure of worn AS1250 samples tested at different mean pressures

No subsurface cracks were observed at 485 MPa; since the mean pressure is below the theoretical resistance of the weaker constituent. But at 556 MPa, which is above the resistance of the weaker constituent and below the resistance of the mean microhardness, subsurface cracks were observed. These cracks found in the bainitic microstructure that agrees with the theoretical resistance of the bainitic constituent (local approach).

Figure 4.3.9 represents the microstructure of worn Ecosint1250 sinterhardened specimen at two different test pressures.

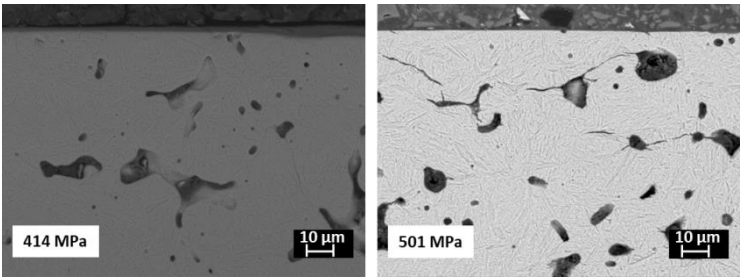

Figure 4.3.9 Microstructure of worn Ecosint1250 specimen tested at different mean pressures

Subsurface cracks were not observed at 414 MPa (which is below the theoretical resistance of the bainite constituent). However, at higher test pressure, 501 MPa, which is above the resistance of bainite and below the mean yield strength, cracks were observed. These cracks are nucleated at the pore edges and grew towards the surface along the pore connectivity.

Similar to materials sintered at a lower temperature, the experimental results of materials sintered at higher temperature are in agreement with the theoretical resistances with reference to the local approach. Moreover, sintering at high temperature improves the resistance to the formation of contact fatigue cracks, this relates to the improvement of a fraction of load bearing sections and yield strength of the matrix.

4.3.2. Theoretical prediction and experimental results of surface plastic deformation

Since Ancorsteel and EcosintC75 materials contain bainite, brittle surface cracks are not expected in this material and not investigated. However, the occurrence of surface plastic deformation of the materials was investigated theoretically and validated experimentally.

Similar to the study of subsurface cracks, pore parameter and microhardness of the surface were analyzed first. Figure 4.3.10 represents the top surface (with a magnification of 250x) of the two materials sintered at the conventional and high sintering temperatures.

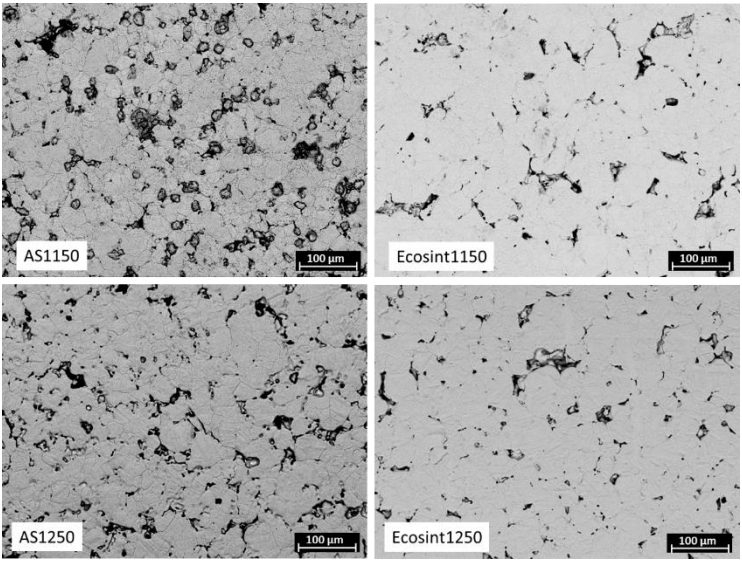

Figure 4.3.10 Top surface view of Ancorsteel and EcosintC75 materials sintered at 1150 °C and 1250 °C

Pore size and distributions were measured using image analysis. The effect of high sintering temperature was observed on both materials where surface pores are

relatively smaller in size and rounded in shape. Figure 4.3.11 represents the distribution of maximum Feret diameter of the surface pore of the two materials.

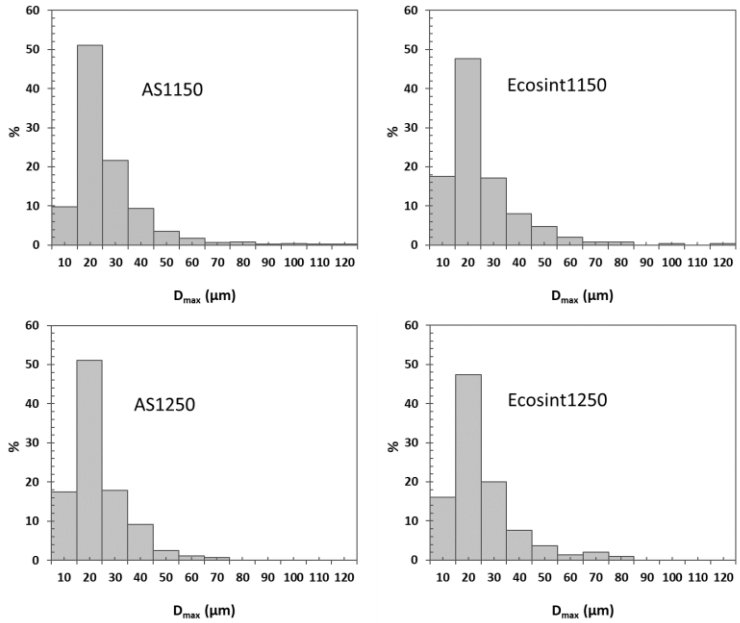

Figure 4.3.11 Distribution of maximum pore diameters of Ancorsteel and EcosintC75 materials sintered at 1150 °C and 1250 °C

The maximum pore diameter for AS1150 and Ecosint1150 sintered at a lower temperature is about 120 µm. Sintering at higher temperature decreases the pore diameter to 75 µm and 85 µm in AS1250 and Ecosint1250, respectively. This reduction indicates that higher sintering temperature may be beneficial to decreases the surface pore size that may result in a significant effect on the resistance to surface plastic deformation.

Table 4.3.3 reports the summary of surface characteristics (microhardness, load bearing surface, and elastic modulus) of the two materials.

Table 4.3.3 Surface characteristics of Ancorsteel and EcosintC75 materials

Material	HV10	HV0.1			Mr_2 (%)	E (GPa)
		Bainite	Martensite	Mean		
AS1150	305-352	375	762	400	86.2	195
Ecosint1150	203-261	250	-	339	77.3	185
AS1250	399-590	450	784	689	83.9	192
Ecosint1250	422-553	429	813	609	78.7	186

Since the microstructure comprises the softer constituents, the response of the contact surface may undergo either elastic or plastic deformation, and the plastic deformation is predicted theoretically and validated by observing the surface top views and the microstructures.

The theoretical prediction of surface plastic deformation, the top surface view, and microstructure of worn AS1150 specimen tested at different pressure are presented using Figure 4.3.12.

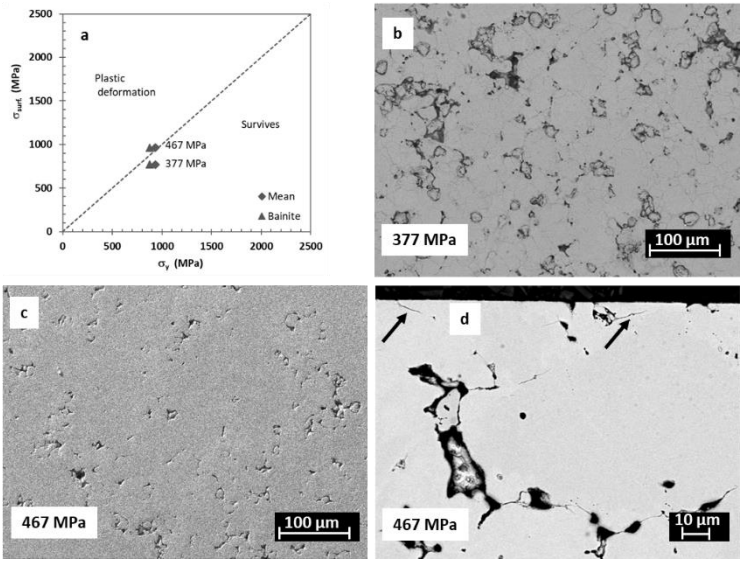

Figure 4.3.12 Theoretical prediction of surface plastic deformation (a), top surface views (b and c) and microstructure (d) of worn AS1150 specimen tested at different mean pressures

Diagram (a) presents the theoretical resistance of the AS1150 material with reference to weaker/bainite constituent (local approach) and the mean microhardness (mean approach). According to the local and the mean approaches, the model predicts no surface plastic deformation at 377 MPa. At higher pressure, 467 MP, the surface stress is higher than the yield strength of the bainite constituent as well as of the mean one, and the occurrence of surface plastic deformation is predicted. The theoretical predictions are validated using the top surface view and the microstructure of worn surfaces. Accordingly, figure (b) shows no surface plastic deformation at the lower mean pressure, and figure (c) and (d) also validates the occurrence of surface plastic deformation (that results in densification, surface cracks/shear lips), respectively.

Figure 4.3.13 represents the theoretical prediction, the surface top views, and the microstructure of the worn Ecosint1150 test at different mean pressures.

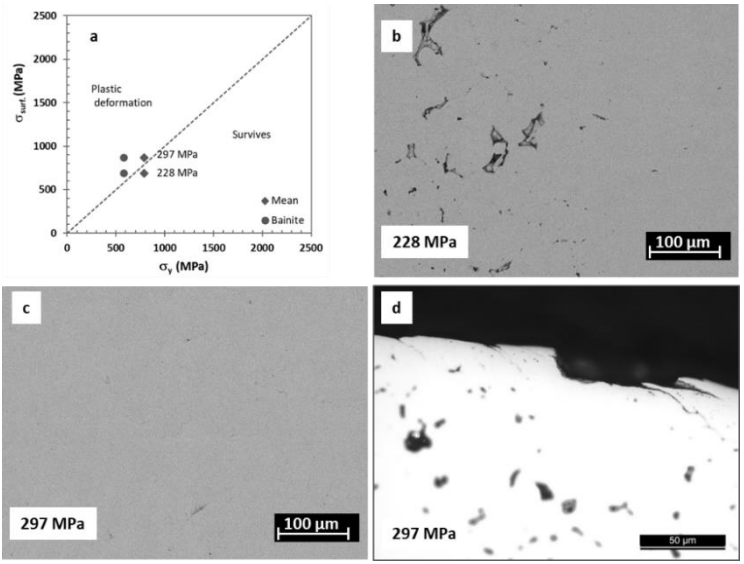

Figure 4.3.13 Theoretical prediction of surface plastic deformation (a), surface top views (b and c) and microstructure (d) of worn Ecosint1150 spacemen tested at different mean pressures

The theoretical prediction is presented using figure (a). Surface plastic deformation is expected at 228 MPa and 297 MPa with reference to the local approach and 297 MPa with reference to the mean approach; since the surface stress is higher than the yield strength of bainite. This prediction is validated using the experimental observation of top surface view (b, c) that shows surface densification at both pressures. The microstructure of worn specimen (d) also indicates the presence of surface cracks and pitting at a higher pressure. Theoretical resistance of the surfaces sintered at low temperature may be predicted accurately using the local approach.

With a similar trend, the theoretical resistance and experimental evidence of surface plastic deformation of materials sintered at high temperature were studied. Figure 4.3.14 represents the theoretical prediction, the top surface view, and the microstructure of worn AS1250 specimen tested at different pressures.

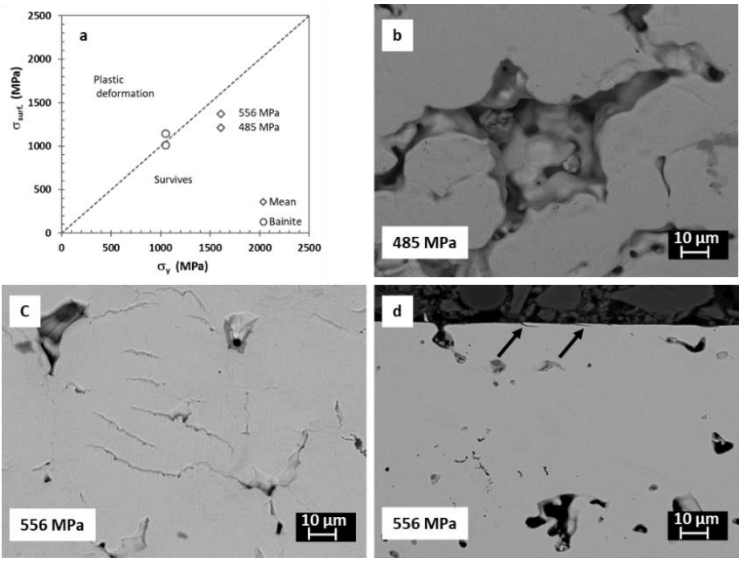

Figure 4.3.14 Theoretical prediction of surface plastic deformation (a), top surface views (b and c) and microstructure (d) of worn AS1250 specimen tested at different mean pressures

Theoretical prediction of the surface plastic deformation is presented using figure (a). According to eq. (20), surface stress is a function of applied mean pressure, notch sensitivity, friction and load bearing surface. But at the given surface porosity, roughness and applied mean pressure, the surface stress is higher on the matrix that are characterized as the mean (martensitic matrix) than on the bainitic matrix because both matrix have different notch sensitivity values: 0.7 for mean matrix (more martensitic constituent) and 0.5 for bainitic matrix. Surface plastic deformation is not predicted at 485 MPa and all test pressures with reference to the local approach and the mean approach respectively. The theoretical predictions are validated using the experimental results: figure (b) shows no surface plastic deformation at a lower pressure, and figure (c) and (d) shows densification, surface cracks, and shear lips.

Figure 4.3.15 represents the theoretical prediction and top surface view of Ecosint1250 materials tested at different mean pressures.

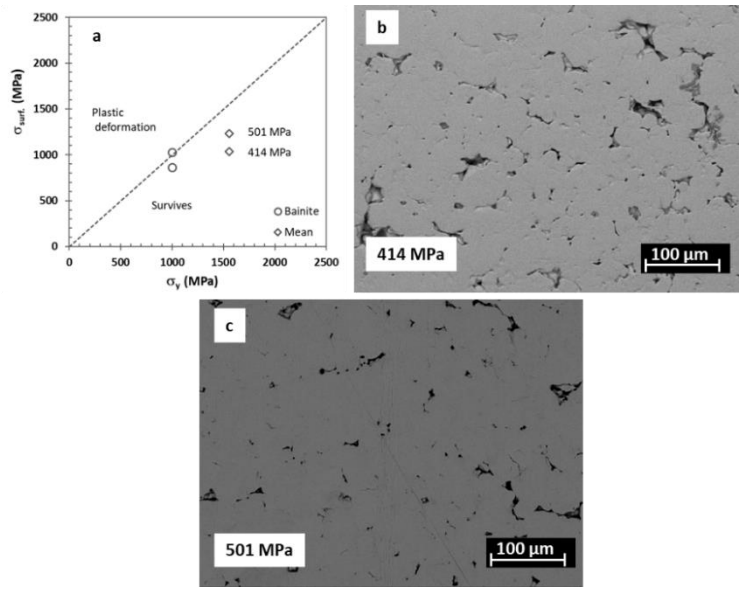

Figure 4.3.15 Theoretical prediction of surface plastic deformation (a), surface top views (b, c) of worn Ecosint1250 spacemen tested at different mean pressures

The theoretical prediction is presented using figure (a). At the given surface porosity, roughness and applied mean pressure, the surface stress is higher on the matrix that are characterized as the mean (martensitic matrix) than on the bainitic matrix because both matrix have different notch sensitivity values: 0.7 for mean matrix (more martensitic constituent) and 0.5 for bainitic matrix. The model predicts no surface plastic deformation at 414 MPa with reference to the resistance of bainitic matrix (local approach) and at all pressures with reference to the resistance of the martensitic matrix (mean approach). The prediction is also validated using the experimental results: the top surface view (b) shows no surface densification and cracks at a lower pressure and slight densification at the higher pressure.

Similar to the materials sintered at a low temperature, the theoretical resistance of the surfaces sintered at a high temperature may be predicted accurately using the local approach. The similarity relates to the microstructural heterogeneity, and both low and high sintering temperature material comprise the weaker constituent, such as bainite. In all the cases high sintering temperature increases the resistance to surface plastic deformation because of the reduction of surface pore size, improvement of matrix yield strength and load bearing surface.

4.4. High-Ni diffusion bonded steels: carburizing vs. through hardening

Apart from the porosity, the second most important parameters are microstructure and microstructural heterogeneity. Harder and homogeneous microstructures provide better resistance to contact fatigue and wear damage. However, heterogeneous microstructures provide a mix of weaker and harder constituents that may affect the resistance to contact fatigue and wear damage, due to the local variation in the matrix yield strength. To modify the microstructure, carburizing (effective on the surface) and heat treatment (effective on the entire cross section) are common techniques applied on PM structural parts that transform the material into a martensitic microstructure. These techniques increase the matrix yield strength and therefore improves the resistance to plastic deformation.

The influence of density, carburizing and heat treatment on the crack formation during lubricated rolling-sliding contact was studied in [81,82,60,83]. As already highlighted, a higher resistance can be gained by reducing porosity and providing a martensitic microstructure. However, the presence of a weaker constituent in a heterogeneous microstructure may affect the resistance to crack nucleation and is not well studied yet.

Ni is added to improve the powder compressibility and matrix toughness; however, the final microstructure comprises harder martensite and weaker Ni-rich austenite. This type of microstructural combination may influence the resistance to crack nucleation. Therefore, the application of surface carburizing and heat treatment may

not show a significant effect on the elimination of local weaker/softer regions. This weaker constituent may decrease the resistance to contact fatigue and wear damage of the typical heterogeneous microstructure.

The contact fatigue and wear damage of Fe-0.5%Mo-4%Ni-1.5%Cu-0.5%C sinterhardened PM steel were studied in [33]. The paper is analyzed only the formation of subsurface cracks using theoretical prediction and experimental validation. However, the effect of densifying, carburizing and heat treatment on the formation of subsurface and surface crack formation has not yet studied.

This study investigates the effect of density and different treatments on the contact fatigue crack nucleation of Fe-0.5%Mo-4%Ni-1.5%Cu PM steel. Carbon added in the form of graphite, 0.3% for the carburized, and 0.5% C for the heat treated conditions. Ring specimens were produced with target densities of 7.0 g/cm^3 and 7.3 g/cm^3. Subsurface and surface crack nucleation during lubricated rolling-sliding contact were studied using the theoretical models described in eq. (14) and eq. (20) and validated experimentally using the contact fatigue tests.

4.4.1. Theoretical prediction and experimental validation of subsurface crack nucleation

Figure 4.4.1 shows the microstructure of carburized (DAE1) and through hardened (DAE2) materials at the optical microscope.

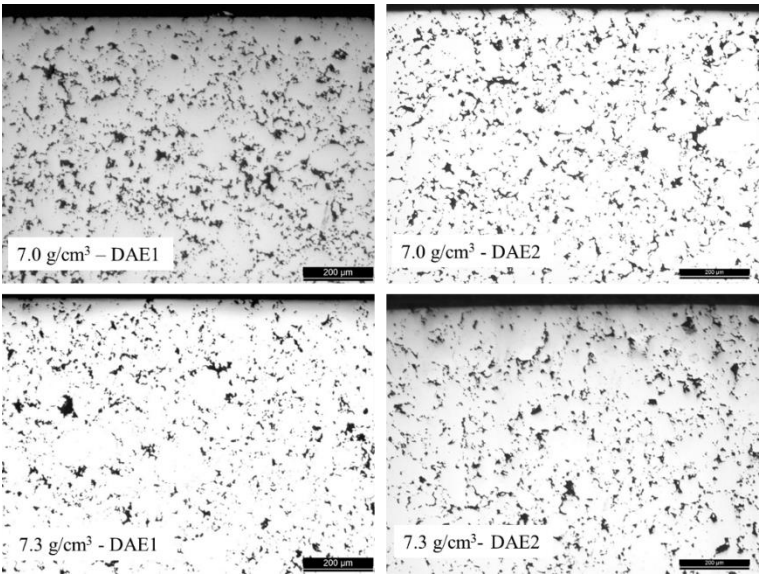

Figure 4.4.1 Unetched microstructure of carburized and through hardened materials with different densities

Porosity, pore area, and perimeter were measured on unetched microstructure using image analysis, from which density, pore shape factor, elastic modulus and a fraction of load bearing sections were determined. Table 4.4.1 reports the pore parameters and selected properties of the two DAE materials.

Table 4.4.1 Pore parameter and material properties of carburized and through hardened diffusion boned materials

Material	ρ, g/cm³		ε	f_{circle}	Φ	E, GPa
	Nominal	Measured				
DAE1	7.0	7.04	0.11	0.58	0.57	118
DAE2	7.0	7.03	0.11	0.60	0.58	123
DAE1	7.3	7.25	0.08	0.66	0.73	154
DAE2	7.3	7.30	0.07	0.62	0.74	160

The measured density corresponds to the nominal one. As expected, the porosity of the two materials decreases with increasing density. As a correction factor, the fraction of load bearing surface was calculated in terms of porosity and pore shape factor using eq. (16). Determination of pore shape factor (f_{circle}) of a fraction of load bearing sections and elastic modulus is based on the mean values of the whole pore population, which was measured on the three different adjacent microstructures. All pore parameters and elastic modulus increase with density.

Figure 4.4.2 represents etched microstructure of carburized and through hardened materials.

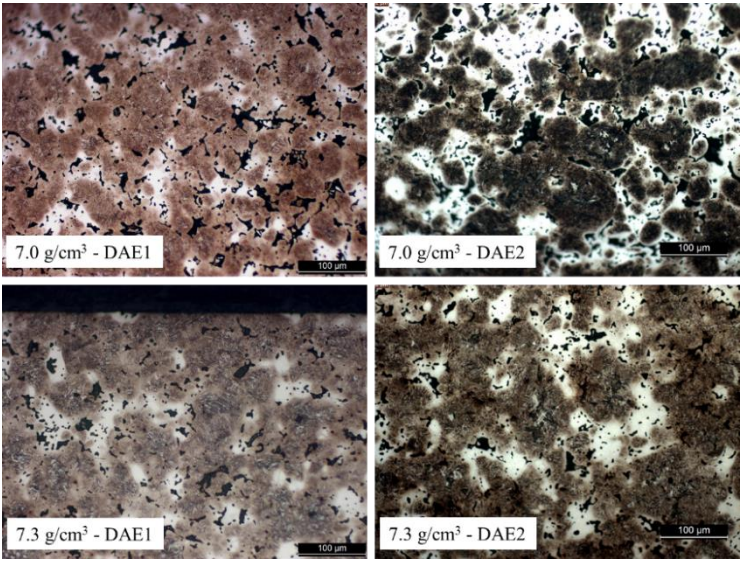

Figure 4.4.2 Etched microstructure of carburized and through hardened DAE materials with different densities

The microstructure of the carburized DAE1 material is the combination of white area, which is Ni-rich austenite, dispersed within the brown martensite matrix. The microstructure of the DAE2 material is almost similar to DAE1, but bainite is present in the dark areas. The amount of white area is higher in through hardened

microstructure than in the case of the carburized materials, due to the lower carbon content in the final microstructure.

The microhardness was measured randomly (mean approach) without selecting each constituent and also locally by selecting the weaker constituent (local approach) on etched microstructure. Figure 4.4.3 shows the microhardness profiles of the weaker constituents and the mean microhardness profiles of carburized and through hardened materials.

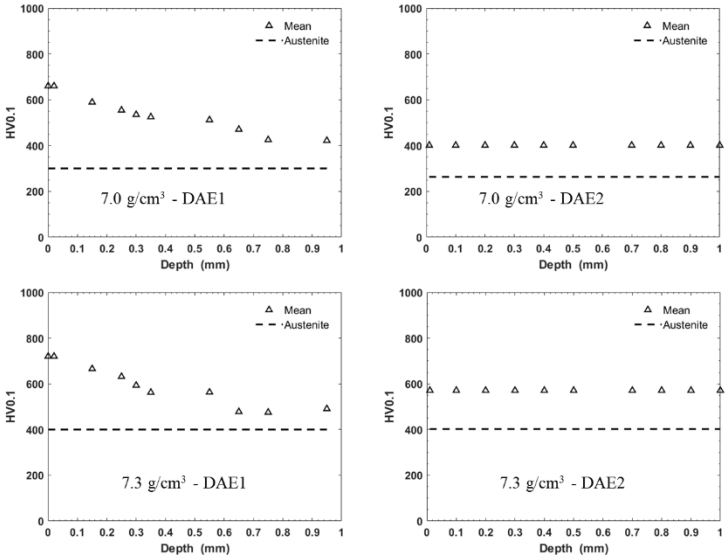

Figure 4.4.3 Microhardness profiles of carburized and through hardened materials with different densities

The mean microhardness profiles of the carburized material show a gradient within 1 mm thick surface layer, while constant profiles are displayed by the through hardened (DAE2) material. Microhardness increases with density, in all the cases. Cases depths of carburized material are 0.5 μm and 0.6 μm for 7.0 g/cm^3 and 7.3 g/cm^3 density, respectively. The difference between case depth and microhardness with density is due to the use of different isothermal holding times, which is longer for

the high density material. The microhardness profile of the weaker constituent (Ni-rich austenite) is constant along the longitudinal cross-sections.

The yield strength profiles of the matrix were calculated from the Ni-rich austenite (softer constituent) microhardness profile and the mean microhardness profile. It is then compared with the Hertzian equivalent stress to predict the nucleation of subsurface cracks. Figure 4.4.4 represents the theoretical prediction of subsurface cracks in carburized and through hardened diffusion bonded materials.

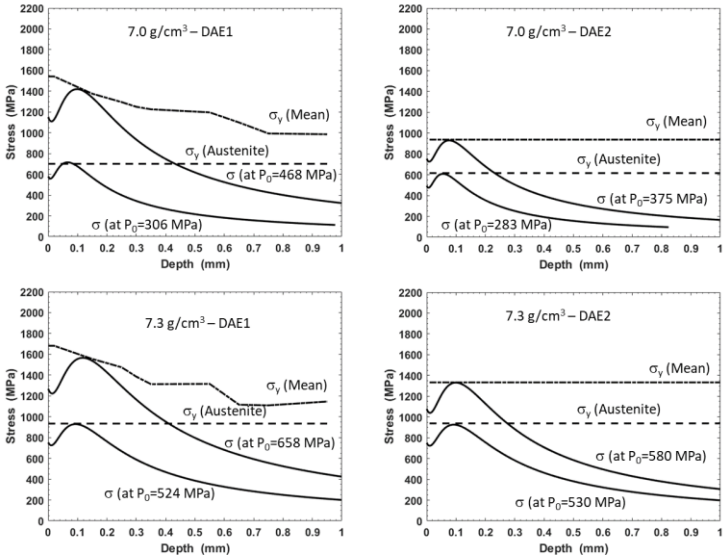

Figure 4.4.4 Theoretical prediction of contact fatigue cracks based on the local and mean approaches of carburized and through hardened materials

Table 4.4.2 summaries the mean pressures, which results in the nucleation of subsurface cracks in the two materials, predicted using different approaches.

Table 4.4.2 Theoretical resistance of carburized and heat treated materials to the nucleation of contact fatigue cracks

Materials	Mean pressure (MPa)	
	Local approach (austenite yield strength)	Mean approach (mean yield strength)
7.0 g/cm^3- DAE1	306	468
7.0 g/cm^3- DAE2	283	375
7.3 g/cm^3- DAE1	524	658
7.3 g/cm^3- DAE2	530	580

The theoretical resistance (the resistance to subsurface crack nucleation) determined using the local approach is always lower than the one determined by the mean approach since the local approach is formulated based on the yield strength of the softer (Ni-rich austenite) microstructural constituent.

When the applied mean pressure exceeds the reported pressures cracks may nucleate due to the local plastic deformation at the Hertzian depth. Table 4.4.3 reports the Hertzian depths determined at the mean pressures corresponding to the theoretical resistance to crack nucleation in the materials.

Table 4.4.3 Hertzian depths at the mean pressures corresponding to the theoretical resistance of austenite and mean microhardness matrix

Material	Hertzian depth (μm)	
	Local approach (austenite yield strength)	Mean approach (mean yield strength)
7.0 g/cm^3- DAE1	66	99
7.0 g/cm^3- DAE2	58	77
7.3 g/cm^3- DAE1	94	117
7.3 g/cm^3- DAE2	92	102

The nucleated crack position is found shallower in the austenite phase and low density materials, and relatively deeper in the high density materials. The Hertzian depth increases with the increases of mean pressures, which was also indicated by figure 4.4.4.

Rolling-sliding contact fatigue test was carried out on the carburized and through hardened materials, at the pressures below and above the theoretical resistance to the formation of contact fatigue cracks (that was determined using the local and mean approaches). Figure 4.4.5 represents the microstructure of worn 7.0 g/cm^3 - DAE1 carburized material tested at different mean pressures.

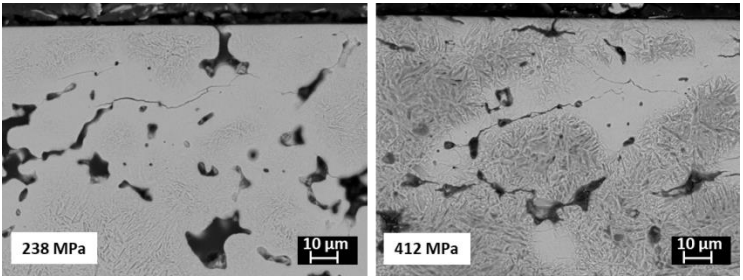

Figure 4.4.5 Microstructure of worn 7.0 g/cm^3 - DAE1 carburized specimen tested at different mean pressures

Subsurface cracks were observed at 238 MPa. This applied mean pressure is below the theoretical resistance of the softer constituent. Also, a test at 412 MPa mean pressures, which is higher than the theoretical resistance of the weaker constituent and lower than the resistance determined from the mean microhardness, resulted in subsurface cracks. These subsurface cracks were nucleated within the Hertzian depth and grew towards the surface along the austenite phase and the pore connectivity.

Figure 4.4.6 represents the microstructure of worn 7.0 g/cm^3 - DAE2 through hardened material tested at different mean pressures.

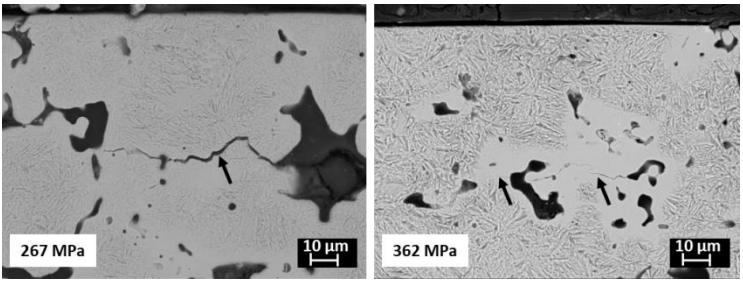

Figure 4.4.6 Microstructure of worn 7.0 g/cm^3 – DAE2 through hardened specimen tested at different mean pressures

Subsurface cracks were observed at 267 MPa mean pressure. This pressure is below the theoretical resistance of the weaker constituent. Also, at a higher mean pressure, 362 MPa (above the resistance of the weaker constituent and below the resistance of the mean microhardness), subsurface cracks were also observed. The occurrence of subsurface cracks are not in agreement with the theoretical prediction based on both the local and the mean approaches. This disagreement indicates the model does not work properly to predict cracks that were detected in the austenite regions.

Similar to 7.0 g/cm^3 carburized and through hardened materials, the experimental results of rolling-sliding contact fatigue tests carried out on 7.3 g/cm^3 materials were compared with the theoretical predictions. Figure 4.4.7 represents the microstructure of worn 7.3 g/cm^3 - DAE1 carburized material tested at different mean pressures.

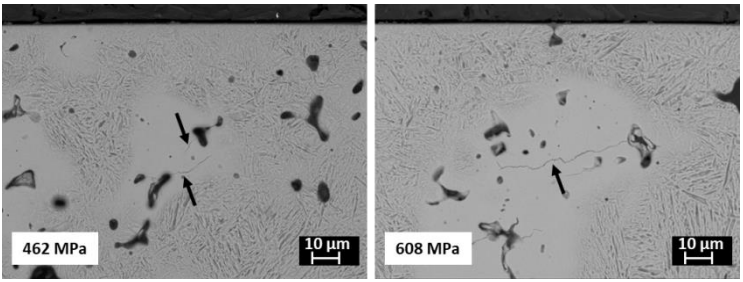

Figure 4.4.7 Microstructure of worn 7.3 g/cm^3 – DAE1 case hardened specimen tested at different mean pressures

Subsurface cracks were observed at 462 MPa, which is below the resistance of the weaker constituent. The experimental evidence is still not in agreement with the theoretical prediction referring to the theoretical resistance of the weaker constituent. Also, a test at 608 MPa that is higher than the resistance of the weaker constituent but lower than the resistance determined from the mean microhardness, cracks were nucleated in the Ni-rich austenite region.

Figure 4.4.8 represents the microstructure of worn 7.3 g/cm^3 - DAE2 through hardened material tested at different mean pressures.

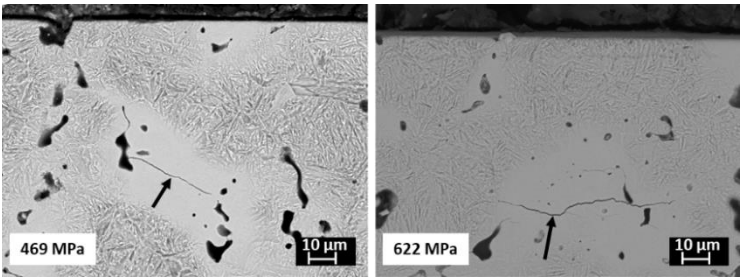

Figure 4.4.8 Microstructure of worn 7.3 g/cm^3 - DAE2 through hardened specimen tested at different mean pressures

Subsurface cracks were observed at 469 MPa. This applied pressure is below the theoretical resistance of the weaker constituent. Also, at a higher pressure, 622 MPa,

subsurface cracks were observed. These cracks nucleate at the edge of the pores and growth through the weaker (Ni-rich austenite) constituent. However, the formation of cracks at a lower pressure are not in agreement with the theoretical prediction based on the weaker constituent.

Similar to the low density materials, the application of local approach is not applicable to predict the nucleation of subsurface cracks accurately in high density materials. Therefore, the theoretical model that was developed based on the comparison of yield strength and equivalent stress need to be verified to investigate carburized and through hardened DAE materials.

4.4.2. Theoretical prediction and experimental results of surface plastic deformation

Surface pore parameters were measured on 250X images collected at SEM. Figure 4.4.9 represents the top surface view of DAE1 and DAE2 materials.

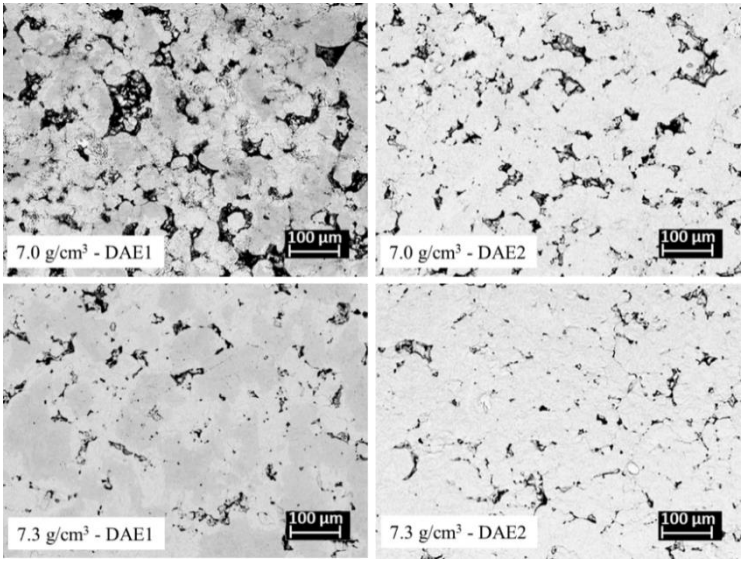

Figure 4.4.9 Top surface view of DAE1 and DAE2 materials with the two densities

Also, Vickers hardness and microhardness were measured on the contact surfaces, and load bearing surface Mr2 was determined from the Abbott Firestone curves. Table 4.4.4 reports the summary of surface characteristics (microhardness, load bearing surface, and elastic modulus) of the two materials.

Table 4.4.4 Surface characteristics of the DAE1 and DAE2 materials

Material	HV10	HV0.1	Mr_2 (%)	E (GPa)
7.0 g/cm^3 - DAE1	268-373	300-700	78	185
7.0 g/cm^3 - DAE2	361-442	263-588	78	185
7.3 g/cm^3 - DAE1	379-453	400-750	82	190
7.3 g/cm^3 - DAE2	435-624	402-749	82	190

Surface hardness, microhardness, load bearing surface and elastic modulus of the carburized material is equivalent to through hardened material, and the parameters increase with density.

The occurrence of surface plastic deformation, at different mean pressures reported in the previous sections, was predicted theoretically with the local and the mean approaches. The theoretical prediction of surface plastic deformation or densification is illustrated using Figure 4.4.10.

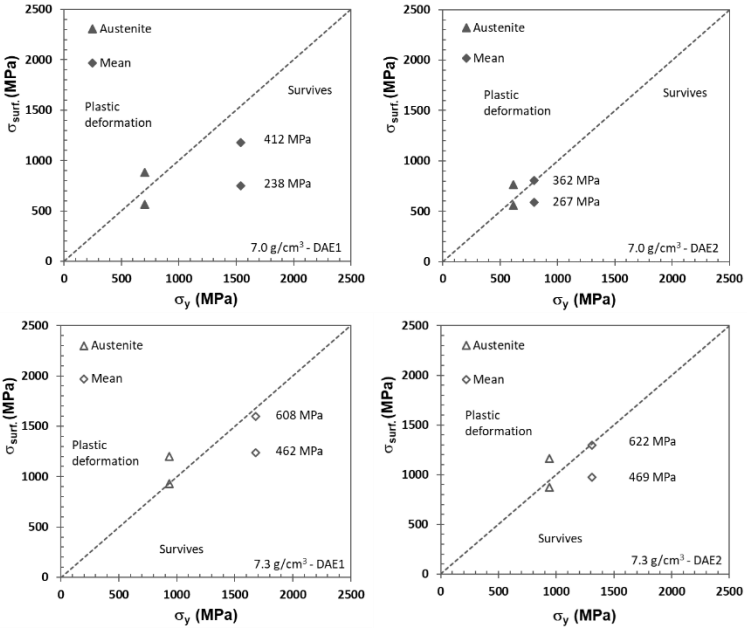

Figure 4.4.10 Theoretical prediction of surface plastic deformation on 7.0 g/cm^3 and 7.3 g/cm^3 carburized and through hardened materials

Except the top right side graph, surface stress is higher on the mean matrix (more martensitic matrix) than on the austenite matrix (weaker constituent) at the same mean pressure. This difference is related with the use of different notch sensitivity values for different constituents: 0.7 for martensitic constituent (mean matrix) and 0.4 for austenite matrix. The dotted bisector line separates the material resistances from surface plastic deformation regimes, and the theoretical results are summarized below:

- 7.0 g/cm^3 - DAE1 material: surface plastic deformation is predicted only at 412 MPa with reference to the theoretical resistance of Ni-rich austenite.
- 7.0 g/cm^3 - DAE2 material: surface plastic deformation is expected at a 362 MPa with reference to the local and mean approaches, and not expected at a lower pressure in all the cases.

- 7.3 g/cm^3 - DAE1 material: surface plastic deformation is predicted only at 608 MPa with reference to the theoretical resistance of Ni-rich austenite.
- 7.3 g/cm^3 - DAE2 material: surface plastic deformation is expected at 622 MPa with reference to the theoretical resistance of Ni-rich austenite.

Carburized and through hardened material shows relatively similar resistance to surface plastic deformation, and the resistance increases with density. The surfaces of the worn specimen observed at SEM to validate the theoretical results. Figure 4.4.11 represents the top surface view of worn 7.0 g/cm^3 - DAE1 materials tested at 238 MPa and 412 MPa mean pressures.

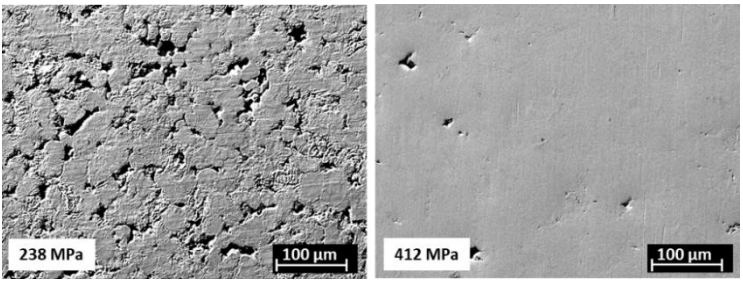

Figure 4.4.11 Top surface view of worn 7.0 g/cm^3 - DAE1 materials tested at different mean pressures

Slight surface plastic deformation was observed at 238 MPa, against the theoretical prediction, since austenite is not expected to undergo plastic deformation at this pressure. Also, at a higher pressure, 412 MPa, extensive surface densification by plastic deformation was observed. Of course, this is in agreement with the theoretical resistance.

Figure 4.4.12 represents the top surface view of worn 7.0 g/cm^3 - DAE2 material tested at 267 MPa and 362 MPa mean pressures.

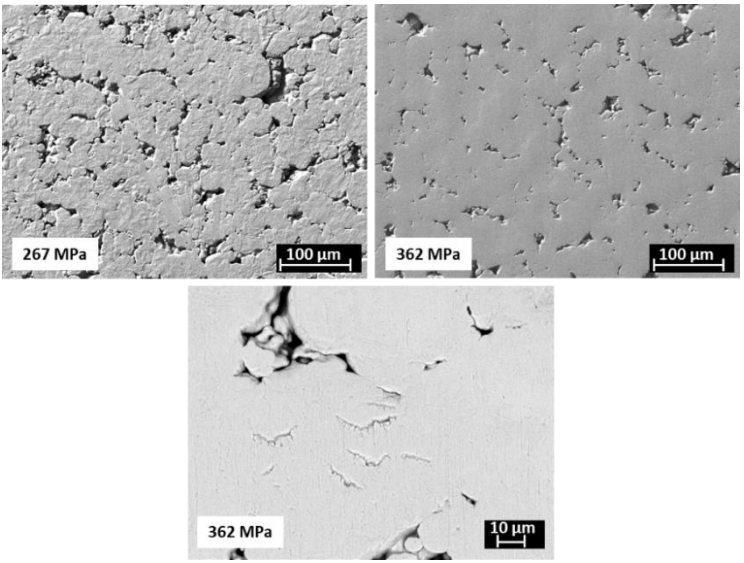

Figure 4.4.12 Top surface view of worn 7.0 g/cm^3 – DAE2 materials tested at different mean pressures

Again, through hardened materials shows slight surface densification at 267 MPa due to plastic deformation. That is not in agreement with the theoretical prediction referring to the resistance of Ni-rich austenite and the mean microhardness. Also, at 362 MPa, the surface is densified extensively and shows a few microcracks.

Similar to low density diffusion bonded materials, the top surface view of worn high density materials were characterized using SEM. Figure 4.4.13 represents the top surface view of worn 7.3 g/cm^3 - DAE1 materials tested at 462 MPa and 608 MPa mean pressures.

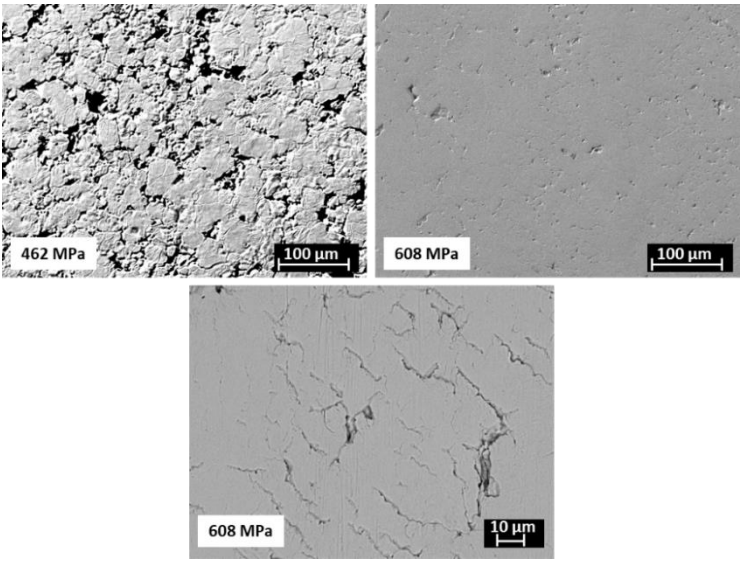

Figure 4.4.13 Top surface view of worn 7.3 g/cm^3 – DAE1 materials tested at different mean pressures

No surface deformation was observed at 462 MPa. However, at higher pressure, 608 MPa, surface cracks and surface densification due to plastic deformation were observed. That is in agreement with the theoretical prediction referring to the resistance of austenite, which predicts no surface plastic deformation at the former pressure and plastic deformation at the latter pressure.

Figure 4.4.14 represents the top surface view of worn 7.3 g/cm^3 - DAE2 materials tested at 469 MPa and 622 MPa mean pressures.

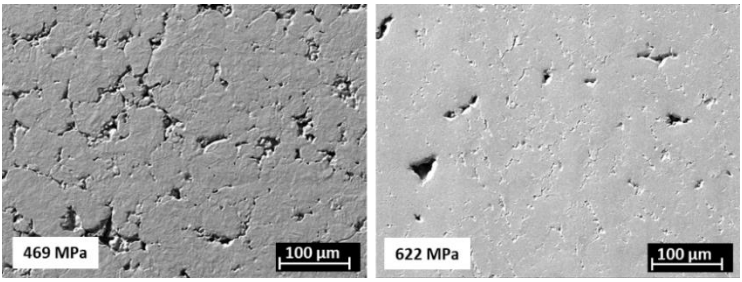

Figure 4.4.14 Top surface view of worn 7.3 g/cm^3 - DAE2 materials tested at different mean pressures

No surface plastic deformation was observed at 469 MPa. However, at higher pressure, 622 MPa, surface densification was observed. That is in agreement with the theoretical prediction referring to the resistance of austenite (weaker constituent).

To summarize the results of surface plastic deformation:

- In the case of low density diffusion bonded materials, the theoretical model with reference to the local and mean approach does not predict the occurrence of surface plastic deformation.
- In the cases of higher density diffusion bonded materials, the occurrence of surface plastic deformation was predicted accurately with reference to the theoretical resistance of Ni-rich austenite (local approach).
- The resistance to surface plastic deformation improves by increasing density.

4.5. Summary

Lubricated rolling-sliding behavior of several PM steels was investigated, with reference to three damage phenomena:

- The nucleation of subsurface contact fatigue cracks due to Hertzian contact stresses;
- The surface plastic deformation due to shear stresses;
- The brittle surface cracks due to surface tensile stress.

Theoretical models were proposed to predict the resistance of the materials to the three damage mechanisms. The first model aims at predicting the contact fatigue cracks, starting from the assumption that crack nucleation is preceded by local plastic deformation when the maximum local stress exceeds the yield strength of the matrix. The second model aims at predicting surface plastic deformation when the surface shear stress exceeds the yield strength of the matrix. The third model aims at predicting brittle surface cracks by comparing the surface tensile stress to the theoretical resistance to brittle fracture (brittle fracture stress).

The theoretical resistance to contact fatigue and surface cracks nucleation of various prealloyed and diffusion bonded PM steels was calculated and verified with lubricated rolling-sliding tests. The materials were obtained with different microstructures through sintering at different temperatures and for a different isothermal holding times, compacting to different green densities, sintering, and sinterhardening, through hardening, carburizing, and shot peening.

The microstructure of the carburized prealloyed materials is homogeneous, while that of the diffusion bonded materials is heterogeneous. Therefore, in the diffusion alloyed steels, the theoretical analysis was carried out with two alternative approaches, based on the mechanical properties of the weaker constituent (local approach) and the mean mechanical properties of the metallic matrix (mean approach).

The results may be summarized as follows.

With reference to the theoretical prediction of the different damage mechanisms investigated, the results show that the theoretical resistance to the nucleation of the subsurface contact fatigue crack is predicted:

- With the mean approach in the prealloyed steels both carburized and shot peened;
- With the mean approach in the Ni-free diffusion bonded steels with a scarcely heterogeneous microstructure, obtained by combining high density and prolonged sintering, both sintered and sinterhardened;
- With the local approach in the Ni-free diffusion bonded steel with heterogeneous microstructure due to standard sintering time, both sintered and sinterhardened;
- With the local approach in the low-Ni diffusion bonded steels, both sintered at standard and high temperature

The nucleation of the contact fatigue cracks cannot be predicted in the high-Ni diffusion bonded steels that are both heat treated and carburized.

The occurrence of brittle surface cracking is predicted with the mean approach in prealloyed materials. Surface brittleness is predicted when theoretical crack size is equivalent to the bigger pore size corresponding to 5% of the whole pore population.

Brittle surface cracks are not investigated or observed in a diffusion bonded materials since the microstructure is heterogeneous and contains softer microstructural constituents.

In diffusion bonded materials the surface plastic deformation is predicted as follows:

- With the mean approach for high density Ni-free diffusion bonded material in both sintered and sinterhardening conditions;
- With the local approach for low density Ni-free diffusion bonded material in both sintered and sinterhardening conditions;
- With the local approach for low-Ni diffusion bonded materials at both low and high sintering temperatures.
- With the local approach in high-Ni diffusion bonded steels at high density, both carburized and through hardened.

Neither the mean approach nor the local approach can predict plastic deformation in low density high-Ni diffusion bonded steels.

The reason for this result may be the presence of large porosity in the Ni-rich areas. By looking at the microstructure, it may observe that the Ni-rich regions contain a significantly larger fraction of pores, sometimes quite large, than the mean fraction of porocity in the material. Therefore, using the mean porosity to determine the fraction of the load bearing section leads to an underestimation of the maximum local stress. As an example, figure 4.5.1 shows the theoretical resistance to subsurface crack nucleation in the 7.0 carburized DAE steel as a function of porosity; by simply increasing porosity from 0.11 (the man one) up to 0.15 the theoretical resistance decreases by 28%. Extensive work is needed to investigate this issue.

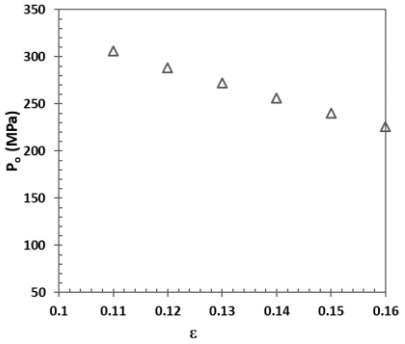

Figure 4.5.1 The effect of porosity of the theoretical resistance to contact fatigue of carburized DAE material

Finally, the investigated materials may rank with reference to the theoretical resistance to the damage mechanisms investigated, as shown in Table 4.5.1. The data for DAE steels are inserted in the last four rows since they were not verified experimentally.

Table 4.5.1 Material ranking based on the theoretical resistance to the three damage mechanisms

Material	Treatment	Mean pressure (MPa)			Verified
		Contact fatigue cracks	Surface plastic deformation	Brittle surface cracks	
AMo1	shot peened	**881**	n.a.	1352	yes
A85Mo	shot peened	**868**	n.a.	1340	yes
A85Mo	Carburized	845	n.a.	**795**	yes
AMo1	Carburized	881	n.a.	**744**	yes
7.3 g/cm^3–DDH2	Sinterhardened	**641**	669	n.a.	yes
7.3 g/cm^3–AS1250	Sinterhardened	**504**	519	n.a.	yes
7.2 g/cm^3– Ecosint1250	Sinterhardened	**481**	484	n.a.	yes
7.0 g/cm^3–DDH2	Sinterhardened	**425**	508	n.a.	yes
7.3 g/cm^3– AS1150	Sinterhardened	**342**	451	n.a.	yes
7.3 g/cm^3–DDH2	Sintered	**310**	310	n.a.	yes
7.2 g/cm^3– Ecosint1150	Sinterhardened	**243**	279	n.a.	yes
7.0 g/cm^3–DDH2	Sintered	**180**	221	n.a.	yes
7.0 g/cm^3–DAE1	Carburized	306	377	n.a.	not
7.0 g/cm^3–DAE2	Heat treated	283	324	n.a.	not
7.3 g/cm^3–DAE1	Carburized	524	512	n.a.	not subsurface
7.3 g/cm^3 –DAE2	Heat treated	530	465	n.a.	not subsurface

Shot peened prealloyed materials are ranked first, and their resistance determined by the resistance to the contact fatigue crack nucleation. Carburized prealloyed materials are also ranked second next to shot peening, and the resistance to brittle surface cracks determines their resistance. Ni-free diffusion bonded material shows better resistance at high density and if sintered for a longer time to the homogenization of the microstructure through diffusion; the resistance of these materials is determined by the resistance to contact fatigue crack formation.

Chapter V

5. Conclusions

Subsurface crack (contact fatigue crack) nucleation, brittle surface cracking, and surface plastic deformation are possible damage mechanisms in materials that are subject to lubricated rolling-sliding contact. In this thesis, these mechanisms have been investigated in many Powder Metallurgy steels.

The investigated materials are prealloyed (homogeneous microstructure) and diffusion bonded (heterogeneous microstructure). They were produced with different microstructures (porosity and constituents of the metallic matrix) and mechanical properties by varying the chemical composition, green density, sintering temperature and time, and by applying different strengthening processes, such as sinterhardening, through hardening, and carburizing. Shot peening was also investigated.

The occurrence of the damage mechanisms mentioned above was predicted based on the analysis of the local stress conditions (in the Hertzian depth and at the surface) and their comparison to the resistance of the matrix to plastic deformation and brittle fracture. Rolling-sliding tests were then carried out to verify the theoretical models. Due to the microstructural heterogeneity, the theoretical analysis was carried out with two approaches: the mean approach which refers to the mean mechanical properties of the matrix, and the local approach which refers to the mechanical properties of the weaker constituent.

The first conclusion, on prealloyed (Fe-0.85Mo and Fe-1.5Mo) steels, may be summarized as:

- Subsurface and surface cracks can be predicted with the mean approach since the case microstructure is homogeneous.

- Shot peening improves the resistance to brittle surface cracks by more than 30%. However, shot peening is not effective in improving the resistance to contact fatigue cracks.
- The two materials have nearly the same resistance to contact fatigue crack nucleation and brittle surface cracking; therefore, the addition of Mo higher than 0.85% may not be effective in improving the contact fatigue and surface damage behavior of carburized steels.
- The theoretical resistance agrees with the experimental evidence if the equivalent stress is used to calculate the maximum Hertzian stress.

The second conclusion, on the diffusion bonded (Ni-free, low-Ni addition and high-Ni addition) materials, may be summarized as follows:

- The mean and the local approaches succeed in predicting subsurface crack nucleation and surface plastic deformation in high density and low density Ni-free materials, respectively; the difference may be associated with the isothermal holding time, which takes longer for high density and subsequently provides relatively a homogenized microstructure.
- The local approach is applied to predict subsurface crack nucleation and surface plastic deformation in low-Ni materials sinterhardened at low and high temperatures since they maintain a rather non-homogeneous microstructure.
- Neither the local nor the mean approach predicts subsurface cracks in a high-Ni material, that has been both case hardened and through hardened, due to the presence of a cluster of pores in Ni-rich austenite, which makes the determination of the fraction of the load bearing section very difficult.
- Increase in density and sinterhardening improves the resistance to subsurface crack nucleation and surface plastic deformation of Ni-free material.

- High sintering temperature improves the resistance to subsurface crack nucleation and surface plastic deformation of low-Ni addition materials.
- Brittle surface crack nucleation was not studied and not even observed in all diffusion bonded materials; this may be associated with microstructural heterogeneity and the presence of a soft constituent in the microstructures.

Finally, the materials investigated were ranked based on their resistance to the damage mechanisms. Shot peened prealloyed materials are the best performing steels; they can work at a higher pressures than the other investigated steels without brittle surface cracking and contact fatigue crack nucleation. Carburized prealloyed materials are the second choice, their working pressure determined by the resistance to brittle surface crack nucleation. The Ni-free and low-Ni addition diffusion bonded materials display lower resistance than prealloyed materials, the former being slightly more resistant.

Lastly, since the theoretical models are not able to predict the subsurface cracks and surface plastic deformation in high-Ni addition diffusion bonded material, the definition of reliable models is still an open issue. Formulating an accurate model may require further work mostly focused on the determination of the fraction of the load bearing section as this parameter is affected by the pore clustering in the Ni-rich areas.

References

[1] R.M. German, In Powder Metallurgy Science: Material Powder Industries Seperation, MPIF Princet. 28 (**1994**).

[2] T.E. Tallian, Failure Atlas for Hertz Contact Machine Elements, ASME Press, **1999**.

[3] ASM Handbook, Volume 19: Fatigue and Fracture - ASM International, (n.d.). http://www.asminternational.org/handbooks/-/journal_content/56/10192/25656855/PUBLICATION (accessed April 6, **2017**).

[4] E.E. Magel, Rolling contact fatigue: a comprehensive review, U.S. Department of Transportation. Federal Railroad Administration, **2011**. doi:10.4224/23000318.

[5] F. Sadeghi, B. Jalalahmadi, T.S. Slack, N. Raje, N.K. Arakere, A Review of Rolling Contact Fatigue, J. Tribol. 131 (**2009**) 041403-041403–15. doi:10.1115/1.3209132.

[6] W. Solano-Alvarez, H.K.D.H. Bhadeshia, White-Etching Matter in Bearing Steel. Part II: Distinguishing Cause and Effect in Bearing Steel Failure, Metall. Mater. Trans. A. 45 (**2014**) 4916–4931. doi:10.1007/s11661-014-2431-x.

[7] A. Clarke, H. Evans, R. Snidle, Understanding micropitting in gears, Proc. Inst. Mech. Eng. Part C J. Mech. Eng. Sci. 230 (**2016**) 1276–1289. doi:10.1177/0954406215606934.

[8] N. Saka, A.M. Eleiche, N.P. Suh, Wear of metals at high sliding speeds, Wear. 44 (**1977**) 109–125. doi:10.1016/0043-1648(77)90089-8.

[9] T.E. Tallian, Simplified Contact Fatigue Life Prediction Model—Part I: Review of Published Models, J. Tribol. 114 (**1992**) 207. doi:10.1115/1.2920875.

[10] A.V. Olver, The Mechanism of Rolling Contact Fatigue: An Update, Proc. Inst. Mech. Eng. Part J J. Eng. Tribol. 219 (**2005**) 313–330. doi:10.1243/135065005X9808.

[11] Contact Fatigue - 06197G_Sample_BuyNow.pdf, (n.d.). http://www.asminternational.org/documents/10192/1849770/06197G_Sample_BuyNow.pdf/2f15ca46-5605-4688-997a-c6f2d138829a (accessed September 18, **2017**).

[12] C.M. Sonsino, K. Lipp, Rolling contact fatigue properties of selected PM-materials for gear-box applications, SAE Technical Paper, 1999. http://papers.sae.org/1999-01-0333/ (accessed June 13, **2017**).

[13] C.M. Sonsino, Fatigue design for powder metallurgy, Met. Powder Rep. 45 (**1990**) 754–764. doi:10.1016/0026-0657(90)90460-X.

[14] C.M. Sonsino, Fatigue design principles for sintered steel components, J. Strain Anal. Eng. Des. 41 (**2006**) 497–555. doi:10.1243/03093247JSA174.

[15] J. Holmes, R.A. Queeney, Fatigue Crack Initiation in a Porous Steel, Powder Metall. (**2013**). doi:10.1179/pom.1985.28.4.231.

[16] G. Hoffmann, W. Jandeska, Effects on Rolling Contact Fatigue Performance, Gear Technol. (**2007**) 42–52.

[17] K. Lipp, G. Hoffmann, Design for roling contact fatigue, Int. J. Powder Metall. 39 (**2003**) 33–46.

[18] R. HAYNES, Fatigue Behaviour of Sintered Metals and Alloys, Powder Metall. 13 (**1970**) 465–510. doi:10.1179/pom.1970.13.26.020.

[19] N. Chawla, J.J. Williams, Fatigue and fracture of powder metallurgy steels, in: Adv. Powder Metall., Elsevier, **2013**: pp. 455–490. doi:10.1533/9780857098900.3.455.

[20] N. Chawla, X. Deng, Microstructure and mechanical behavior of porous sintered steels, Mater. Sci. Eng. A. 390 (**2005**) 98–112. doi:10.1016/j.msea.2004.08.046.

[21] A. Sinha, Z. Farhat, Effect of Surface Porosity on Tribological Properties of Sintered Pure Al and Al 6061, Mater. Sci. Appl. 06 (**2015**) 549. doi:10.4236/msa.2015.66059.

[22] A. Simchi, H. Danninger, Effects of porosity on delamination wear behaviour of sintered plain iron, Powder Metall. 47 (**2004**) 73–80. doi:10.1179/003258904225015545.

[23] F. Hanejko, A. Rawlings, P. King, G. Poszmik, Surface Densification Coupled with Higher Density Processes Targeting High-Performance Gearing, Mater. Sci. Forum. 534–536 (**2007**) 317–320. doi:10.4028/www.scientific.net/MSF.534-536.317.

[24] F. Hanejko, A. Rawlings, K.S.V. Narasimhan, Surface densified P/M steel–Comparison with wrought steel grades, Euro PM2005 Prague. (**2005**) 509–511.

[25] B. Kubicki, Stress Concentration at Pores in Sintered Materials, Powder Metall. 38 (1995) 295–298. doi:10.1179/pom.1995.38.4.295.

[26] G. Straffelini, A. Molinari, Effect of hardness on rolling–sliding damage mechanisms in PM alloys, Powder Metall. 44 (**2001**) 344–350. doi:10.1179/pom.2001.44.4.344.

[27] A. Šalak, Ferrous Powder Metallurgy, Cambridge International Science Pub., **1995**.

[28] A. Molinari, C. Menapace, E. Santuliana, G. Straffelini, A simplified model for the impact resistance of porous sintered steels, Powder Metall. Prog. 11 (**2011**) 12–20.

[29] P. Beiss, M. Dalgic, Structure property relationships in porous sintered steels, Mater. Chem. Phys. 67 (**2001**) 37–42. doi:10.1016/S0254-0584(00)00417-X.

[30] R.A. Grange, C.R. Hribal, L.F. Porter, Hardness of tempered martensite in carbon and low-alloy steels, Metall. Trans. A. 8 (**1977**) 1775–1785. doi:10.1007/BF02646882.

[31] O. Bergman, B. Lindqvist, S. Bengtsson, Influence of Sintering Parameters on the Mechanical Performance of PM Steels Pre-Alloyed with Chromium, Mater. Sci. Forum. 534–536 (**2007**) 545–548. doi:10.4028/www.scientific.net/MSF.534-536.545.

[32] Y. Shen, S.M. Moghadam, F. Sadeghi, K. Paulson, R.W. Trice, Effect of retained austenite – Compressive residual stresses on rolling contact fatigue life of carburized AISI 8620 steel, Int. J. Fatigue. 75 (**2015**) 135–144. doi:10.1016/j.ijfatigue.2015.02.017.

[33] A. Molinari, I. Metinöz, I. Cristofolini, A CONSERVATIVE APPROACH TO PREDICT THE CONTACT FATIGUE BEHAVIOR OF SINTERED STEELS, Powder Metall. Prog. 14 (**2014**) 32.

[34] N. Kurgan, Effect of porosity and density on the mechanical and microstructural properties of sintered 316L stainless steel implant materials, Mater. Des. 55 (2014) 235–241. doi:10.1016/j.matdes.2013.09.058.

[35] I. Sauermann, P. Beiss, Rolling Contact Fatigue of a Case Hardened High Density PM Steel, Adv Powder Met. Part. Mat-2007. 10 (**2007**) 35–46.

[36] G.F. Bocchini, B. Rivolta, G. Silva, E. Poggio, M.R. Pinasco, M.G. Ienco, Microstructural and mechanical characterisation of some sinter hardening alloys and comparisons with heat treated PM steels, Powder Metall. 47 (**2004**) 343–351. doi:10.1179/003258904X14464.

[37] P.S. Prevéy, The effect of cold work on the thermal stability of residual compression in surface enhanced IN718, DTIC Document, **2000**. http://oai.dtic.mil/oai/oai?verb=getRecord&metadataPrefix=html&identifier=ADA452401 (accessed May 31, 2017).

[38] A. Molinari, E. Santuliana, I. Cristofolini, A. Rao, S. Libardi, P. Marconi, Surface modifications induced by shot peening and their effect on the plane bending fatigue strength of a Cr–Mo steel produced by powder metallurgy, Mater. Sci. Eng. A. 528 (**2011**) 2904–2911. doi:10.1016/j.msea.2010.12.072.

[39] E. Nordin, B. Alfredsson, Experimental Investigation of Shot Peening on Case Hardened SS2506 Gear Steel, Exp. Tech. (**2017**) 1–19. doi:10.1007/s40799-017-0183-4.

[40] H. Xiao, Q. Chen, E. Shao, D. Wu, Z. Chen, Z. Wang, The effect of shot peening on rolling contact fatigue behaviour and its crack initiation and propagation in carburized steel, Wear. 151 (**1991**) 77–86. doi:10.1016/0043-1648(91)90347-W.

[41] Y. Kobayashi, T. Tsuji, R. Ishikura, K. Inoue, Influences of Mechanical Properties and Retained Austenite Content on Shot-peening Characteristics, Trans. Jpn. Soc. Spring Eng. 2012 (**2012**) 9–15. doi:10.5346/trbane.2012.9.

[42] S. Wang, Y. Li, M. Yao, R. Wang, Compressive residual stress introduced by shot peening, J. Mater. Process. Technol. 73 (**1998**) 64–73. doi:10.1016/S0924-0136(97)00213-6.

[43] J.J. Williams, X. Deng, N. Chawla, Effect of residual surface stress on the fatigue behavior of a low-alloy powder metallurgy steel, Int. J. Fatigue. 29 (**2007**) 1978–1984. doi:10.1016/j.ijfatigue.2007.01.008.

[44] I. Metinöz, I. Cristofolini, W. Pahl, A. DeNicolo, P. Marconi, A. Molinari, Theoretical and experimental study of the contact fatigue behavior of a Mo–Cu steel produced by powder metallurgy, Mater. Sci. Eng. A. 614 (**2014**) 81–87. doi:10.1016/j.msea.2014.07.009.

[45] L. Ruiz, M.J. Readey, Effect of Heat Treatment on Grain Size, Phase Assemblage, and Mechanical Properties of 3 mol% Y-TZP, J. Am. Ceram. Soc. 79 (**1996**) 2331–2340. doi:10.1111/j.1151-2916.1996.tb08980.x.

[46] K.L. Johnson, Contact Mechanics, Cambridge University Press, Cambridge, 1985. doi:10.1017/CBO9781139171731.

[47] G. Straffelini, Friction and Wear, Springer International Publishing, Cham, **2015**. doi:10.1007/978-3-319-05894-8.

[48] S. Glodež, H. Winter, H.P. Stüwe, A fracture mechanics model for the wear of gear flanks by pitting, Wear. 208 (**1997**) 177–183. doi:10.1016/S0043-1648(97)00008-2.

[49] K.L. Johnson, K.L. Johnson, Contact mechanics, Cambridge university press, **1987**. https://books.google.it/books?hl=it&lr=&id=Do6WQlUwbpkC&oi=fnd&pg=PA1&dq=johnson+contact+mechanics&ots=gplgiyib0_&sig=HwdQhKArOwIf-HAXsqmgqgk1acM.

[50] C. Santus, M. Beghini, I. Bartilotta, M. Facchini, Surface and subsurface rolling contact fatigue characteristic depths and proposal of stress indexes, Int. J. Fatigue. 45 (**2012**) 71–81. doi:10.1016/j.ijfatigue.2012.06.012.

[51] A. Bhattacharyya, G. Subhash, N. Arakere, Evolution of subsurface plastic zone due to rolling contact fatigue of M-50 NiL case hardened bearing steel, Int. J. Fatigue. 59 (**2014**) 102–113. doi:10.1016/j.ijfatigue.2013.09.010.

[52] M. Widmark, A. Melander, Effect of material, heat treatment, grinding and shot peening on contact fatigue life of carburised steels, Int. J. Fatigue. 21 (**1999**) 309–327. doi:10.1016/S0142-1123(98)00077-2.

[53] T. Slack, F. Sadeghi, Explicit finite element modeling of subsurface initiated spalling in rolling contacts, Tribol. Int. 43 (**2010**) 1693–1702. doi:10.1016/j.triboint.2010.03.019.

[54] G.G. Adams, M. Nosonovsky, Contact modeling — forces, Tribol. Int. 33 (**2000**) 431–442. doi:10.1016/S0301-679X(00)00063-3.

[55] B. Bhushan, Contact mechanics of rough surfaces in tribology: multiple asperity contact, Tribol. Lett. 4 (**1998**) 1–35. doi:10.1023/A:1019186601445.

[56] B. Bhushan, Contact Mechanics of Rough Surfaces in Tribology: Single Asperity Contact, Appl. Mech. Rev. 49 (**1996**) 275–298. doi:10.1115/1.3101928.

[57] D. Hannes, B. Alfredsson, Modelling of Surface Initiated Rolling Contact Fatigue Damage, Procedia Eng. 66 (**2013**) 766–774. doi:10.1016/j.proeng.2013.12.130.

[58] B. Zafošnik, Z. Ren, J. Flašker, G. Mishuris, Modelling of Surface Crack Growth under Lubricated Rolling–Sliding Contact Loading, Int. J. Fract. 134 (**2005**) 127–149. doi:10.1007/s10704-005-8546-8.

[59] T.E. Tallian, J.I. McCool, An engineering model of spalling fatigue failure in rolling contact, Wear. 17 (**1971**) 447–461. doi:10.1016/0043-1648(71)90050-0.

[60] E. Bormetti, G. Donzella, A. Mazzù, Surface and Subsurface Cracks in Rolling Contact Fatigue of Hardened Components, Tribol. Trans. 45 (**2002**) 274–283. doi:10.1080/10402000208982550.

[61] G. Straffelini, A. Molinari, T. Marcupuscas, Identification of rolling-sliding damage mechanisms in porous alloys, Metall. Mater. Trans. A. 31 (**2000**) 3091–3099. doi:10.1007/s11661-000-0088-0.

[62] Y. Ding, N.F. Rieger, Spalling formation mechanism for gears, Wear. 254 (**2003**) 1307–1317. doi:10.1016/S0043-1648(03)00126-1.

[63] T. Makino, Y. Neishi, D. Shiozawa, S. Kikuchi, S. Okada, K. Kajiwara, Y. Nakai, Effect of defect shape on rolling contact fatigue crack initiation and propagation in high strength steel, Int. J. Fatigue. 92 (**2016**) 507–516. doi:10.1016/j.ijfatigue.2016.02.015.

[64] T. Makino, Y. Neishi, D. Shiozawa, Y. Fukuda, K. Kajiwara, Y. Nakai, Evaluation of rolling contact fatigue crack path in high strength steel with artificial defects, Int. J. Fatigue. 68 (**2014**) 168–177. doi:10.1016/j.ijfatigue.2014.05.006.

[65] Q. Chen, E. Shao, D. Zhao, J. Guo, Z. Fan, Measurement of the critical size of inclusions initiating contact fatigue cracks and its application in bearing steel, Wear. 147 (**1991**) 285–294. doi:10.1016/0043-1648(91)90186-X.

[66] N. Govindarajan, R. Gnanamoorthy, Study of damage mechanisms and failure analysis of sintered and hardened steels under rolling–sliding contact conditions, Mater. Sci. Eng. A. 445–446 (**2007**) 259–268. doi:10.1016/j.msea.2006.09.039.

[67] R. Ahmed, Rolling contact fatigue, ASM Handb. 11 (**2002**) 941–956.

[68] J.W. Ringsberg, Life prediction of rolling contact fatigue crack initiation, Int. J. Fatigue. 23 (**2001**) 575–586. doi:10.1016/S0142-1123(01)00024-X.

[69] J.O. Smith, C.K. Liu, Stresses due to tangential and normal loads on an elastic solid with application to some contact stress problems, J. Appl. Mech.-Trans. ASME. 20 (**1953**) 157–166.

[70] N. Govindarajan, R. Gnanamoorthy, Rolling/sliding contact fatigue life prediction of sintered and hardened steels, Wear. 262 (**2007**) 70–78. doi:10.1016/j.wear.2006.03.053.

[71] D. Pohl, On the fatigue strength of sintered iron, Powder Metall. Int. 1 (**1969**) 26–28.

[72] T. Bell, Y. Sun, Load Bearing Capacity of Plasma Nitrided Steelunder Rolling–Sliding Contact, Surf. Eng. 6 (**1990**) 133–139. doi:10.1179/sur.1990.6.2.133.

[73] S.J. Sharp, M.F. Ashby, N.A. Fleck, Material response under static and sliding indentation loads, Acta Metall. Mater. 41 (**1993**) 685–692. doi:10.1016/0956-7151(93)90002-A.

[74] I. Cristofolini, A. Molinari, G. Straffelini, P.V. Muterlle, A systematic approach to design against wear for Powder Metallurgy (PM) steel parts: The case of dry rolling–sliding wear, Mater. Des. 32 (**2011**) 2191–2198. doi:10.1016/j.matdes.2010.11.033.

[75] G. Straffelini, C. Menapace, A. Molinari, Interpretation of effect of matrix hardening on tensile and impact strength of sintered steels, Powder Metall. 45 (**2002**) 167–172. doi:10.1179/003258902225002587.

[76] D. Nélias, M.L. Dumont, F. Champiot, A. Vincent, D. Girodin, R. Fougéres, L. Flamand, Role of Inclusions, Surface Roughness and Operating Conditions on Rolling Contact Fatigue, J. Tribol. 121 (**1999**) 240–251. doi:10.1115/1.2833927.

[77] G. Straffelini, V. Fontanari, A. Hafez, M. Benedetti, Tensile and fatigue behaviour of sinter hardened Fe–1·5Mo–2Cu–0·6C steels, Powder Metall. 52 (**2009**) 298–303. doi:10.1179/003258909X12502679013774.

[78] Steel Heat Treatment Handbook : George E. Totten : 9780824727413, (n.d.). https://www.bookdepository.com/Steel-Heat-Treatment-Handbook-George-E-Totten/9780824727413 (accessed October 24, **2017**).

[79] J.I. Goldstein, A.E. Moren, Diffusion modeling of the carburization process, Met. Trans A. 9 (**1978**) 1515–1525.

[80] F. Castro, S. Sainz, B. Lindsley, W. Brian James, The Effect Of Sintering Conditions And Composition On The Mechanical Property Response Of Cr Containing PM Steels, 29 (**2011**).

[81] W. Jandeska, R. Slattery, F. Hanejko, A. Rawlings, P. King, Rolling-Contact-Fatigue Performance Contrasting Surface-Densified, Powder Forged, and Wrought Materials, Adv. POWDER Metall. Part. Mater. 3 (**2005**) 12.

[82] M. Boniardi, F. D'Errico, C. Tagliabue, Influence of carburizing and nitriding on failure of gears – A case study, Eng. Fail. Anal. 13 (**2006**) 312–339. doi:10.1016/j.engfailanal.2005.02.021.

[83] F. D'Errico, Micropitting Damage Mechanism on Hardened and Tempered, Nitrided, and Carburizing Steels, Mater. Manuf. Process. 26 (**2011**) 7–13. doi:10.1080/10426910903388424.

Scientific Production

International Journals

1. S. Tesfaye Mekonone, A. Molinari, W. Pahl, 'Damage Phenomena in Lubricated Rolling-Sliding Wear of a Gas Carburized 0.85%Mo Low-Alloyed Sintered Steel: Theoretical Analysis and Experimental Verification', Powder Metall., 2017, **60(5)**, 321–329.
2. S. Tesfaye Mekonone, A. Molinari, W. Pahl, 'Influence of the microstructure on the subsurface and surface damage during lubricated rolling-sliding wear of sintered and sinterhardened 1.5%Mo-2%Cu-0.6%C steel: theoretical analysis and experimental investigation', Powder Metall., 2018,https://doi.org/10.1080/00325899.2018.1446706.
3. A. Molinari, S. Tesfaye Mekonone, I. Cristofolini, W. Pahl, 'Surface hardening vs. surface embrittlement in carburizing of porous steels', Powd. Metall. Prog., in press

Proceedings

1. S. Tesfaye Mekonone, A. Molinari, P. Wolfgnang, Theoretical and experimental investigation of rolling/sliding surface damage of sinterhardened low alloyed Mo-Cu steel, in Congress Proceedings EuroPM 2017, Milan- Italy: EPMA, 2017. - ISBN: 978-1-899072-48-4. -D: Euro PM 2017, Milan 1-5.
2. A. Molinari, S. Tesfaye Mekonone, W. Pahl, A. Denicolo, P. Marconi, Effect of shot peening on the formation of surface cracks during lubricated rolling-sliding wear of carburized low Mo alloyed sintered steel, Adv. Powd. Metal. & Part. Mater., 2017, **6,** 589-597.
3. S. Tesfaye Mekonone, A. Molinari, P. Wolfgnang, A. De Nicolo, microstructure and residual stress of shot peened 0.85%Mo carburized PM steels, in Proceedings WorldPM 2016, Hamburg - Germany: EPMA, 2016. - ISBN: 978-1-899072-48-4. -D: WorldPM 2016, Hamburg, 9-13 October 2016.

Acknowledgments

First and foremost, I would like to thank my advisors Prof. Alberto Molinari and Prof. Ilaria Cristofolini for their excellent guidance and support during my Ph.D. study. In particular, I want to express my deepest gratitude to Prof. Alberto Molinari, for his understanding, caring with a fatherly approach and showing me an extreme patient; without him, this work could not be completeted.

I gratefully acknowledge GKN Sinter Metals R&D team for preparation of all specimens and arranging helpful meetings. In particular, I would like to thank Dr. Wolfgang Pahl for his valuable comments.

I would like to thank the group of Mechanical, Metallurgy and Microstructure Laboratory: Cinzia, Giulia, Lorena, Simone, Nicolò, Marco, Faraz, Silvia, Sazan, and Elisa. They were always available to me when I need help and support. I want to thank Dr. Ibrahim Metinöz for his training on Tribometer. I want to thank Prof. Vigilio Fontanari, Prof. Massimo Pellizzari and Mr. Emillio for their assistance and providing quick maintenances when Amsler fails. Also, I would like to thank Paolo Gussago (master's student), Daniel Frizzo and Pierguido Danzo (bachelor students) for their assistance on the experimental works.

I would like to thank Dr. Lorena Maines and Dr. Gloria Ischia for their availability during the electron microscope image preparations.

I want to thank all my friends for their accompaniment, in particular, Getch, Elias, John, and Dave they were always good for me.

I would like to thank my family for their unconditional support. To call a few: my father Tesfaye and stepmother Etalemahu; little brothers Abraham and Solomon; little sister Kidist; cousin Dr. Mekonnen, Tigza and Yalewayiker they were always available to help me when I was in trouble. Lastly, I want to thank my cousin Emebet Alemu for her wise advice; without her words, I would quit my Ph.D. study at the beginning of the program.